

1

UNIVERSITY OF BRISTOL

2

DOCTORAL THESIS

3

4

Investigating, implementing, and creating methods for analysing large neuronal ensembles

5

6

Author:

Thomas J. DELANEY

Supervisors:

Dr. Cian O'DONNELL

Dr. Michael C. ASHBY

7

A thesis submitted in fulfillment of the requirements

for the degree of Doctor of Philosophy

8

in the

9

Biological Intelligence & Machine Learning Unit

10

Department of Computer Science

11

July 11, 2020

¹⁵ Declaration of Authorship

¹⁶ I, Thomas J. DELANEY, declare that this thesis titled, "Investigating, implementing, and
¹⁷ creating methods for analysing large neuronal ensembles" and the work presented in it are
¹⁸ my own. I confirm that:

- ¹⁹ • This work was done wholly or mainly while in candidature for a research degree at this
²⁰ University.
- ²¹ • Where any part of this thesis has previously been submitted for a degree or any other
²² qualification at this University or any other institution, this has been clearly stated.
- ²³ • Where I have consulted the published work of others, this is always clearly attributed.
- ²⁴ • Where I have quoted from the work of others, the source is always given. With the
²⁵ exception of such quotations, this thesis is entirely my own work.
- ²⁶ • I have acknowledged all main sources of help.
- ²⁷ • Where the thesis is based on work done by myself jointly with others, I have made
²⁸ clear exactly what was done by others and what I have contributed myself.

²⁹

³⁰ Signed:

³¹ _____

³² Date:

³³ _____

34

UNIVERSITY OF BRISTOL

35

Abstract

36

Engineering

37

Department of Computer Science

38

Doctor of Philosophy

39

Investigating, implementing, and creating methods for analysing large neuronal ensembles

40

by Thomas J. DELANEY

42

Ever since the use of multi-electrode recording in neuroscience began, the number neurons being recorded in parallel has been increasing. Methods developed more recently using calcium or voltage imaging have also contributed to the growth in neuronal datasets. As datasets grow, the need for new analysis methods that scale also grows. In our research we attempted to address some of the problems associated with reading from large neuronal ensembles using fluorescent calcium indicators by creating a new biophysical model for the fluorescence trace induced by spike trains. This model should be helpful for ... We applied a novel method from network science for detecting structure and communities in the correlated behaviour of a large dataset. We aimed to find order and structure in this dataset at different timescales and investigate the differences We developed a new statistical model for the number of neurons spiking in a neuronal ensemble based on the Conway-Maxwell-binomial distribution. Our aim was to capture correlated activity in a neuronal population without measuring correlation coefficients directly. Allowed us to capture correlated activity at very short timescales better than measuring correlation coefficients. Also parallel the finding of Churchland et al.

57

Acknowledgements

- 58 The acknowledgments and the people to thank go here, don't forget to include your project
59 advisor...

60 **Contents**

61	Declaration of Authorship	iii
62	Abstract	v
63	Acknowledgements	vii
64	1 Introduction	1
65	1.1 Overview	1
66	1.2 Modelling the fluorescence of calcium indicators	2
67	1.3 Functional networks	4
68	1.4 A new statistical model for capturing correlated behaviour	6
69	2 Sensitivity of the spikes-to-fluorescence transform to calcium indicator and neu-	
70	ron properties	9
71	2.1 Introduction	10
72	2.2 Methods	12
73	2.2.1 Calcium dynamics model	12
74	Photon release & capture	14
75	2.2.2 Parameter optimisation	15
76	Fixed parameters	16
77	2.2.3 Julia	16
78	2.2.4 Spike inference	18
79	Comparing spike inference quality	20
80	2.2.5 Perturbation analysis	20
81	2.2.6 Signal-to-noise ratio	20
82	2.2.7 Data sources	21
83	2.3 Results	21
84	2.3.1 A biophysical computational model can generate accurate fluores-	
85	cence traces from spike trains	21

86	2.3.2	Spike inference algorithms perform similarly on real data compared with time series simulated from the model	22
87	2.3.3	Relative effects of various buffers to the fluorescence signal	23
88	2.3.4	Spike inference accuracy is sensitive to indicator properties, and likely varies within and between cells	24
89	2.3.5	Single spike inference accuracy drops for high firing rates, but firing rate itself can be estimated from mean fluorescence amplitude	29
90	2.4	Discussion	31
94	3	Functional networks expand across anatomical boundaries as correlation time- scale increases	35
95	3.1	Introduction	36
96	3.2	Data	37
97	3.2.1	Brain regions	37
98	3.2.2	Video recordings	38
99	3.3	Methods	38
100	3.3.1	Binning data	38
101	3.3.2	Correlation coefficients	39
102		Total correlations, r_{SC}	39
103		Shuffled total correlations	40
104		Separating Correlations & Anti-correlations	40
105	3.3.3	Conditioning on behavioural data	40
106		Linear regression	40
107		Elastic net regularisation	41
108		Conditional covariance	41
109		Measures of conditional correlation	42
110	3.3.4	Information Theory	43
111		Entropy $H(X)$	43
112		Maximum entropy limit	43
113		Mutual Information $I(X; Y)$	44
114		Variation of Information $VI(X, Y)$	46
115		Measuring entropies & mutual information	46
116	3.3.5	Network analysis	46
117		Correlation networks	46

119	Rectified correlations	47
120	Sparsifying data networks	47
121	Communities	47
122	Weighted configuration model	48
123	Sparse weighted configuration model	48
124	Spectral rejection	48
125	Node rejection	49
126	Community detection	50
127	3.3.6 Clustering Comparison	50
128	Adjusted Rand Index	50
129	Clusterings as random variables	51
130	Information based similarity measures	52
131	Information based metrics	52
132	Comparing detected communities and anatomical divisions	53
133	3.4 Results	53
134	3.4.1 Average correlation size increases with increasing time bin width	54
135	3.4.2 Goodness-of-fit for Poisson and Gaussian distributions across increasing time bin widths	56
136	3.4.3 Differences between and inter- and intra- regional correlations decrease with increasing bin width	56
137	3.4.4 Connected and divided structure in correlation based networks reduces in dimension with increasing bin width	59
138	3.4.5 Detecting communities in correlation based networks	60
139	3.4.6 Functional communities resemble anatomical division at short timescales	63
140	3.4.7 Conditional correlations & signal correlations	63
141	3.4.8 Absolute correlations and negative rectified correlations	68
142	3.5 Discussion	69
143	4 A simple two parameter distribution for modelling neuronal activity and capturing neuronal association	75
144	4.1 Introduction	76
145	4.2 Data	77
146	4.2.1 Experimental protocol	77
147	4.3 Methods	78

152	4.3.1	Binning data	78
153	4.3.2	Number of <i>active</i> neurons	78
154	4.3.3	Moving windows for measurements	78
155	4.3.4	Fano factor	80
156	4.3.5	Probability Distributions suitable for modelling ensemble activity	80
157		Association	80
158		Binomial distribution	81
159		Beta-binomial distribution	81
160		Conway-Maxwell-binomial distribution	82
161	4.3.6	Fitting	84
162	4.3.7	Goodness-of-fit	86
163	4.4	Results	86
164	4.4.1	Increases in mean number of active neurons and variance in number of active neurons at stimulus onset in some regions	86
165		Primary visual cortex	87
166		Hippocampus	87
167		Thalamus	87
168	4.4.2	Conway-Maxwell-binomial distribution is usually a better fit than binomial or beta-binomial	87
169	4.4.3	Conway-Maxwell-binomial distribution captures changes in association at stimulus onset	92
170	4.4.4	Replicating stimulus related quenching of neural variability	92
171	4.5	Discussion	94
172	5	Studies with practical limitations & negative results	97
173	5.1	Dynamic state space model of pairwise and higher order neuronal correlations	98
174	5.2	A multiscale model for hierarchical data applied to neuronal data	98
175	6	Discussion	101
176	Bibliography		109

181 List of Figures

182 2.1	A: Example spike train (blue) and the corresponding GCaMP6s fluorescence 183 trace (green), data replotted from (Berens et al., 2018). Inset shows zoomed 184 section of traces to highlight slow decay of GCaMP6s fluorescence relative 185 to spike time intervals. B: Schematic diagram of the neuron calcium and 186 GCaMP computational model. C: Good visual match of data fluorescence 187 trace (green) and model simulated fluorescence (orange) in response to an 188 identical spike train (blue).	11
189 2.2	A: Workflow to compare spike inference for real versus simulated fluores- 190 cence data. B: True positive rates achieved by three different spike inference 191 algorithms when applied to observed spike trains, and simulated spike trains. 192 Data points overlaid as blue circles. The performance is similar from real 193 and simulated data for each of the algorithms.	23
194 2.3	Calcium Buffering Dynamics (a) The proportions of bound and free cal- 195 cium concentrations within a cell, with the associated spike train. (b)-(f) The 196 dynamics of the concentration of (b) excited indicator bound calcium, (c) in- 197 dicator bound calcium, (d) immobile endogenous buffer bound calcium, (e) 198 mobile endogenous buffer bound calcium, and (f) free calcium in response to 199 an action potential at $\sim 23.2\text{s}$	25
200 2.4	(a) An example trace for each of the five pairs of values used for the binding 201 and unbinding rates of the fluorescent calcium indicator. (b) The signal-to- 202 noise ratio of the modelled fluorescence traces using each of the four per- 203 turbed value pairs, and the experimental value. The SNRs for the value pairs 204 perturbed downward are lower than that for the unperturbed value pair or 205 the higher value pairs. (c) The true-positive rates of the deconvolution al- 206 gorithm's predictions when inferring from the observed data, and inferring 207 from modelled traces using the perturbed and experimental values.	27

208	2.5 (a) An example trace for each of the five perturbed values for the concentration of fluorescent calcium indicator. The top two traces are produced by the lower perturbed values, the middle trace is produced by the experimental value, and the lowest two traces are produced when using the higher perturbed values. (b) The signal-to-noise ratio of the modelled fluorescence traces using each of the four perturbed values, and the experimental value. Extreme perturbations of the concentration either above or below the experimental level lowered the SNR. (c) The true-positive rates of the deconvolution algorithm's predictions when inferring from the observed data, and inferring from modelled traces using the perturbed and experimental values. We found that the algorithms performs equally badly on the two most extreme values, and performs equally well on the experimental value, and the next higher perturbed value.	28
221	2.6 (a) An example trace for each of the five perturbed values for the concentration of immobile endogenous buffer. (b) The signal-to-noise ratio of the modelled fluorescence traces using each of the four perturbed values, and the experimental value. The lower values for the immobile buffer produce the same SNR as the experimental value. But the higher perturbed values produce fluorescence traces with a lower SNR. (c) The true-positive rates of the deconvolution algorithm's predictions when inferring from the observed data, and inferring from modelled traces using the perturbed and experimental values.	30
230	2.7 Simulating fluorescence traces at different firing rates Example modelled traces created using simulated spike trains with a mean firing rate of 1Hz (left column), 5Hz (middle column), and 10Hz (right column). Note the difference in amplitude with different mean firing rates.	31
234	2.8 Inference quality and $\Delta F/F_0$ vs Firing rate (left) The spike inference accuracy when applied to 30 traces created using simulated spike trains with mean firing rates of 1, 5, and 10 Hz. (right) The mean $\Delta F/F_0$ across those 30 traces for each frequency.	32
238	3.1 Probe Locations: The locations of the probes in each of the three mouse brains (Stringer et al., 2019).	38

240	3.2 Entropy Limit: The upper limit on entropy of binned spike count data as 241 a function of the maximum observed spike count. The orange line is the 242 analytical maximum. The blue line is the entropy of samples with $N = 1000$ 243 data points taken from the discrete uniform distribution.	44
244	3.3 (A) An example of the correlation coefficients between two different pairs 245 of cells, one where both cells are in the same brain region (intra-regional 246 pair), and one where both cells are in different brain regions (inter-regional 247 pair). The correlation coefficients have been measured using different time 248 bin widths, ranging from 5ms to 3s. Note the increasing amplitude of the 249 correlations with increasing bin width. (B) A raster plot showing the spike 250 times of each pair of cells.	54
251	3.4 Mean correlation coefficients measured from pairs of 50 randomly chosen 252 neurons. (A) All possible pairs, (B) positively correlated pairs, and (C) neg- 253 atively correlated pairs. (D) Mean and standard error of χ^2 test statistics for 254 Poisson and Gaussian distributions fitted to neuron spike counts.	55
255	3.5 (Left)The mean intra-region and inter-region correlations using all possible 256 pairs of ~ 500 neurons, spread across 9 different brain regions. (Right) 257 Courtesy of Stringer et al. (2019), mean inter-regional (out-of-area) correla- 258 tion coefficients vs mean intra-regional (within-area) correlation coefficients 259 for a bin width of 1.2s. Note that the intra-regional coefficients are higher in 260 each case.	57
261	3.6 The mean intra-regional correlations (coloured dots) and mean inter-regional 262 correlations (black dots) for a given region, indicated on the x-axis, for dif- 263 ferent time bin widths. Each black dot represents the mean inter-regional 264 correlations between the region indicated on the x-axis and one other region. 265 (A) shows these measurements when we used a time bin width of 5ms. (B) 266 shows these measurements when we used a time bin width of 1s. Note that 267 the difference between the mean inter-regional correlations and mean intra- 268 regional correlations is smaller for 1s bins.	58
269	3.7 Mean inter-regional (main diagonal) and intra-regional (off diagonal) corre- 270 lation coefficients. (A) Shows these measurements when spike times were 271 binned using 5ms time bins. (B) Shows the same, using 1s time bins. Note 272 that the matrices are ordered according to the main diagonal values, therefore 273 the ordering is different in each subfigure.	59

304	3.13 Matrices showing the regional membership of pairs by colour, and the com-	
305	munities in which those pairs lie. (A-B) Detected communities and regional	
306	membership matrix for network based on rectified spike count correlation	
307	$\rho_{X,Y Z}$, using time bin widths of 0.005s and 1s respectively. (C-D) Detected	
308	communities and regional membership matrix for network based on rectified	
309	signal correlation ρ_{signal} , using time bin widths of 0.005s and 1s respectively.	67
310	3.14 Distance and similarity measures between the anatomical division of the neu-	
311	rons, and the communities detected in the network based on the spike count	
312	correlations $\rho_{X,Y Z}$. (A) The variation of information is a ‘distance’ mea-	
313	sure between clusterings. The distance between the anatomical ‘clustering’	
314	and the community clustering increases as the time bin width increases. (B)	
315	The adjusted Rand index is a similarity measure between clusterings. The	
316	detected communities become less similar to the anatomical division of the	
317	cells as the time bin width increases.	68
318	3.15 Distance and similarity measures between the anatomical division of the neu-	
319	rons, and the communities detected in the network based on the signal cor-	
320	relations ρ_{signal} . (A) The variation of information is a ‘distance’ measure be-	
321	tween clusterings. The distance between the anatomical ‘clustering’ and the	
322	community clustering increases as the time bin width increases. (B) The ad-	
323	justed Rand index is a similarity measure between clusterings. The detected	
324	communities become less similar to the anatomical division of the cells as	
325	the time bin width increases.	69
326	3.16 (A-B) Absolute correlation matrices with detected communities indicated by	
327	white lines. These communities are based on the absolute value of the total	
328	correlation between each pair of cells. Those entries within a white square in-	
329	dicate that both of those neurons are in the same community. Matrices shown	
330	are for 5ms and 1s time bin widths respectively. Main diagonal entries were	
331	set to 0. (C-D) Matrices showing the anatomical distribution of pairs along	
332	with their community membership. Regional membership is indicated by the	
333	colour bar. (E) Variation of information between the anatomical division of	
334	the cells, and the detected communities. (F) Adjusted Rand index between	
335	the anatomical division, and the detected communities.	70

336	3.17 (A-B) Sign reversed rectified correlation matrices with detected communities indicated by white lines. Those entries within a white square indicate that both of those neurons are in the same community. Matrices shown are for 5ms and 1s time bin widths respectively. Main diagonal entries were set to 0. (C-D) Matrices showing the anatomical distribution of pairs along with their community membership. Regional membership is indicated by the colour bar. (E) Variation of information between the anatomical division of the cells, and the detected communities. (F) Adjusted Rand index between the anatomical division, and the detected communities.	71
345	4.1 Figures showing the over-dispersion possible for a beta-binomial distribution relative to a binomial distribution. Parameters are shown in the captions. . .	82
347	4.2 Figures showing (A) the under-dispersion and (B) over-dispersion permitted by the COMb distribution relative to a binomial distribution. (C) illustrates that the p parameter of the COMb distribution does not correspond to the mean of the distribution, as it does for the binomial and beta-binomial distributions. (D) shows a heatmap for the value of the Kullback-Liebler divergence between the COMb distribution and the standard binomial distribution with same value for n , as a function of p and ν . Parameters are shown in the captions.	85
355	4.3 (A) Raster plot showing the spikes fired by 33 randomly chosen neurons in the primary visual cortex. (B-C) (B) average and (C) variance of the number of active neurons, measured using a sliding window 100ms wide, split into 100 bins. The midpoint of the time interval for each window is used as the timepoint (x-axis point) for the measurements using that window. The grey shaded area indicates the presence of a visual stimulus. The opaque line is an average across the 160 trials that included a visual stimulus of any kind. We can see a transient increase in the average number of active neurons and the variance of this number, followed by a fluctuation and another increase. .	88

364	4.4 (A) Raster plot showing the spikes fired by 33 randomly chosen neurons in 365 the hippocampus. (B-C) (B) average and (C) variance of the number of active 366 neurons, measured using a sliding window 100ms wide, split into 100 bins. 367 The midpoint of the time interval for each window is used as the timepoint (x- 368 axis point) for the measurements using that window. The grey shaded area 369 indicates the presence of a visual stimulus. The opaque line is an average 370 across the 160 trials that included a visual stimulus of any kind. We can see 371 a transient increase in the average number of active neurons and the variance 372 of this number at stimulus onset.	89
373	4.5 (A) Raster plot showing the spikes fired by 33 randomly chosen neurons in 374 the thalamus. (B-C) (B) average and (C) variance of the number of active 375 neurons, measured using a sliding window 100ms wide, split into 100 bins. 376 The midpoint of the time interval for each window is used as the timepoint (x- 377 axis point) for the measurements using that window. The grey shaded area 378 indicates the presence of a visual stimulus. The opaque line is an average 379 across the 160 trials that included a visual stimulus of any kind. We can 380 see in immediate increase at stimulus onset, a subsequent fall, and another 381 sustained increased until the stimulus presentation ends.	90
382	4.6 (A) An example of the binomial, beta-binomial, and Conway-Maxwell-binomial 383 distributions fitted to a sample of neural activity. The Conway-Maxwell- 384 binomial distribution is the best fit in this case. The histogram shows the 385 empirical distribution of the sample. The probability mass function of each 386 distribution is indicated by a different coloured line. (B) Across all samples 387 in all trials, the proportion of samples for which each fitted distribution was 388 the the best fit. The Conway-Maxwell-binomial distribution was the best fit 389 for 93% of the samples taken from V1 using a bin width of 1ms.	91

390	4.7 (A) We fit a Conway-Maxwell-binomial distribution to the number of active	
391	neurons in 1ms time bins of a 100ms sliding window. We did this for all	
392	trials with a visual stimulus and took the average across those trials. We	
393	see a transient drop in value for the distribution's ν parameter at stimulus	
394	onset. This shows an increase in association between the neurons. (B) We	
395	measured the correlation coefficient between the spike counts of all possible	
396	pairs of neurons in the same sliding window. The took the average of those	
397	coefficients. We also did this for every visually stimulated trial, and took	
398	the average across trials. The increase in association is not reflected with an	
399	increase in average correlation.	93
400	4.8 (A) The mean Fano factor of the spike counts of the cells in the primary visual	
401	cortex. Means were taken across cells first, then across trials. There was a	
402	significant decrease in the Fano factors immediately after stimulus onset. (B)	
403	The mean Fano factor of the spike counts of the cells in the motor cortex. No	
404	significant change in measurements at any point.	94

405 List of Tables

406	2.1	Fixed parameters A table of the parameters fixed before optimising the		
407		model. The values of these parameters could be changed to model differ-		
408		ent fluorescent calcium indicators.	17	
409	4.1	Details of the different bin width and analysis window sizes used when bin-		
410		ning spike times, and analysing those data.	79	
411	4.2	Relative dispersion of the COMb distribution, and association between Bernoulli		
412		variables as represented by the value of the ν parameter.	84	
413	4.3	Proportion of samples for which each distribution was the best fit, grouped		
414		by bin width. The COMb distribution is the best fit most of the time.	92	

⁴¹⁵ **List of Abbreviations**

COMb Conway-Maxwell-binomial (distribution)

OASIS Online active set method to infer spikes

SNR Signal to noise ratio

⁴¹⁶ **List of Symbols**

$[Ca^{2+}]$	Free calcium concentration	mol
$[BCa]$	Fluorescent indicator bound calcium	mol
$[ECa]$	Endogenous mobile buffer bound calcium	mol
$[ImCa]$	Immobile mobile buffer bound calcium	mol
$[BCa^*]$	excited fluorescent indicator bound calcium	mol
k_{X_f}	binding (affinity) rate	s^{-1}
k_{X_b}	unbinding (dissociation) rate	s^{-1}

For/Dedicated to/To my...

418 **Chapter 1**

419 **Introduction**

420 **1.1 Overview**

421 Since Hodgkin and Huxley's squid experiments featuring a single axon (Hodgkin and Hux-
422 ley, 1939), to more recent research with spike sorted data from ~ 24000 neurons from 34
423 brain regions from 21 mice (Allen et al., 2019), the number of neurons contributing to elec-
424 trophysiological datasets has been growing. The number of simultaneously recorded neurons
425 has doubled approximately every seven years since the use of multi-electrode recording in
426 neuroscience began (Stevenson and Kording, 2011). Recording methods using two-photon
427 calcium imaging have also been used to extract data from populations containing over 10000
428 neurons (Peron et al., 2015). This dramatic growth in the number of neurons available for
429 analysis requires a dramatic change in analysis methods.

430 There are multiple methods for reading activity from neuronal ensembles: electrophysiolog-
431 ogy, calcium imaging, and voltage imaging. Electrophysiology involves inserting electrodes
432 into the brain of an animal. The electrodes read extra-cellular membrane potential, and using
433 these readings we observe activity in the ensemble. Calcium imaging and voltage imaging
434 use indicator dyes or fluorescent proteins that emit fluorescence traces that indicate either
435 the concentration of calcium in a neuron's cytoplasm, or the neuron's membrane potential.
436 In this project, we have attempted to address some of the difficulties in collecting data from
437 these large ensembles using fluorescent calcium indicators, and some of the difficulties in
438 analysing the collected data.

439 The rest of this introductory chapter will give some background about methods of record-
440 ing from the brain, and some background for the rest of the document. Chapter two describes
441 a biophysical model for the fluorescence trace induced by a given spike train in a cell con-
442 taining a fluorescent calcium indicator. Our third chapter describes our investigations into

443 the correlated activity across different regions of a mouse behaving spontaneously. We ap-
444 plied a novel community detection method (Humphries et al., 2019) from network science
445 to correlation based networks of neurons, and observed differences in the structure of these
446 correlations at different timescales. In our fourth chapter, we detail a new statistical model
447 for the number of neurons spiking in a neuronal ensemble at any given moment. With this
448 model, we attempted to capture correlated activity in a new way. The fifth chapter is a brief
449 description of the work that yielded negative results or was abandoned. The final chapter is a
450 discussion of our work and results from the previous chapters and their implications.

451 1.2 Modelling the fluorescence of calcium indicators

452 To focus on calcium imaging for a start, a neuron that contains a fluorescent calcium indicator
453 in its cytoplasm will fluoresce when bombarded with photons. The amount that the cell
454 will fluoresce is dependent on the concentration of fluorescent indicator within the cell, and
455 the concentration of calcium within the cell. When a neuron fires an action potential, the
456 influx of free calcium ions causes an increase in fluorescence when those ions bond with the
457 fluorescent indicator and those bounded molecules are bombarded with photons. After the
458 action potential, as calcium is extruded from the cell the fluorescence returns to a baseline
459 level. This is the basic mechanism of fluorescent calcium indicator based imaging.

460 This method has some advantages over electrophysiology as measure of neuronal ensem-
461 ble activity. Many of the problems with electrophysiology are within the processes used to
462 isolate spikes in the extracellular voltage readings, and assign these spikes to individual cells.
463 These processes are collectively called ‘spike sorting’. A comparison of many different spike
464 sorting algorithms found that these algorithms only agreed on a fraction of cases (Buccino
465 et al., 2019). Furthermore, because electrodes measure extracellular voltage, neurons that do
466 not spike will not be detected. Isolating individual neurons is easier and more reliable when
467 using calcium imaging data, because cells will emit a baseline level of fluorescence when not
468 firing action potentials. Another advantage is that calcium imaging sites can be re-used for
469 weeks for longitudinal studies (Chen et al., 2013). One of the methods of delivering the flu-
470 orescent indicator is by adeno-associated viruses, consequently there can be problems with
471 indicator gradients around the infection site, and expression levels will change in individual
472 cells over weeks (Tian et al., 2009; Chen et al., 2013). This delivery method can also cause
473 cell pathology, and nuclear filling (Zariwala et al., 2012), but these problems can be solved by
474 using lines of transgenic mice (Dana et al., 2014). The fluorescence signal itself can serve a a

475 good indicator of cell activity, but similarly to electrophysiology, the aim of calcium imaging
476 is often spike detection.

477 If the imaging data is collected at a high enough frequency, and the signal-to-noise ratio
478 of the fluorescence trace is high enough, it should be possible to infer the spike times to some
479 level of accuracy. For example, the calmodulin based indicator GCaMP6s has a sufficiently
480 high signal-to-noise ratio that isolated action potentials can be detected and inferred (Chen
481 et al., 2013). Many spike inference algorithms exist (Vogelstein et al., 2010; Pnevmatikakis
482 et al., 2016; Friedrich and Paninski, 2016; Pnevmatikakis et al., 2013; Pnevmatikakis et al.,
483 2014; Deneux et al., 2016; Greenberg et al., 2018), and some of these can perform both cell
484 isolation and spike detection simultaneously (Vogelstein et al., 2010; Pnevmatikakis et al.,
485 2016; Pnevmatikakis et al., 2014; Deneux et al., 2016). But the relationship between spik-
486 ing and fluorescence change is not fully understood. For example, the fluorescent indicator
487 will act like an additional calcium buffer within the cell cytoplasm and will compete with
488 the other endogenous buffers to bind with free calcium ions. Therefore, the concentration
489 of those endogenous buffers, and the binding dynamics of those buffers will have an effect
490 on the change in fluorescence in response to an action potential. Furthermore, the binding
491 dynamics of the fluorescent indicator itself will have an effect on the change in fluorescence.
492 For example, the GCaMP series of fluorescence indicators are based on the calcium buffer
493 protein calmodulin. This protein has four binding sites, whose affinities interact non-linearly.
494 But most of the spike inference algorithms model the fluorescence as a linear function of
495 a calcium trace, and they model this calcium trace as a first or second order autoregression
496 with a pulse input to represent action potentials. Deneux et al. (2016) developed two dif-
497 ferent calcium fluorescence models behind their spike inference algorithm (MLspike) with a
498 more biological inspiration. For their simpler model, they take a physiological approach and
499 account for baseline calcium indicator dynamics. They end up with a system of first order
500 differential equations defining the dynamics of calcium concentration, baseline fluorescence,
501 and fluorescence. For their more complicated model specifically for genetically encoded cal-
502 cium indicators, they also took into account indicator binding and unbinding rates, which
503 added another equation to their system of equations. The algorithms that use the autore-
504 gression model and the MLspike algorithm are outperformed by the most recently published
505 spike inference algorithm (Greenberg et al., 2018). This algorithm takes into account the
506 binding dynamics of both the endogenous buffers and fluorescent calcium indicator, and the
507 concentrations of free calcium, indicator, and endogenous buffer within the cell cytoplasm.
508 The performance of this algorithm shows that there is value in more biologically inspired

509 models of fluorescent calcium indicators.

510 In light of the growing popularity of two-photon calcium imaging, and the lack of biolog-
511 ically inspired spike inference algorithms (Greenberg et al. developed their spike inference
512 algorithm in parallel to our work), we decided to develop a biologically inspired model for
513 fluorescent calcium indicator fluorescence. The idea being that our model would take a spike
514 train, or simply spike times, provided by the user, and return the fluorescence trace that would
515 be induced by this spike train or spike times. The model contains parameters for concentra-
516 tions of indicator and endogenous buffers, as well as affinity and unbinding rates for these
517 buffers. There are also parameters for the baseline concentration of free calcium in the cell
518 cytoplasm, and the cell radius (as a means for calculating the cell volume). With this model,
519 we hoped that experimentalists would be able to test out different calcium indicators on the
520 types of spike trains that they expect to encounter. This way they could decide ahead of time
521 which indicator suited their situation best. Since the output of our model is a fluorescence
522 trace, the spike inference models mentioned above can be applied to the modelled fluores-
523 cence. This means that the model could also be used to benchmark the performance of these
524 spike inference algorithms, and to investigate the impact of variations in the model on spike
525 inference accuracy.

526 1.3 Functional networks

527 We have outlined some of the advantages that calcium imaging has over electrophysiology.
528 But electrophysiology is more useful in some situations. One particular drawback for two-
529 photon calcium imaging is that usually it can only be used for imaging near to the surface
530 of the brain. This problem can be solved by removing the tissue around the area to be im-
531 aged, and custom building a two-photon microscope Dombeck et al., 2010. Imaging with
532 three (or presumably more) photons may solve this problem in the future (Ouzounov et al.,
533 2017). A better option for reading activity from neurons beyond the surface of the brain is to
534 use Neuropixels probes (Jun et al., 2017). These probes can be used to read from thousands
535 of neurons simultaneously in many different areas of the brain (Allen et al., 2019; Stringer
536 et al., 2019; Steinmetz, Carandini, and Harris, 2019; Steinmetz et al., 2019). This brings us
537 to another problem for which we require new innovations in our analysis methods. Specif-
538 ically, analysing correlated behaviour in neural ensembles consisting of neurons from many
539 different brain regions.

540 Until the invention of new technologies such as the Neuropixels probes, most elec-
541 trophysiology datasets read from neurons in only one or two regions. Therefore most of
542 the research on interactions between neurons in different regions is limited to two regions
543 (Wierzynski et al., 2009; Patterson et al., 2014; Girard, Hupé, and Bullier, 2001). In chapters
544 3 and 4 we used datasets with neurons from 9 and 5 different brain regions respectively. In
545 their review of the interaction between growing the number of neurons in datasets and the
546 analysis methods applied to those dataset, Stevenson and Kording (2011) assert that an im-
547 portant objective of computational neuroscience is to find order in these kinds multi-neuron
548 of datasets. This was our main aim for the research described in chapter 3.

549 In light of recent findings based on correlated behaviour showing that spontaneous be-
550 haviours explain activity in many different parts of the brain that would otherwise be regarded
551 as noise (Stringer et al., 2019), that satiety is represented brain wide (Allen et al., 2019), and
552 that exploratory and non-exploratory states are represented in the amygdala (Gründemann
553 et al., 2019), it was clear that state representation or motor control had an influence on cor-
554 related behaviour in areas of the brain not usually associated with these tasks. Also, given
555 differences in timescales of fluctuations in different brain regions (Murray et al., 2014), and
556 different timescales for event representation in different brain regions (Baldassano et al.,
557 2017), we decided to investigate brain wide correlated behaviour at timescales ranging from
558 5ms up to 3s.

559 We started off measuring the correlations in spike counts between individual neurons in
560 our ensemble. These measurements induced a weighted undirected graph where each node
561 represented a neuron, and the weight of each edge was the strength of the correlation be-
562 tween the neurons represented by the nodes at either end of that edge. In order to put the
563 neurons into groups with correlated behaviour, we applied a novel community detection al-
564 gorithm (Humphries et al., 2019) to this graph. We repeated this analysis for timescales
565 from milliseconds to seconds. Bear in mind that our correlation based graph was completely
566 agnostic of the anatomical regions in which our cells resided. We then compared our corre-
567 lated communities to their anatomy at each timescale. In this way, we used a novel method,
568 never applied neuronal data before, to analyse the makeup of correlated communities across
569 different regions at different timescales.

570 1.4 A new statistical model for capturing correlated behaviour

571 Many important findings have been made by measuring the correlations between binned
572 spike counts, but there are some problems with this method of analysis. Firstly, the width
573 of the bins used to bin spike times into spike counts has an effect on the magnitude of the
574 correlations measured. Using a short bin width can cause your measurements to be artificially
575 small (Cohen and Kohn, 2011). This may not be an issue if one is considering relative size of
576 correlations when using the same bin width, but it is still not ideal. Secondly, while pairwise
577 correlations can capture most of the information in a small network (up to 40 cells) of highly
578 correlated cells (Schneidman et al., 2006), a model based on pairwise correlations alone will
579 fail to capture the activity of larger (~ 100 cells) networks, higher order correlated activity
580 is required (Ganmor, Segev, and Schneidman, 2011). One problem with these higher order
581 correlations is that they may be defined in different ways (Staude, Grün, and Rotter, 2010).
582 Furthermore if we want to include them in a model this usually involves greatly increasing the
583 number of parameters to fit, which increases the dimension of the parameter space leading
584 to the ‘curse of dimensionality’. Some models attempt to sidestep these problems while
585 still capturing higher-order correlations. These models attempt to capture the relationship
586 between each individual neuron in the ensemble, and the ensemble as a whole. Okun et al
587 (2015) called the strength of this relationship the ‘population coupling’, and demonstrated
588 that this quantity can predict an individual neuron’s response to optogenetic stimulation of
589 the whole ensemble. They also showed that this quantity was an indicator of the neuron’s
590 synaptic connectivity (Okun et al., 2015). With the ‘population tracking model’, O’Donnell
591 et al. (2016) linked the probability of firing an action potential for each individual neuron
592 with the distribution of the number of active neurons. This allowed model fitting for a large
593 number of neurons, as well as calculation of full pattern probabilities, and population entropy
594 (O’Donnell et al., 2017).

595 In this work, we also aimed to capture correlated behaviour between the neurons in a
596 neuronal ensemble without measuring correlations directly. Correlation coefficients capture
597 the linear component of the relationship between two random variables, but will not mea-
598 sure any relationship beyond linearity. Also, measuring correlation coefficients using short
599 timebins can be difficult for neuronal data (Cohen and Kohn, 2011). We decided to abandon
600 correlation, and we aimed to quantify a more general concept of association by modelling
601 the number of active neurons in the ensemble using a Conway-Maxwell-binomial (COMb)
602 distribution (Kadane, 2016).

603 The COMb distribution is a probability distribution over the number of successes in a
604 sequence of Bernoulli trials, where these trials can be associated in some way. The COMb
605 distribution is an extension of the standard binomial distribution, with an additional parameter
606 to model association between the Bernoulli variables. Using this additional parameter the
607 distribution can capture positive association, where the Bernoulli variables tend to take the
608 same value, negative association, where the Bernoulli variables tend to take opposite values,
609 or no association i.e. the standard binomial distribution.

610 We fit a COMb distribution to spike sorted electrophysiological data taken from five
611 different regions in the brain of an awake mouse exposed to visual stimuli (Steinmetz et al.,
612 2019). We examined whether or not a model based on the COMb distribution was able to
613 capture changes in the number of active neurons in these neuronal ensembles in response to
614 the stimuli. We also investigated the relationship between the changes as captured by the
615 COMb model and the change in neural variability as measured by Churchland et al. in their
616 famous paper (Churchland et al., 2010).

617 Our overall aim was to investigate some of the challenges in analysing large ensembles
618 of neurons present today. That included collecting the data to analyse (via calcium imaging),
619 and subsequently analysing these data. We felt that this was a worthwhile project because
620 the size of datasets, in terms of numbers of neurons and data collected, is growing rapidly.
621 Consequently these challenges will only become greater unless they are addressed. This is
622 our attempt at addressing them.

623 **Chapter 2**

624 **Sensitivity of the
spikes-to-fluorescence transform to
calcium indicator and neuron
properties**

628 *Abstract*

629 Fluorescent calcium indicators such as GCaMP are widely used to monitor neuronal activity.
630 However the relationship between the fluorescence signal and the underlying action potential
631 firing is poorly understood. This lack of knowledge makes it difficult for experimenters
632 to decide between different indicator variants for a given application. We addressed this
633 problem by studying a basic biophysical model of calcium dynamics in neuronal soma. We
634 fit the model parameters to publicly available data where GCaMP6s fluorescence and whole-
635 cell electrophysiological recordings were made simultaneously in the same single neurons.
636 We systematically varied the model's parameters to characterise the sensitivity of spike train
637 inference algorithms to the calcium indicator's main biophysical properties: binding rate,
638 dissociation rate, and molecular concentration. This model should have two potential uses:
639 experimental researchers may use it to help them select the optimal indicator for their desired
640 experiment; and computational researchers may use it to generate simulated data to aid design
641 of spike inference algorithms.

642

2.1 Introduction

643 Although fluorescent calcium indicators such as GCaMP are widely used to monitor neuronal
644 activity, the relationship between the fluorescence signal and the underlying action potential
645 firing is imperfect. The fluorescence signal has a low signal-to-noise ratio, and most indica-
646 tors' kinetics are slow relative to the millisecond-timescale dynamics of the membrane volt-
647 age (example in figure 2.1A). This makes spike inference difficult. Furthermore, the effects
648 of the indicator and cell properties on the fluorescence signal are unknown. For example,
649 genetically encoded indicators can accumulate within neurons over weeks and months (Chen
650 et al., 2013). Studies using calcium-sensitive fluorescent dyes have shown that indicator con-
651 centration has substantial effects on the spike-to-fluorescence relationship (Maravall et al.,
652 2000). Therefore spike rates inferred from GCaMP fluorescence signals may give mislead-
653 ing results if comparing across imaging sessions. More generally, the poor understanding of
654 the spike-to-fluorescence transform means experimenters may not know whether to trust the
655 outputs of spike train inference methods in any given application.

656 Spike trains are usually inferred from the time series of intensity values of one pixel of the
657 fluorescence image, where the pixel is located at the cell's soma. The problems of identifying
658 these pixels, and inferring spikes from their time series can solved separately or together.
659 When attempting to infer spikes, the fluorescence trace is modelled as a linear combination of
660 calcium concentration dynamics, a baseline calcium concentration, and some Gaussian noise.
661 The calcium concentration dynamics are modelled as an autoregressive process of degree 1
662 or 2 with a pulse input corresponding to the spike train, or the number of spikes fired in a
663 time step. The model includes no dynamics for the fluorescent indicator itself. Furthermore,
664 in order to make this model into an easily solvable linear programming problem the number
665 of spikes fired in a timestep is not restricted to non-negative integers but to arbitrary non-
666 negative values (Vogelstein et al., 2010; Pnevmatikakis et al., 2016; Friedrich and Paninski,
667 2016; Pnevmatikakis et al., 2013; Pnevmatikakis et al., 2014). More biologically inspired
668 spike inference models do exist (Deneux et al., 2016), but their fundamentals are very similar.
669 In this work, we investigated the effect of changing dynamics and buffer concentrations on
670 the accuracy of the inference algorithms based on these models.

671 The aim of this project was to model the fluorescence traces produced by a fluorescent
672 calcium indicator in a neuron soma resulting from a specific spike train, given calcium indi-
673 cator parameters such as binding rate, dissociation rate, and molecular concentration. Such

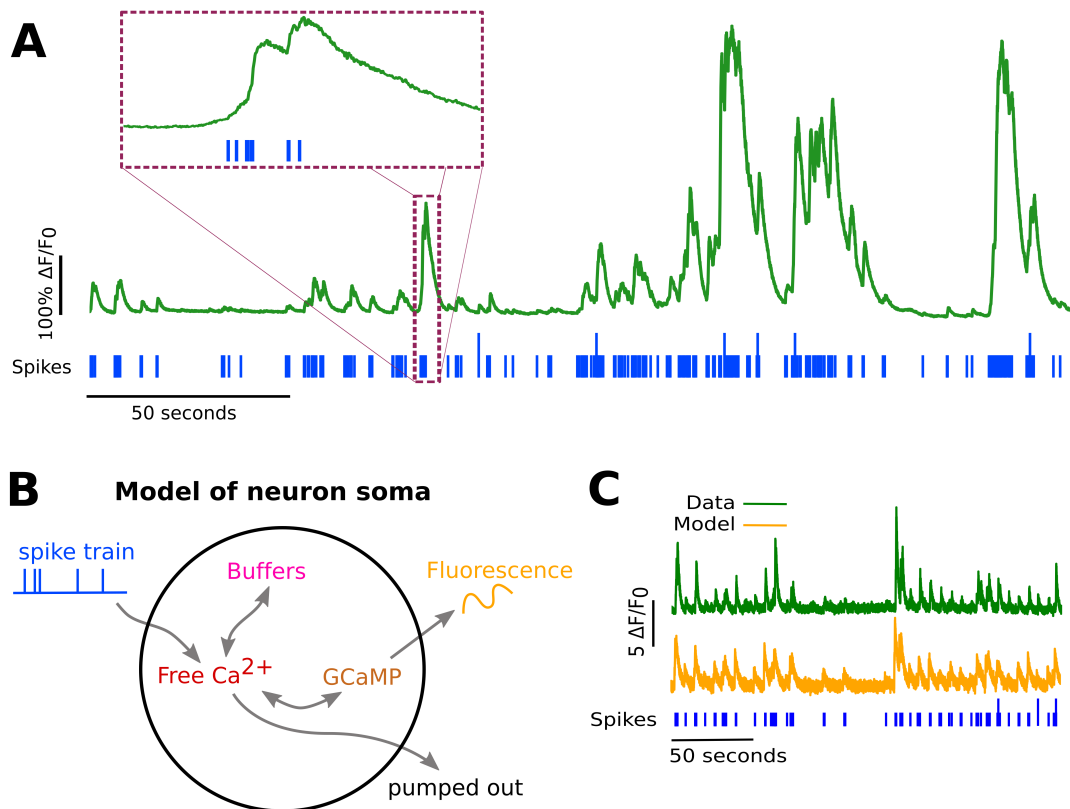


FIGURE 2.1:

A: Example spike train (blue) and the corresponding GCaMP6s fluorescence trace (green), data replotted from (Berens et al., 2018). Inset shows zoomed section of traces to highlight slow decay of GCaMP6s fluorescence relative to spike time intervals.

B: Schematic diagram of the neuron calcium and GCaMP computational model.

C: Good visual match of data fluorescence trace (green) and model simulated fluorescence (orange) in response to an identical spike train (blue).

674 a model would allow benchmarking of various spike inference algorithms, and enable under-
675 standing of how indicator characteristics affect the quality of spike train inference.

676 The model we developed consisted of free calcium, fluorescent indicator molecules, and
677 mobile and immobile endogenous calcium buffers. The indicator molecules which were
678 bound to a calcium molecule could be either excited, i.e. able to release a photon, or relaxed.
679 In order to reproduce the noise inherent in the data collection, we modelled the release of
680 photons from the excited indicator bound calcium as a stochastic process.

681 The fluorescence traces produced by the simulation were calibrated to reproduce the
682 signal-to-noise ratio observed in experimental data. Previously published spike inference
683 algorithms were then used to infer spike trains from the experimental fluorescence traces and
684 the modelled fluorescence traces. The parameters of the model were then varied in order to
685 determine the effect on the system dynamics and the effects on spike inference.

686 2.2 Methods

687 2.2.1 Calcium dynamics model

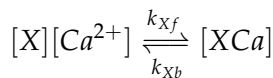
688 We wrote a biophysical model of the calcium dynamics within a cell soma. When a neu-
689 ron fires an action potential, voltage-dependent calcium ion-channels open up that allow a
690 current of Ca^{2+} to flow into the neuron (Koch, 1999). The increase in the free calcium ion
691 concentration inside of the cell, along with changes in the concentration of potassium and
692 sodium, causes the change in cell membrane potential, which must be depolarised. The de-
693 polarising process consists of free calcium ions leaving the cell through open ion channels,
694 or binding to molecules within the cell called buffers, or calcium storage by organelles such
695 as the endoplasmic reticulum. A diagram illustrating the cell, its channels, and its buffers
696 can be seen in figure 2.1A. There are several different types of calcium buffer, each with
697 different dynamics and different concentrations within different types of excitable cell. The
698 fluorescent calcium indicator is another calcium buffer, with the useful property that when it
699 is bound to a calcium ion, the bound molecule may become excited by a photon and release
700 a photon in return. This is what creates the fluorescence. After the action potential has taken
701 place, the free calcium concentration within the cell will return to a baseline level (Maravall
702 et al., 2000).

703 We modelled the the dynamics of five molecular concentrations,

- 704 • Free calcium ion concentration, $[\text{Ca}^{2+}]$

- 705 • Fluorescent indicator bound calcium, $[BCa]$
- 706 • Endogenous mobile buffer bound calcium, $[ECa]$
- 707 • Endogenous immobile buffer bound calcium, $[ImCa]$
- 708 • Excited buffered calcium, $[BCa^*]$

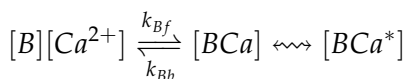
The term ‘buffering’ refers to free calcium ions coming into contact with buffer molecules and binding together. Diagrammatically:



709 where $[X]$ represents any buffer molecule, and k_{X_f} and k_{X_b} represent the binding and un-
 710 binding (dissociation) rates in units of per molar concentration per second ($M^{-1} s^{-1}$) and per
 711 second (s^{-1}) respectively. The speed of this chemical reaction is determined by the binding
 712 and unbinding rates.

713 There are a number different endogenous buffers in any neuron. Which buffers are
 714 present, and the buffers’ concentrations vary from cell to cell. In order to capture the ef-
 715 fects of mobile and immobile endogenous buffers without introducing several parameters,
 716 they were modelled as two buffers. One representing mobile buffers and the other represent-
 717 ing immobile buffers. Each with their own binding and unbinding rates.

The fluorescent calcium indicator behaves similarly to the other calcium buffers. The calcium is buffered by the indicator in the same way. But an indicator bound calcium molecule can become excited by absorbing the energy from a photon. An excited indicator bound calcium molecule can then release a photon to go back to its ‘relaxed’ state.



718 The released photons are captured by a photon collector. This gives us the fluorescence trace.
 719 Ignoring the baseline level of free calcium in a neuron, the system of equations we used
 720 to model all of these interactions is as follows:

$$\begin{aligned} \frac{d[Ca^{2+}]}{dt} = & k_{Bb}[BCa] + k_{Eb}[ECa] + k_{Imb}[ImCa] \\ & - k_{Bf}[B][Ca^{2+}] - k_{Ef}[E][Ca^{2+}] - k_{Imf}[Im][Ca^{2+}] \\ & + \beta([Ca_0^{2+}] - [Ca^{2+}]) \end{aligned} \quad (2.1)$$

$$\frac{d[BCa]}{dt} = k_{Bf}[B][Ca^{2+}] - k_{Bb}[BCa] + r[BCa^*] - e[BCa] \quad (2.2)$$

$$\frac{d[ECa]}{dt} = k_{Ef}[E][Ca^{2+}] - k_{Eb}[ECa] \quad (2.3)$$

$$\frac{d[ImCa]}{dt} = k_{Imf}[Im][Ca^{2+}] - k_{Imb}[ImCa] \quad (2.4)$$

$$\frac{d[BCa^*]}{dt} = \eta[BCa] - r[BCa^*] \quad (2.5)$$

721 where $[Ca_0^{2+}]$ is the baseline calcium concentration within the cell soma, β is a rate defining
722 how quickly free calcium enters or leaves the cell in the absence of an action potential, η
723 is the excitation rate for indicator bound calcium, r is the photon release rate for the excited
724 indicator bound calcium, and f and b are used to indicate the forward and backward rates
725 for chemical reactions respectively. The excitation rate defines the proportion of indicator
726 bound calcium that becomes excited at each time step. The photon release rate defines the
727 proportion of excited indicator bound calcium that releases a photon and returns to its relaxed
728 state at each time step. An action potential is modelled as a discontinuous increase in the free
729 calcium concentration to an appropriate value (Maravall et al., 2000).

730 Note that each of the three pairs of binding and unbinding terms in the first equation has a
731 corresponding pair in one of the subsequent three equations. Binding removes a free calcium
732 molecule and adds a bound calcium molecule, and unbinding does the opposite.

733 When using this model to simulate a fluorescence trace, the system of equations above are
734 first solved over a period of 25s without action potentials. This lets each of the five tracked
735 chemical concentrations reach their steady state. Then we use the given spike train and the
736 parameters to model the fluorescence trace.

737 Note that since the model has no spatial component, the mobile and immobile buffers
738 only differ in their binding and unbinding rates.

739 Photon release & capture

740 We used a simple model for the photon release. The number of photons released at each time
741 step was controlled by the number of excited indicator bound calcium molecules in the cell
742 and a parameter called the ‘release rate’. The release rate is an optimised free parameter of
743 the model.

744 As for the photon capture, in two-photon excitation microscopy the photons scattered
745 by the fluorescent indicator get scattered in all directions. Therefore the number of photons
746 detected is stochastic. This made the process for capturing photons the natural source of
747 noise in the system. The number of photons captured, and therefore the intensity of the

748 fluorescence, is modelled using a binomial distribution. The number of photons released was
749 used as the number of trials. The probability of success, or ‘capture rate’ was a free parameter
750 of the model that we optimised.

751 **2.2.2 Parameter optimisation**

752 The free parameters of the model are as follows:

753 **Calcium rate, β** Controls how quickly the concentration of free calcium will be driven to
754 the baseline concentration.

755 **Capture rate, p** The average proportion of photons captured by the photon detector.

756 **Excitation rate, η** The number of indicator bound calcium molecules that become excited
757 by photon bombardment at each time step.

758 **Release rate, r** The number of excited indicator bound calcium molecules that release a
759 photon at each time step.

760 To optimise the free parameters given a fluorescence trace, we applied the following proce-
761 dure:

- 762 1. The frequency power spectrum of the trace was measured.
- 763 2. The power spectrum was smoothed using a boxcar smoother (aka. sliding average, box
764 smoother).
- 765 3. The log of the smoothed power spectrum was measured.
- 766 4. Use the model to create a modelled fluorescence trace.
- 767 5. Apply steps 1, 2, and 3 to the modelled fluorescence trace.
- 768 6. Calculate the root mean squared difference between the log power of the actual fluo-
769 rescence trace, and the log power of the modelled fluorescence trace.
- 770 7. Calculate the root mean squared difference between the actual fluorescence trace and
771 the modelled fluorescence trace.
- 772 8. Use an optimisation algorithm to reapply this process, attempting to minimize the sum
773 of the two root mean squared differences at each iteration.

774 Using the root mean squared difference of the log power spectra as part of the objective
775 function forces the model to match the noise frequency of the actual fluorescence. Using
776 the root mean squared difference of the traces themselves forces the model to match the
777 amplitude of the fluorescence trace more accurately.

778 In order to minimise the objective function, a suite of meta-heuristic optimisation (aka.
779 black-box optimisation) algorithms were implemented on each of the traces in the dataset.
780 These methods were chosen because they don't require a gradient for the objective function
781 (gradient-free) and they are particularly useful for minimising stochastic objective functions
782 like the one we used here. The free parameters were optimised for each individual fluores-
783 cence trace. The most successful method for each trace was recorded. The method that was
784 most often successful was probabilistic descent, and the second most successful method was
785 generating set search. Both of these methods are examples of pattern search. These two
786 methods were the best optimisers on about 75% of the traces in the dataset.

787 Although this optimisation procedure minimises the value of the optimisation function,
788 the value never reaches zero for a number of reasons. Firstly, the fluorescence traces carry low
789 frequency fluctuations that cannot be captured by the model. Secondly, the model assumes
790 that the process of calcium binding to the fluorescent indicator is linear in time (see equation
791 1), but there are more complicated dynamics involved here. Fluorescent calcium indicators
792 are often built upon the calcium binding protein called 'calmodulin'. This protein has four
793 calcium binding sites. These sites are locally split into two pairs. Each pair has a different
794 affinity for calcium, and the affinity of the binding sites is affected by the occupancy of
795 the other binding sites (Kilhoffer et al., 1992). So the calcium to calcium indicator binding
796 process is non-linear, but the model does not take this into account.

797 **Fixed parameters**

798 As well as the optimised parameters mentioned in section 2.2.2, the model also has thirteen
799 fixed parameters. Please see table 2.1 for details of these parameters and their values. In
800 an application of the model, these parameters can be changed in order to model any given
801 fluorescent calcium indicator.

802 **2.2.3 Julia**

803 The programming language used to write and execute the model was 'Julia'. Julia is a dy-
804 namic programming language designed for technical computing. Julia was designed specif-
805 ically to provide a convenient high-level dynamic language similar to MATLAB, or Python,

Parameter	Description	Value	Source
baseline	The baseline concentration of free calcium within the cell soma	$4.5 \times 10^{-8} M$	(Maravall et al., 2000)
cell radius	The radius of the soma (assumed to be spherical)	$10^{-5} M$	(Fiala and Harris, 1999)
endogenous	The concentration of endogenous mobile buffer within the cell soma	$10^{-4} M$	(Faas et al., 2011)
frequency	The frequency at which the spike trains are sampled.	100Hz	
immobile	The concentration of endogenous immobile buffer within the cell soma	$7.87 \times 10^{-5} M$	(Bartol et al., 2015)
indicator	The concentration of fluorescent indicator within the cell soma	$10^{-4} M$	(Maravall et al., 2000)
k_{Bb}	The unbinding rate of the fluorescent calcium indicator	$160 s^{-1}$	(Bartol et al., 2015)
k_{Bf}	The binding rate of the fluorescent calcium indicator	$7.77 \times 10^8 s^{-1} M^{-1}$	(Bartol et al., 2015)
k_{Eb}	The unbinding rate of the endogenous mobile buffer	$10^4 s^{-1}$	(Bartol et al., 2015)
k_{ef}	The binding rate of the endogenous mobile buffer	$10^8 s^{-1} M^{-1}$	(Bartol et al., 2015)
k_{Imb}	The unbinding rate of the endogenous immobile buffer	$524 s^{-1}$	(Bartol et al., 2015)
k_{Imf}	The binding rate of the endogenous immobile buffer	$2.47 \times 10^8 s^{-1} M^{-1}$	(Bartol et al., 2015)
peak	The increase in free calcium concentration within the cell induced by an action potential	$2.9 \times 10^{-7} M$	(Maravall et al., 2000)

TABLE 2.1: **Fixed parameters** A table of the parameters fixed before optimising the model. The values of these parameters could be changed to model different fluorescent calcium indicators.

806 with improved performance. Julia’s type system and Julia’s direct interfaces with C and
807 Fortran allow this aim to be achieved (Bezanson et al., 2012). The Julia version of the
808 ‘Sundials’ package for ODE solving was used to solve the system of equations above. The
809 BlackBoxOptim.jl package for Julia was used to perform the optimisation.

810 **2.2.4 Spike inference**

811 We used spike inference algorithms to compare the quality of spike inference using the mod-
812 elled traces to the quality of spike inference using the observed traces. We also used the
813 spike inference algorithms to assess the effect of parameter perturbation on the spike infer-
814 ence. Three algorithms were used:

815 **Constrained non-negative deconvolution algorithm (aka Pnevmatikakis algorithm)** This
816 algorithm uses a constrained version of non-negative Weiner deconvolution to infer a
817 calcium signal and a ‘spiking activity signal’ from the fluorescence trace (Vogelstein
818 et al., 2010; Pnevmatikakis et al., 2016). The spiking activity signal is a non-negative
819 vector of real numbers reflecting the cell’s activity rather than an actual spike train. We
820 inferred a spike train by choosing an optimised threshold for the spiking activity sig-
821 nal. Whenever the spiking activity signal exceeded that threshold, an action potential
822 was inferred. The threshold was optimised by minimising the difference between the
823 number of spikes observed and the number of spikes predicted.

824 **ML-Spike algorithm** This algorithm uses a generalised version of the Viterbi algorithm to
825 return the spike train that maximises the likelihood of producing the given fluorescence
826 trace. The Viterbi algorithm is an algorithm for estimating the most likely sequence
827 of hidden states resulting in a sequence of observed states in a discrete-time finite-
828 state Markov process (Forney, 1973). In this case, each hidden state is defined by the
829 presence or absence of an action potential, and each observed state is the value of the
830 fluorescence trace at each time step. This algorithm assumes that the concentration of
831 calcium within the cell will decay to a drifting baseline, rather than a fixed baseline
832 (Deneux et al., 2016).

833 **Online Active Set method to Infer Spikes (OASIS)** This algorithm is once again based on
834 an auto-regressive model of the fluorescence trace, but can be generalised to any or-
835 der. The algorithm itself is a generalisation of the pool adjacent violators algorithm
836 (PAVA) that is used in isotonic regression. The OASIS algorithm works through the

837 fluorescence trace from beginning to end, this combined with the speed of the algo-
838 rithm means that it could be used for real-time online spike inference (Friedrich and
839 Paninski, 2016). Given a fluorescence trace, the algorithm will return the most likely
840 spike train and an inferred denoised fluorescence signal.

841 In order to quantify the quality of spike inference for a given algorithm, we ran that algorithm
842 on all of the fluorescence traces in dataset number eight of the spike finder datasets. Then we
843 measured some binary classification measures on the results. These measures included

- 844 • Accuracy
- 845 • True positive rate (aka recall, sensitivity, hit rate)
- 846 • True negative rate (aka specificity)
- 847 • Precision
- 848 • Negative predicted value
- 849 • False negative rate (aka miss rate)
- 850 • False positive rate (aka fall-out)
- 851 • False discovery rate
- 852 • False omission rate

853 In making these measurements, we allowed a tolerance of two subsequent time bins for spike
854 prediction. For example, the spike train data is a vector of 0s and 1s, with one element for
855 each time bin. A ‘0’ denotes inactivity, a ‘1’ denotes the presence of at least one action
856 potential. The inferred spike trains produced by the spike inference algorithms take the same
857 form. In our analysis, if a spike appeared in the inferred spike train up to two time frames
858 after a spike in the observed spike train, that spike was considered correctly inferred i.e. a true
859 positive. However, once a spike in the inferred spike train was matched to a spike from the
860 observed spike train, the inferred spike could not be matched to another observed spike. To
861 illustrate, if two spikes were inferred in the two time bins following an isolated observed
862 spike, the first inferred spike was considered correctly inferred, but the second inferred spike
863 was considered incorrectly inferred, i.e. a false positive.

864 The most useful measure was the true positive rate. This is because the spiking is sparse
865 and this measurement is sensitive to the number of spikes observed and inferred, but is not
866 affected by the true negative or false negative rates. After optimising the parameters for each

867 fluorescence trace we measured the spike inference quality for the observed fluorescence
868 traces, and compared this to the spike inference quality for the modelled traces.

869 When measuring the spike inference quality for higher frequency spike train (1 – 10Hz),
870 we used the accuracy as our binary classification measure. At these frequencies the variance
871 of the fluorescence trace was much higher than for sparser spiking regimes, therefore we
872 wanted to take into account the number of false negatives inferred by the algorithm.

873 **Comparing spike inference quality**

874 In order to compare spike inference quality we had to use methods for comparing samples.
875 When comparing the true positive rate distributions arising from two different datasets, or
876 two different algorithms on the same dataset, we compared the distributions using a paired
877 t-test.

878 **2.2.5 Perturbation analysis**

879 In order to measure the sensitivity of spike inference to changes in a given model parameter,
880 we perturbed the parameter and compared the quality of spike inference with the perturbed
881 parameters to the quality of spike inference with the experimental or optimised parameters.
882 In order to maximise the possibility of observing a difference due to the perturbation, we
883 perturbed the chosen parameter by a relatively large amount. For example, the experimen-
884 tal value for the molar concentration of the fluorescent indicator within the cell was 10^{-4}M
885 (Maravall et al., 2000). The perturbed values used for this parameter were 10^{-2}M , 10^{-3}M ,
886 10^{-5}M , and 10^{-6}M . The quality of the inference was compared by measuring the true posi-
887 tive rate for each perturbed value and using a t-test to compare the distributions of the results.

888 This analysis was performed firstly without any optimisation of the free parameters for
889 use with the perturbed parameters. Then the analysis was performed after the optimised
890 parameters for each perturbed value were calculated.

891 **2.2.6 Signal-to-noise ratio**

892 To assess the effect of perturbation on the modelled traces, we measured and compared the
893 signal to noise ratio (SNR) on each of the modelled traces. We calculated the SNR as the
894 peak change in fluorescence divided by the standard deviation of the baseline fluctuation of
895 the fluorescence trace (Tada et al., 2014). We measured these values by running the model
896 on a spike train consisting a long period of inactivity followed by one action potential. We
897 ran the model on this spike train one hundred times. We then measured the mean change

898 in fluorescence and standard deviation of baseline activity across the one hundred modelled
899 fluorescence traces, and calculated the SNR.

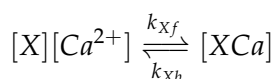
900 **2.2.7 Data sources**

901 All of the data used in this project was sourced from the ‘Spike Finder’ project (spikefinder.codeneuro.org).
902 The data consisted of a collection of datasets with simultaneously measured fluorescence
903 traces and action potentials (Berens et al., 2018).

904 **2.3 Results**

905 **2.3.1 A biophysical computational model can generate accurate fluorescence
906 traces from spike trains**

To study the relationship between action potential firing and calcium fluorescence, we built a computational model of calcium dynamics in a neuronal soma. The model consisted of four dynamic variables: the concentration of free calcium, two types of endogenous buffer, and the calcium-sensitive fluorescent indicator. Each of the buffers and the indicator could independently bind and unbind with calcium. These reactions were modelled as



907 where X is the buffer concentration and Ca^{2+} is the calcium concentration. Each species
908 could therefore exist in two states: either bound with calcium or unbound. To model the
909 imaging process, we also added a third, excited state to the indicator. When in the calcium-
910 bound state, the indicator could be converted to an excited state, corresponding to the absorp-
911 tion of a photon. The rate of this excitation process could be interpreted as the intensity of
912 the light illuminating the sample. Once excited, the species decayed back to the unexcited
913 state at a fixed rate, corresponding to the spontaneous emission of photons. The total emitted
914 fluorescence signal was interpreted as proportional to this de-excitation flux. To represent
915 experimental noise in the photon capture process, we drew a random number of captured
916 photons at each time step from a binomial distribution, parameterised by a number p that
917 corresponds to the mean fraction of released photons that are captured.

918 The model had 17 parameters in total describing the molecules’ concentrations and re-
919 action rates (Methods). We set 13 of these parameters to values from the literature. The
920 remaining 4 parameter values we fit to publicly-available data (Berens et al., 2018), briefly

explained as follows (see Methods for full details). Single neurons from acute rat cortical slices expressing GCaMP6f were imaged with two-photon microscopy while the membrane potentials of the somata of the same neurons were simultaneously recorded via whole-cell patch clamp electrophysiology. In this dataset, the electrical recordings give unambiguous information about neurons' spike times. To do the parameter fitting, we feed these spike trains as inputs to the computational model. After running, the model returns a simulated fluorescence trace. We aimed to find the model parameter values that give the best match between this simulated fluorescence trace and the real fluorescence time series recorded in the corresponding neuron. To do this we used a suite of optimisation procedures to jointly fit both the real neuron's fluorescence time series and power spectrum, which capture complementary information about the spikes-to-fluorescence mapping (Methods). We performed the fitting procedure independently for each of the 20 neurons in the spikefinder dataset (<http://spikefinder.org>). After fitting, the model produced realistic-looking fluorescence time series (Figure 2.1).

935 **2.3.2 Spike inference algorithms perform similarly on real data compared with
936 time series simulated from the model**

937 Researchers often pass the fluorescence time series through a spike inference tool before per-
938 forming further statistical analyses. These spike inference algorithms take the fluorescence
939 trace as input and attempt to estimate the neuronal spike train that triggered them (Vogelstein
940 et al., 2010; Pnevmatikakis et al., 2016; Friedrich and Paninski, 2016; Pnevmatikakis et al.,
941 2013; Pnevmatikakis et al., 2014; Deneux et al., 2016). Part of our motivation for building
942 this model was to allow us to ask the questionon-linearitiesproperties of the cell and the cal-
943 cium indicator affect the quality of spike inference? In order to trust the conclusions from
944 our model, we should first be confident that spike inference from our simulated fluorescence
945 traces is similar to that from the real data. To test this we passed each of the simulated fluores-
946 cence traces through three previously published spike inference algorithms, quantified their
947 performance against the ground-truth electrophysiology data, repeated the procedure for the
948 real calcium fluorescence time series, and compared the accuracy of the inference processes
949 in all cases. The *true positive rate*, also known as the *recall*, the *sensitivity*, or the *probabi-*
950 *lity of detection* of spike inference varied across the three inference algorithms we tried (p
951 value and statistical test here). The constrained non-negative matrix deconvolution algorithm
952 (Pnevmatikakis et al., 2016) (CNMD algorithm) correctly detected approximately 45% of the

953 true spikes, the OASIS algorithm (Friedrich and Paninski, 2016) correctly detected approx-
 954 imately 35% of the true spikes, and the ML spike algorithm (Deneux et al., 2016) correctly
 955 detected approximately 15% of the true spikes (see figure 2.2). Notably, for two of the three
 956 inference algorithms, the quality of inference was also fairly consistent for individual spike
 957 trains, not just the group means ($p > 0.05$, paired t-test). This demonstrates that the models
 958 were generating fluorescence time series that were similarly difficult to decode as the real
 959 data, in ways that were not specific to any one inference algorithm. This is evidence that the
 models captured real aspects of the spikes-to-fluorescence transform.

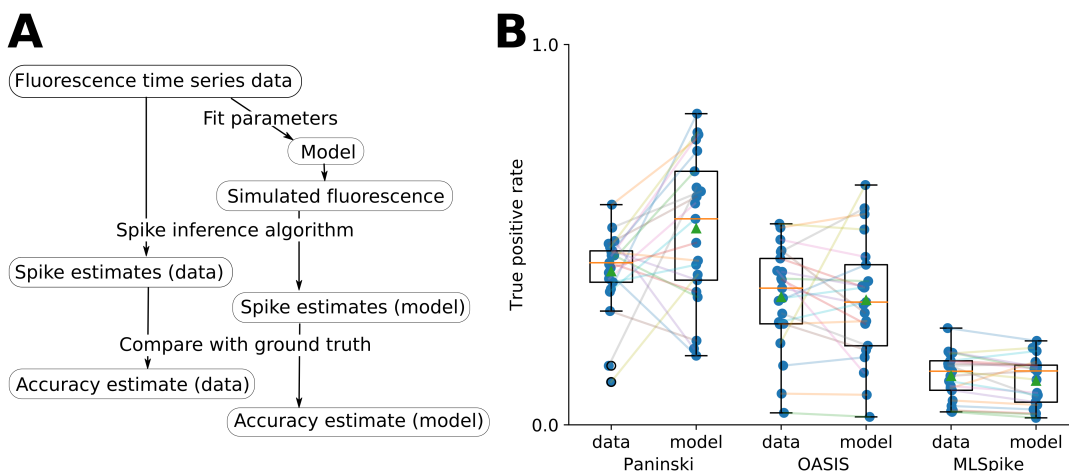


FIGURE 2.2:
 A: Workflow to compare spike inference for real versus simulated fluorescence data.
 B: True positive rates achieved by three different spike inference algorithms when applied to observed spike trains, and simulated spike trains. Data points overlaid as blue circles. The performance is similar from real and simulated data for each of the algorithms.

960

961 2.3.3 Relative effects of various buffers to the fluorescence signal

962 One of the benefits of computational models over laboratory experiments is that we can
 963 observe all the variables in the simulation to gain insight into the system's dynamics, which
 964 can be difficult to do in the lab. We plotted the concentrations of the various species over
 965 time for a version of the model fit to one data set, in response to the same train of spikes used
 966 for fitting (figure 2.3). Figure 2.3a shows the absolute values of the species concentrations,
 967 summed. Consistent with experimental estimates (Maravall et al., 2000), only a small fraction
 968 ($\sim 0.1\%$) of calcium is free and unbound to any buffer. Of the bound calcium, the vast
 969 majority, ($\sim 96\%$) is bound to the GCaMP indicator. The two types of endogenous buffer

970 are bound to the remaining calcium ($\sim 4\%$). An influx of calcium from a single spike adds
971 very little to the total calcium, in relative terms (red line in Figure 3a).

972 When calcium entered the model neuron it was rapidly buffered (Bartol et al., 2015).
973 However the relative fractions of which buffer molecules bound to the influxed calcium was
974 dynamic, and changed over time. Figure 2.3 (b-f) shows the time course of the various
975 species over time in response to a calcium influx event from a single action potential. Cru-
976 cially, the indicator $[BCa]$ competed with the endogenous buffers $[ImCa]$ and $[ECa]$ – all
977 three bind calcium on similar timescales. This implies that the timecourse and amplitude of
978 the $[BCa]$ variable will also depend on the binding rates and availabilities of the endogenous
979 buffers. For example if we decreased the concentration of an endogenous buffer, we might
980 expect both a faster rise time and greater peak amplitude of the $[BCa]$ signal in response to
981 a calcium influx event. The slowest component of the decay had a similar time constant for
982 $[BCa]$, $[ImCa]$ and $[ECa]$, which in turn matched the $[Ca]$ extrusion time constant in our
983 model ($\sim 6.29 \times 10^{-22} \text{Ms}^{-1}$). This implies that the buffers and the indicator had reached
984 a dynamic equilibrium and were jointly tracking the free calcium concentration as calcium
985 was slowly extruded from the cell.

986 Interestingly the excited bound calcium species ($[BCa^*]$) showed a qualitatively different
987 timecourse in response to a calcium influx event. This concentration is subject to the added
988 ‘excitation and release’ dynamic, where a certain proportion of the concentration absorbs the
989 energy from an incoming photon and goes into an ‘excited state’ at each time step. A certain
990 proportion of the concentration releases a photon and reverts to a ‘relaxed state’ at each
991 timestep also. This means that the excited bound calcium lags behind the bound calcium
992 trace. We could think of the excited bound calcium trace as a low pass filtered version of the
993 bound calcium trace.

994 **2.3.4 Spike inference accuracy is sensitive to indicator properties, and likely
995 varies within and between cells**

996 The above results imply that the fluorescence signal depends on the relative properties of
997 both GCaMP and the endogenous buffers. We next used the model to directly ask how
998 sensitive spike inference was to these components. We focused on three key parameters that
999 likely vary from cell to cell and experiment to experiment: GCaMP binding kinetics, GCaMP
1000 concentration, and endogenous buffer concentration.

1001 Several variants of GCaMP itself have been made that differ in calcium binding kinetics,
1002 baseline fluorescence, fluorescence efficiency, and other factors. For example, GCaMP6f has

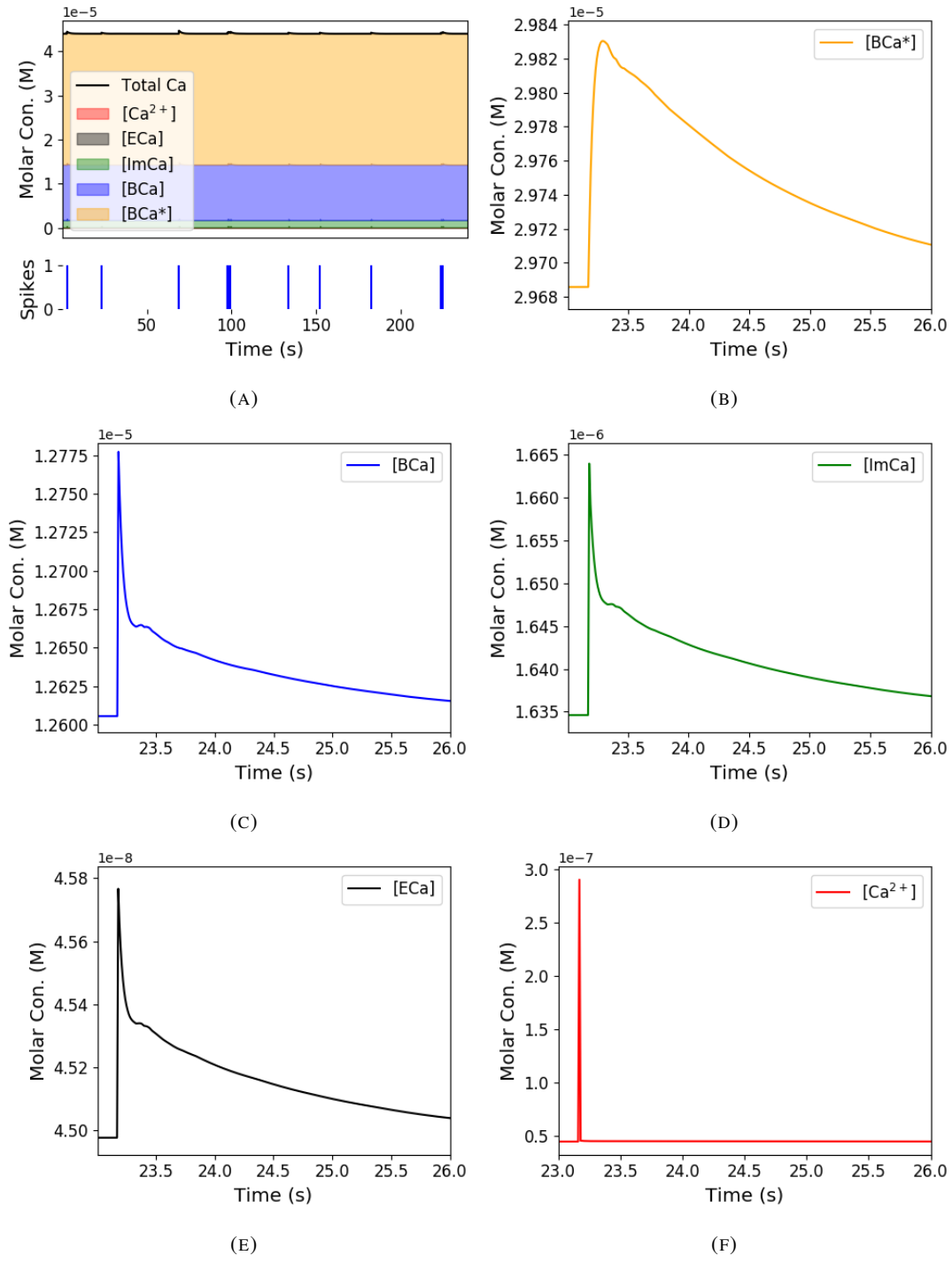


FIGURE 2.3: Calcium Buffering Dynamics (a) The proportions of bound and free calcium concentrations within a cell, with the associated spike train. (b)-(f) The dynamics of the concentration of (b) excited indicator bound calcium, (c) indicator bound calcium, (d) immobile endogenous buffer bound calcium, (e) mobile endogenous buffer bound calcium, and (f) free calcium in response to an action potential at ~ 23.2 s.

1003 a decay time constant of \sim 1s, while GCaMP6s has a decay time constant of \sim 2s (Chen
1004 et al., 2013). Here we asked how these differences in binding kinetics affect spike inference.
1005 We jointly varied the calcium binding and unbinding rates of the indicator by the same factor
1006 over a range from 100-fold slower to 100-fold faster from the fitted values, and simulated the
1007 fluorescence response for each of the parameter settings in response to the same spike trains
1008 as before (figure 2.4). Notably this manipulation does not affect the indicators affinity, and
1009 therefore would not affect steady-state responses to prolonged changes in calcium. Instead
1010 it is likely to affect its sensitivity to the spike train dynamics. We computed two summary
1011 measures from the simulated fluorescence traces: the signal-to-noise ratio for a single spike
1012 (Methods, section 2.2.6), and the accuracy of spike inference for each of the spike trains. We
1013 observed a reduction in the signal-to-noise ratio and the spike inference quality when we set
1014 the binding and unbinding rates were set to one hundredth of their fitted values, and to one
1015 tenth of their fitted values. When we increased the value of both binding rates, we observed
1016 no change in these measurements. The reduction in both rates lead to smaller increases in
1017 fluorescence in response to an action potential and a longer decay time (figure 2.4a), this
1018 caused the reduction in signal-to-noise ratio. As both rates were increased, the change in
1019 $\Delta F/F_0$ in response to an action potential increased and the decay time decreased slightly,
1020 but the fluorescence trace created by these values was very similar to the trace created by the
1021 fitted values.

1022 Second, the overall concentrations of GCaMP often varies from cell to cell. For exam-
1023 ple different cells, even of the same type in the same tissue, can express different levels of
1024 GCaMP, due to proximity to the infection site, or the cell becoming ‘nuclear-filled’ (Tian et
1025 al., 2009; Chen et al., 2013). Also, GCaMP is often used for longitudinal experiments where
1026 the same cells are re-imaged across multiple days or weeks. However since GCaMP expres-
1027 sion typically ramps up over time (Chen et al., 2013), the accuracy of spike inference may
1028 differ across multiple longitudinal recordings in the same cell. We addressed this by varying
1029 the concentration of calcium indicator in the model, simulating spike trains and measuring
1030 signal-to-noise ratio and spike inference accuracy on the resulting fluorescence traces. Both
1031 increasing and decreasing the concentration of the indicator had effects on the fluorescence
1032 trace, signal-to-noise ratio, and spike inference. The signal-to-noise ratio and spike inference
1033 quality decreased with decreased indicator concentration, and both showed a decrease when
1034 the indicator concentration was increased to 100 times its fitted value (figure 2.5). The signal-
1035 to-noise ratio showed an increase when the indicator concentration was increased to 10 times
1036 its fitted value, but there was no corresponding change in the spike inference quality. The

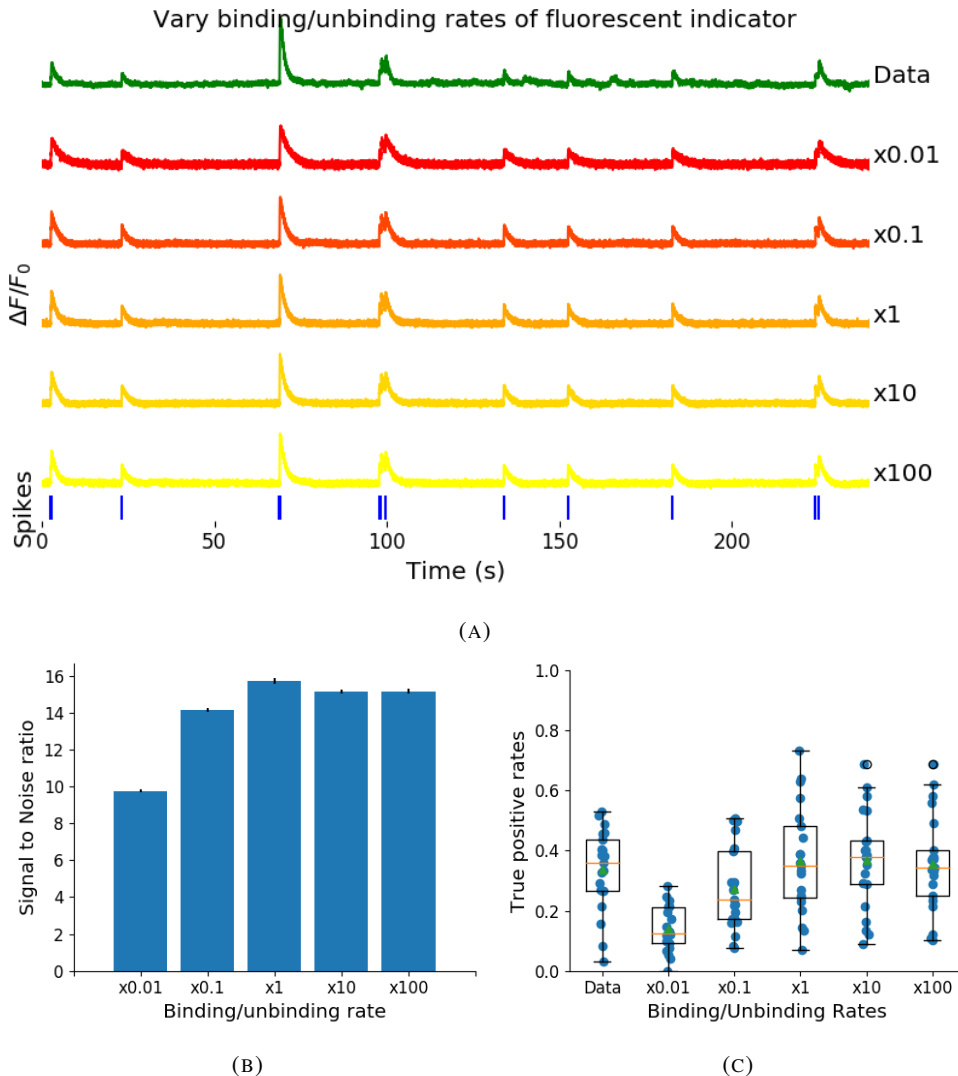


FIGURE 2.4: (a) An example trace for each of the five pairs of values used for the binding and unbinding rates of the fluorescent calcium indicator. (b) The signal-to-noise ratio of the modelled fluorescence traces using each of the four perturbed value pairs, and the experimental value. The SNRs for the value pairs perturbed downward are lower than that for the unperturbed value pair or the higher value pairs. (c) The true-positive rates of the deconvolution algorithm's predictions when inferring from the observed data, and inferring from modelled traces using the perturbed and experimental values.

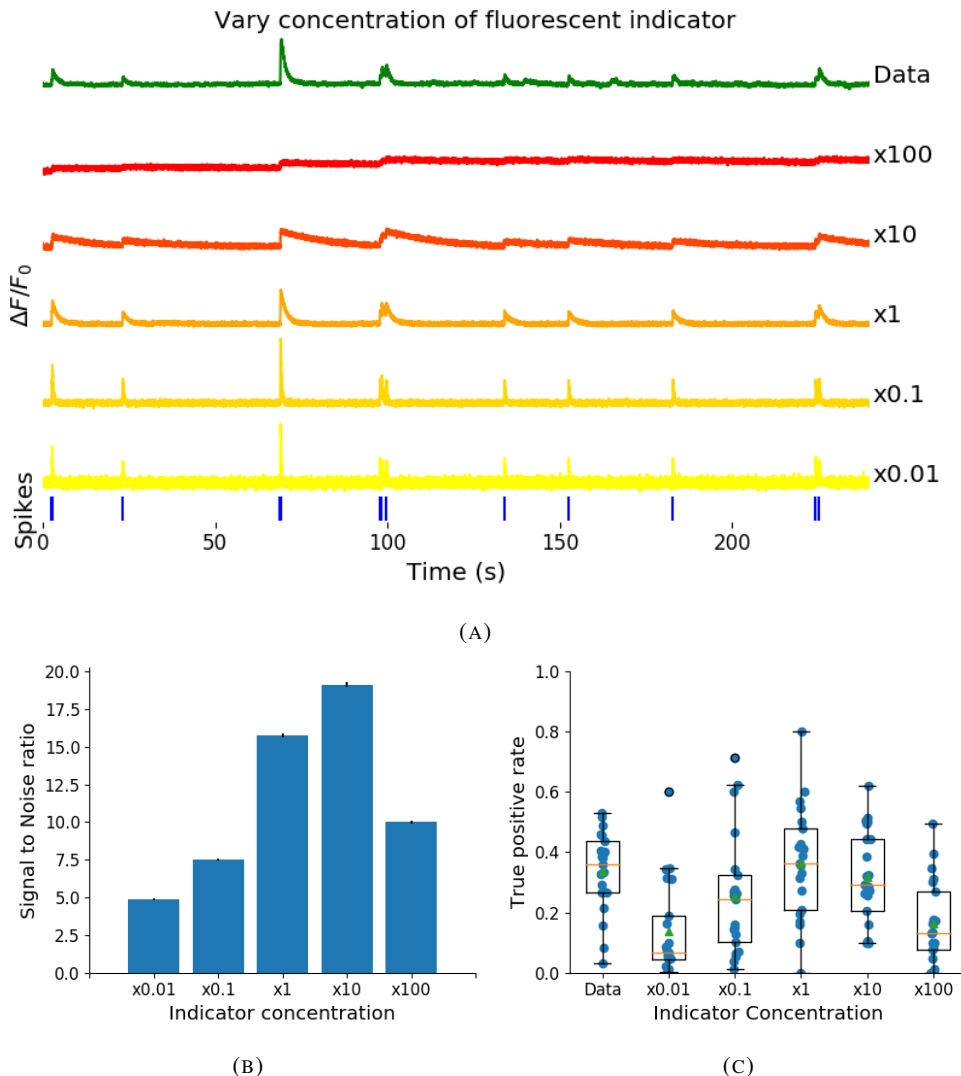


FIGURE 2.5: (a) An example trace for each of the five perturbed values for the concentration of fluorescent calcium indicator. The top two traces are produced by the lower perturbed values, the middle trace is produced by the experimental value, and the lowest two traces are produced when using the higher perturbed values. (b) The signal-to-noise ratio of the modelled fluorescence traces using each of the four perturbed values, and the experimental value. Extreme perturbations of the concentration either above or below the experimental level lowered the SNR. (c) The true-positive rates of the deconvolution algorithm's predictions when inferring from the observed data, and inferring from modelled traces using the perturbed and experimental values. We found that the algorithms performs equally badly on the two most extreme values, and performs equally well on the experimental value, and the next higher perturbed value.

1037 decrease in indicator concentration caused a reduction in the increase in $\Delta F / F_0$ in response
1038 to an action potential, and an increase in the decay time of this increase (figure 2.5a). The
1039 increase in indicator concentration had the opposite effect, it caused an increase in the change
1040 in $\Delta F / F_0$ in response to an action potential, and a decrease in the decay time.

1041 Third, the concentration and types of endogenous calcium buffers also vary from neuron
1042 to neuron, both within and between cell types (Bartol et al., 2015; Maravall et al., 2000;
1043 Neher and Augustine, 1992). Since the calcium buffer capacity of neurons is high, around
1044 50-70 (Lee et al., 2000) in excitatory hippocampal pyramidal cells, around 100-250 (Lee et
1045 al., 2000) in inhibitory hippocampal pyramidal cells, and 900-200 in Purkinje cells (depend-
1046 ing on the age of the subject), these endogenous buffers compete with GCaMP for binding
1047 to calcium, and variations in endogenous buffer concentration may affect GCaMP signal and
1048 therefore spike inference. To address this we varied the concentration of the endogenous
1049 buffer in the model neuron over five orders of magnitude from 0.8 to 8000 μM , simulated
1050 calcium fluorescence traces in response to the same set of spike trains, and performed spike
1051 inference on the resulting fluorescence time series. Increasing the endogenous buffer con-
1052 centration had a substantial effect on the GCaMP fluorescence signal, both decreasing its
1053 amplitude and slowing its kinetics (figure 2.6(a)). This corresponded with a decrease in both
1054 single-spike signal-to-noise ratio (figure 2.6(b)) and spike inference accuracy (figure 2.6(c)).
1055 In contrast, decreasing endogenous buffer capacity from the fitted value had little effect on
1056 either the GCaMP signal or spike inference (figure 2.6).

1057 **2.3.5 Single spike inference accuracy drops for high firing rates, but firing rate
1058 itself can be estimated from mean fluorescence amplitude**

1059 The fluorescence signal recorded from neurons using calcium indicators is typically much
1060 slower than changes in membrane potential for two reasons: first, because the calcium and
1061 the indicator have slow binding and unbinding kinetics, the signal is a low-pass filtered ver-
1062 sion of the membrane potential. Second, neuronal two-photon imaging experiments are often
1063 performed in scanning mode, which limits their frame rate to $\sim 10\text{Hz}$ or slower. This im-
1064 plies that multiple spike events that occur close in time might be difficult to resolve from a
1065 calcium indicator time series. Many cells, especially several types of inhibitory interneurons,
1066 fire tonically at rates higher than 10Hz. We used the model to test whether spike inference
1067 accuracy depended on the neuron's firing frequency by driving the cell with spike trains sam-
1068 pled from a Poisson processes of varying frequency. We simulated a variable firing rate using
1069 an Ornstein-Uhlenbeck process, and simulated the spike trains using a Poisson distribution

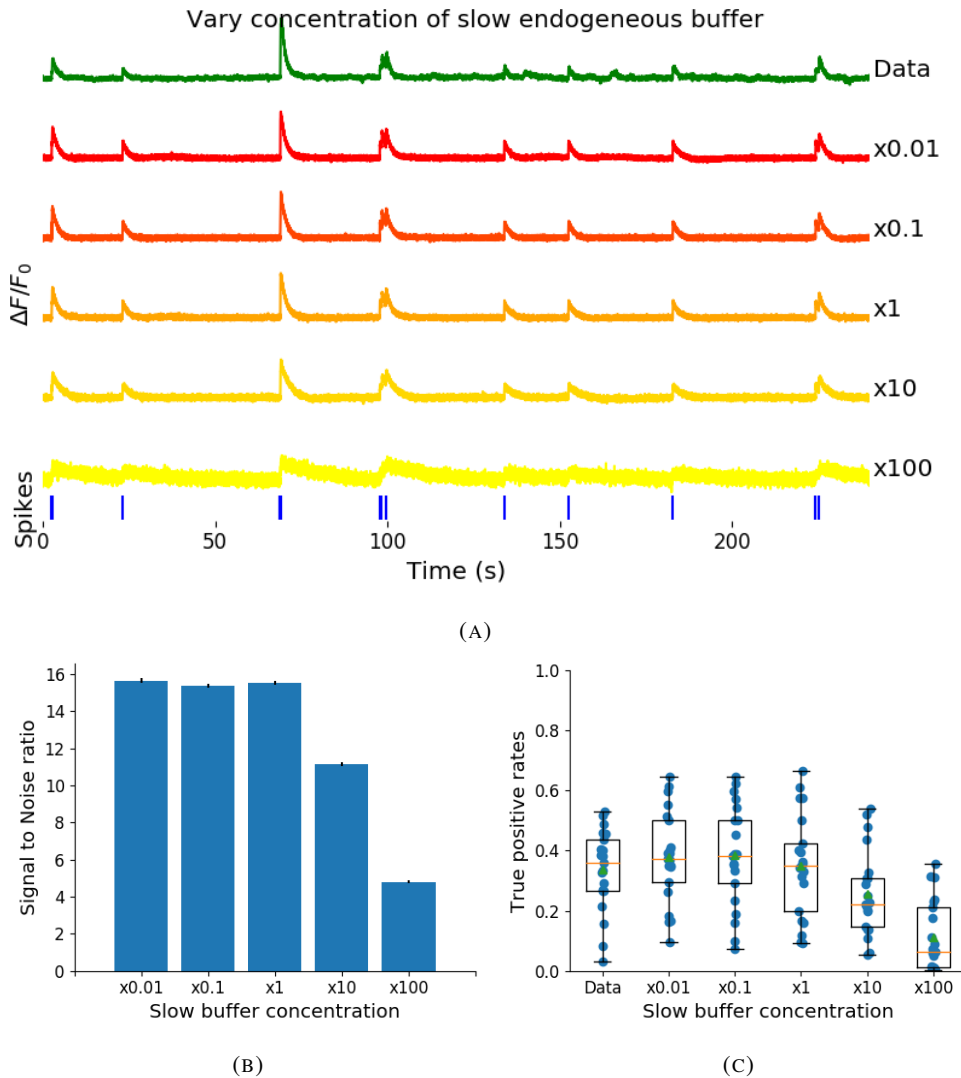


FIGURE 2.6: (a) An example trace for each of the five perturbed values for the concentration of immobile endogenous buffer. (b) The signal-to-noise ratio of the modelled fluorescence traces using each of the four perturbed values, and the experimental value. The lower values for the immobile buffer produce the same SNR as the experimental value. But the higher perturbed values produce fluorescence traces with a lower SNR. (c) The true-positive rates of the deconvolution algorithm’s predictions when inferring from the observed data, and inferring from modelled traces using the perturbed and experimental values.

with its rate taken from this process. Because of the high frequency firing rate of these spike trains, we used the accuracy as the measure of spike inference quality. We simulated 30 spike trains at average firing rate of 1, 5, and 10Hz, and measured the spike inference quality of all these traces. Spike inference accuracy decreased with increasing firing rate, for up to 10Hz Poisson spike trains (figure 2.8(left)). Although the accuracy remained above 90% for each of the three frequencies. We also plotted the average $\Delta F/F_0$ as a function of stimulation firing rate. We found that it increased monotonically as a function of firing rate (figure 2.8(right)).

We expected lower spike inference quality as the average spiking frequency increased. Since the fluorescence trace, in some sense, is a low pass filtered version of the spike train, a tightly packed groups of spikes will be more difficult to infer than isolated spikes. However, the increasing amplitude of the fluorescence trace with increasing frequency suggests that some spike inference algorithm could be developed based on this amplitude.

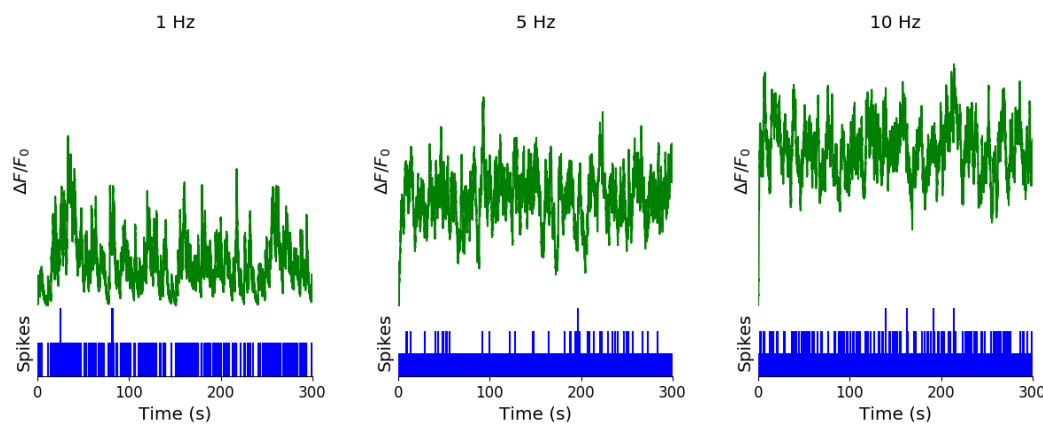


FIGURE 2.7: Simulating fluorescence traces at different firing rates Example modelled traces created using simulated spike trains with a mean firing rate of 1Hz (left column), 5Hz (middle column), and 10Hz (right column). Note the difference in amplitude with different mean firing rates.

2.4 Discussion

We designed a biophysical model for the changes in free calcium and bound calcium concentrations within a cell soma with a fluorescent calcium indicator. We used this model to model the fluorescence trace resulting from a spike train in this cell. We fit the free parameters of the model by matching the power spectrum and amplitude of fluorescence traces with simultaneously measured spike trains. We inferred spikes from real fluorescence traces and modelled fluorescence traces, and measured the quality of the spike inference in both cases.

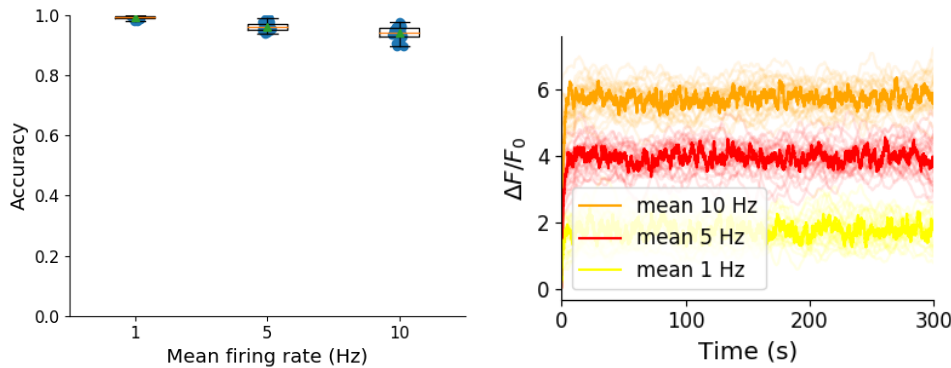


FIGURE 2.8: **Inference quality and $\Delta F/F_0$ vs Firing rate** (left) The spike inference accuracy when applied to 30 traces created using simulated spike trains with mean firing rates of 1, 5, and 10 Hz. (right) The mean $\Delta F/F_0$ across those 30 traces for each frequency.

1090 We found that the spike inference quality was similar in both cases. We perturbed the concentration of the calcium buffers in the model, and the binding/unbinding rates of those buffers
 1091 in the model, and measured the effect on the signal-to-noise ratio (SNR) of the modelled
 1092 fluorescence traces and the spike inference quality.
 1093

1094 For the fluorescent calcium indicator, we found that any large perturbation away from
 1095 the taken from the literature led to a reduction in SNR, and spike inference quality. For the
 1096 binding/unbinding rates, we kept the ratio of these rates constant, but altered their values in
 1097 parallel. The lower values caused a reduction in SNR, and a reduction in spike inference
 1098 quality. For the endogenous buffer concentration, an increase above the experimental value
 1099 caused a reduction in SNR and spike inference quality.

1100 Although the model produced visually similar time series to the real data, there were a
 1101 few aspects it did not capture. First, the real data featured some low-frequency components
 1102 that did not appear related to the spike events. These were not captured by the models we
 1103 used in this study, but could be added in future by adding a suitable low-frequency term to the
 1104 resulting time series. Second, the real data seemed to have some non-linearities not captured
 1105 in the model, for example the response to two nearby spikes was greater than expected from
 1106 the linear sum of two single spikes. This may be due to the co-operative binding of calmod-
 1107 ulin to calcium, which gives calmodulin a supra-linear sensitivity to calcium concentration
 1108 (Faas et al., 2011). The non-linear dynamics of this binding have been included in a recently
 1109 developed spike inference model (Greenberg et al., 2018). Our model, in contrast, behaved
 1110 much more linearly but could be extended in future to include such non-linearities. Third,
 1111 in the real data the fluorescence peak amplitude seemed to vary from spike to spike, even
 1112 for well-isolated spike events. Recent research has shown that calcium influx due to a single

action potential was quite variable in pyramidal cells, and that this variability had a effect on spike inference (Éltes et al., 2019). However in our model we assumed each spike lead to the same fixed-amplitude injection of calcium to the cell, leading to much greater regularity in fluorescence peak amplitudes. This variability could be added in future versions of the model by making the injected calcium peak a random variable. Fourth, we modelled the soma as a single compartment, but in reality there is likely a non-uniform spatial profile of calcium concentration. This may matter because some endogenous buffers might access calcium right as it influxes from the extracellular space, whereas the majority of the fluorescence signal is more likely coming from the bulk of the cytoplasm. Future models could attempt to model these spatial dependencies to assess whether they affect the overall spike inference procedure.

As well as the optimised parameters, the model has 14 fixed parameters than can be changed to simulate different types of calcium indicators. This model could be used to test the theoretical performance of proposed new types of calcium indicator. The model could also be used by developers of spike inference algorithms to test the effects of changing calcium indicator parameters on spike inference, or to test the affects of changing spiking characteristics on spike inference. For example, high firing rate vs low firing rate, or bursting vs no bursting. Given the increasing amplitude of the fluorescence trace with increasing mean firing rate, it would be possible to build a spike inference algorithm on this principle at least in part.

Our model has already been used as a tool by our colleagues, for simulating fluorescence traces in response to cells that can fire with a continuous rate between 10 and 20Hz, but do not always do so. Our colleagues found that a combination of the amplitude and the variance of the simulated fluorescence trace was the best indicator of firing rate. For example, when a cell was not firing, the amplitude and variance of the fluorescence trace was relatively low. When the cell fired with a low firing rate $\sim 1\text{Hz}$, the mean amplitude was still low but the variance of the fluorescence trace was high, and for high firing rate $\sim 10 - 20\text{Hz}$, the fluorescence amplitude was high, and the variance was low. In this way, our model may be useful for investigating firing rates underlying real fluorescence traces in response to cells which can fire in these rage ranges.

A recent paper by Greenberg et al (2018) described a biophysical model for spike train inference called the ‘Sequential binding model’. Their model for spike inference was similar to our model for fluorescence traces in that their model included parameters for two types of endogenous buffer. But this model also included dynamics for calcium binding to and unbinding from these endogenous buffers. Furthermore, this model included dynamics

1147 for calcium binding to and unbinding from the four binding sites present on a GCaMPs6
1148 molecule. In the accuracy measurements specified in that paper, this model performed better
1149 than the MLspike algorithm, which is also partially a biophysically model, and it performed
1150 better than the constrained non-negative deconvolution algorithm. The sequential binding
1151 model also has biophysically interpretable parameters, and its fitted parameters for quantities
1152 such as buffering capacity and calcium influx upon action potential firing fall in line with
1153 experimental values (Greenberg et al., 2018). Biophysical models like this appear to be the
1154 way forward for spike inference algorithms, and would make a good complimentary tool to
1155 our fluorescence model.

1156 **Chapter 3**

1157 **Functional networks expand across
1158 anatomical boundaries as correlation
1159 time-scale increases**

1160 *Abstract*

1161 Decades of research has established that correlated spiking plays a crucial role in represent-
1162 ing sensory information. One drawback associated with the recent improvement in recording
1163 technology and consequent large datasets is the difficulty in analysing higher order correla-
1164 tions in large neuronal ensembles. One benefit of these datasets that has not yet been explored
1165 is the opportunity to compare correlations within anatomical regions to correlations across
1166 anatomical regions. In this work, we measured correlations between neurons residing in
1167 nine different brains regions in three awake and behaving mice. Using the these correlation
1168 measurements, we created weighted undirected graph networks and applied network science
1169 methods to detect functional communities in our neural ensembles. We compared these func-
1170 tional communities to their anatomical distribution. We repeated the analysis, using different
1171 timescales for our correlation measurements, and found that functional communities were
1172 more likely to be dominated by neurons from a single brain region at shorter timescales
1173 (< 100ms).

1174 3.1 Introduction

1175 Decades of research has established that correlations play a crucial role in representing sen-
1176 sory information. For example, the onset of visual attention has been shown to have a greater
1177 affect on the correlations in the macaque V4 region than on the firing rates in that region
1178 (Cohen and Maunsell, 2009). Recent findings show that spontaneous behaviours explain cor-
1179 relations in parts of the brain not associated with motor control (Stringer et al., 2019), that
1180 satiety state appears to have a brain wide representation (Allen et al., 2019), and that subject
1181 exploratory and non-exploratory states are represented in the amygdala (Gründemann et al.,
1182 2019). So, behavioural states are likely represented across many regions of the brain, not just
1183 motor related areas. In order to understand the brain, we must understand the interactions
1184 between neurons and regions.

1185 Because of limitations in recording technology almost all research has explored corre-
1186 lations between neurons within a given brain region, or within only two regions at most
1187 (Wierzynski et al., 2009; Patterson et al., 2014; Girard, Hupé, and Bullier, 2001). Rela-
1188 tively little is known about correlations between neurons in many different brain regions.
1189 However, the recent development of ‘Neuropixels’ probes (Jun et al., 2017) has allowed
1190 extracellular voltage measurements to be collected from multiple brain regions simultane-
1191 ously routinely, and in much larger numbers than traditional methods. In this project we
1192 used a publicly-available Neuropixels dataset to analyse correlations between different brain
1193 regions (Stringer et al., 2019).

1194 A drawback associated with the improvement in recording technology is an increase in
1195 the difficulty in analysing these data. For example, analysing the i th order interactions of
1196 N neurons generally requires estimation of N^i parameters. A number that becomes astro-
1197 nomical for large N . New methods are required for analysing these new large datasets. We
1198 attempted to address this requirement in this piece of research by applying a cutting-edge
1199 network science community detection method to neural data.

1200 Another unexplored area of research is the changes in cell interactions at different timescales.
1201 Studies have shown different timescales for fluctuations in spiking activity (Murray et al.,
1202 2014), and different time scales for event representation (Baldassano et al., 2017) across dif-
1203 ferent brain regions. Still most studies focus on quantifying interactions at a given timescale.
1204 But neurons may interact differently, or may interact with different neurons at different
1205 timescales. Here we explore correlated communities of neurons at different timescales.

1206 In this work, we measured correlations between binned spike counts from neurons from

1207 nine different regions of the mouse brain. These measurements induced a weighted undi-
1208 rected graph or network where each neuron is represented by a node, and the strength of
1209 the connection between these nodes/neurons is the strength of the correlation between their
1210 spike counts. We then applied newly invented network methods (Humphries et al., 2019)
1211 to this network to find any community structure, and place the neurons in these correlation
1212 based communities. Finally, we compared these functional communities to the anatomical
1213 membership of the neurons.

1214 To investigate the functional communities and their relationship with anatomy at different
1215 time scales, we repeated these analyses using different length bin widths when binning spike
1216 times.

1217 To find and analyse functional networks while controlling for the subject’s behaviour, we
1218 conditioned the binned spike counts on data from a video of the subject’s face, and repeated
1219 our analysis for spike count correlations (or noise correlations) and signal correlations.

1220 **3.2 Data**

1221 The data that we used in this project were collected by Nick Steinmetz and his lab members
1222 (Stringer et al., 2019).

1223 **3.2.1 Brain regions**

1224 Neuropixels probes were used to collect extracellular recordings (Jun et al., 2017) from three
1225 different mice. The mice were awake, headfixed, and engaging in spontaneous behaviour.
1226 The mice were of different sexes and different ages. One mouse was ‘wild-type’, the others
1227 were mutants. Details as follows:

- 1228 1. male, wild type, P73.
1229 2. female, TetO-GCaMP6s, Camk2a-tTa, P113
1230 3. male, Ai32, Pvalb-Cre, P99

1231 Eight probes were used to collect readings from 2296, 2668, and 1462 cells respectively.
1232 Data were collected from nine brain regions in each mouse:

- 1233 • Caudate Putamen (CP)
1234 • Frontal Motor Cortex (Frmocxtx)
1235 • Hippocampal formation (Hpf)

- 1236 • Lateral Septum (Ls)
- 1237 • Midbrain (Mb)
- 1238 • Superior Colliculus (Sc)
- 1239 • Somatomotor cortex (Sommotcx)
- 1240 • Thalamus (Th)
- 1241 • Primary visual cortex (V1)

1242 Readings were continuous and lasted for about 1 hour (Stringer et al., 2019). Locations of
 1243 each of the probes can be seen in figure 3.1.

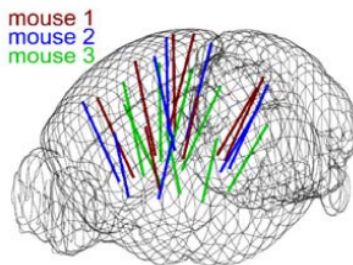


FIGURE 3.1: Probe Locations: The locations of the probes in each of the three mouse brains (Stringer et al., 2019).

1244 3.2.2 Video recordings

1245 Video recordings of the mouse's face were taken during the spontaneous behaviour. We had
 1246 access to the top 500 principle components and top 500 eigenvectors of the processed videos.
 1247 The frequency of recording was slightly less than 40Hz. Each frame contained 327×561
 1248 pixels. These principal components were used as behavioural data. We controlled for these
 1249 components when taking measurements conditioned on behaviour.

1250 3.3 Methods

1251 3.3.1 Binning data

1252 We transformed the spike timing data into binned spike count data by dividing the exper-
 1253 imental period into time bins and counting the spikes fired by each cell within the time period
 1254 covered by each of those bins. The data were divided into time bins of various widths ranging
 1255 from 0.01s to 4s.

If the total length of the recording period was not an integer multiple of the time bin width, we cut off the remaining time at the end of the recording period. This period was at most 3.99s. This is far less than the total recording time of around 1 hour. So, this detail would not affect our results.

3.3.2 Correlation coefficients

We calculated Pearson's correlation coefficient for pairs of spike counts from pairs of neurons. For jointly distributed random variables X and Y , Pearson's correlation coefficient is defined as:

$$\rho_{XY} = \frac{\text{cov}(X, Y)}{\sigma_X \sigma_Y} \quad (3.1)$$

$$= \frac{E[(X - \mu_X)(Y - \mu_Y)]}{\sigma_X \sigma_Y} \quad (3.2)$$

where E denotes the expected value, μ denotes the mean, and σ denotes the standard deviation. The correlation coefficient is a normalised measure of the covariance. It can take values between 1 (completely correlated) and -1 (completely anti-correlated). Two independent variables will have a correlation coefficient of 0. But, having 0 correlation does not imply independence.

If we do not know the means and standard deviations required for equation 3.1, but we have samples from X and Y , Pearson's sample correlation coefficient is defined as:

$$r_{XY} = \frac{\sum_{i=1}^n (x_i - \bar{x})(y_i - \bar{y})}{\sqrt{\sum_{i=1}^n (x_i - \bar{x})^2} \sqrt{\sum_{i=1}^n (y_i - \bar{y})^2}} \quad (3.3)$$

where $\{(x_i, y_i)\}$ for $i \in \{1, \dots, n\}$ are the paired samples from X and Y , and $\bar{x} = \frac{1}{n} \sum_{i=1}^n x_i$, and $\bar{y} = \frac{1}{n} \sum_{i=1}^n y_i$ are the sample means.

In practice we used the python function `scipy.stats.pearsonr` to calculate the correlation coefficients.

1270 Total correlations, r_{SC}

The total correlation (r_{SC}) of two cells is the correlation between the spike counts of those cells in response to a given stimulus condition.

1273 **Shuffled total correlations**

1274 We measured the shuffled total correlations between two neurons by randomly permuting one
 1275 of the neuron's spike counts and measuring the total correlations. These shuffled correlations
 1276 were useful when measuring the effect of time bin width on correlations, and when decid-
 1277 ing which correlations should be preserved when creating correlation networks (see section
 1278 [3.3.5](#)).

1279 **Separating Correlations & Anti-correlations**

1280 In order to compare the effect of bin width on measures of negative r_{SC} (anti-correlation) and
 1281 positive r_{SC} separately, we had to separate correlated and anti-correlated pairs. To do this, we
 1282 simply measured the mean r_{SC} , taking the mean across all the bin widths. If this quantity was
 1283 positive or zero we regarded the pair as positively correlated. If this quantity was negative
 1284 we regarded the pair as anti-correlated.

1285 **3.3.3 Conditioning on behavioural data**

Our behavioural data consisted of the top 500 principal components (PCs) of a processed video recording of the mouse's face (see section [3.2.2](#)). Denoting the spike count of a given cell by X , and the PCs by Z_1, \dots, Z_{500} , we wanted to model X as a function of Z_1, \dots, Z_{500} in order to estimate

$$E[X|Z_1, \dots, Z_{500}] = \int_{x \in X} x P(X = x|Z_1, \dots, Z_{500}) dx \quad (3.4)$$

$$= \int_{x \in X} x \frac{P(X = x, Z_1, \dots, Z_{500})}{P(Z_1, \dots, Z_{500})} dx \quad (3.5)$$

1286 Given the 500 components, a naïve estimation of $P(Z_1, \dots, Z_{500})$ or $P(X, Z_1, \dots, Z_{500})$ by
 1287 histogramming was impossible. Therefore we modelled X as a linear combination of the
 1288 PCs.

1289 **Linear regression**

1290 We modelled the spike count of a given cell, X , as a linear combination of the PCs of the
 1291 video of the mouse's face, $\mathbf{Z} = Z_1, \dots, Z_{500}$. We tried three different types of regularization

1292 • *L1* or 'Lasso'

1293 • *L2* or 'Ridge regression'

- 1294 • ‘Elastic net’ regularisation (a linear combination of both $L1$ and $L2$ regularisation
 1295 penalties)

1296 The elastic net regularisation performed the best, so we stuck with that.

1297 **Elastic net regularisation**

Suppose we wish to model n observations of a random variable X , $\mathbf{x} = (x_1, \dots, x_n)$ using n instances of m predictors $\mathbf{Z} = (Z_1, \dots, Z_m)$. The naïve elastic net criterion is

$$L(\lambda_1, \lambda_2, \boldsymbol{\beta}) = |\mathbf{x} - \mathbf{Z}\boldsymbol{\beta}|^2 + \lambda_2|\boldsymbol{\beta}|_2 + \lambda_1|\boldsymbol{\beta}|_1 \quad (3.6)$$

where

$$|\boldsymbol{\beta}|_2 = \sum_{j=1}^m \beta_j^2 \quad (3.7)$$

$$|\boldsymbol{\beta}|_1 = \sum_{j=1}^m |\beta_j| \quad (3.8)$$

The naïve elastic net estimator $\hat{\boldsymbol{\beta}}$ is the minimiser of the system of equations 3.6 (Zou and Hastie, 2005)

$$\hat{\boldsymbol{\beta}} = \arg \min_{\boldsymbol{\beta}} L(\lambda_1, \lambda_2, \boldsymbol{\beta}) \quad (3.9)$$

1298 We implemented the model using the `ElasticNetCV` method of Python’s
 1299 `sklearn.linear_models` package.

1300 As well as using the PCs, we also tried fitting the models using the raw video data recon-
 1301 structed from the PCs and eigenvectors. These models performed worse than those using the
 1302 PCs. We expected this because each representation contains the same amount of information,
 1303 but the raw video representation spreads this information across many more components.
 1304 This requires more parameter fitting, but given the same information.

1305 **Conditional covariance**

We calculated the expected value of the conditional covariance using the law of total covariance.

$$\text{cov}(X, Y) = E[\text{cov}(X, Y|Z)] + \text{cov}(E[X|Z], E[Y|Z]) \quad (3.10)$$

1306 where these expected values are calculated with respect to the distribution of Z as a random
 1307 variable.

1308 The law of total covariance breaks the covariance into two components. The first com-
 1309 ponent $E[\text{cov}(X, Y|Z)]$ is the expected value, under the distribution of Z , of the conditional
 1310 covariance $\text{cov}(X, Y|Z)$. This covariance could be interpreted as the unnormalised version
 1311 of what Cohen et al. (2011) call the spike count correlation (Cohen and Kohn, 2011), aka.
 1312 the noise correlation. In particular, this is the covariance of the spike counts in response to
 1313 repeated presentation of identical stimuli.

1314 The second component is analogous to what Cohn et al. (2011) call the *signal correlation*
 1315 (Cohen and Kohn, 2011). In particular, $\text{cov}(E[X|Z], E[Y|Z])$ is the covariance between
 1316 spike counts in response to different stimuli.

Using our linear model, we calculated $E[X|Z_1, \dots, Z_{500}]$ for each cell X . Then we pro-
 ceeded to calculate

$$E[\text{cov}(X, Y|Z_1, \dots, Z_{500})] = \text{cov}(X, Y) - \quad (3.11)$$

$$\text{cov}(E[X|Z_1, \dots, Z_{500}], E[Y|Z_1, \dots, Z_{500}]) \quad (3.12)$$

1317 **Measures of conditional correlation**

As a measure of expected correlation, we measured the ‘event conditional correlation’ (Maugis,
 2014)

$$\rho_{XY|Z} = \frac{E[\text{cov}(X, Y|Z)]}{\sqrt{E[\text{var}(X|Z)]E[\text{var}(Y|Z)]}} \quad (3.13)$$

1318 Although this is not an actual correlation, it is an intuitive analogue to the correlation as a
 1319 normalised version of the covariance.

For comparison, we also measured the ‘signal correlation’

$$\rho_{\text{signal}} = \frac{\text{cov}(E[X|Z], E[Y|Z])}{\sqrt{\text{var}(E[X|Z])\text{var}(E[Y|Z])}} \quad (3.14)$$

1320 this is an actual correlation.

1321 **3.3.4 Information Theory**

1322 **Entropy $H(X)$**

The entropy of a random variable X , with outcomes x_1, \dots, x_N , and corresponding probabilities p_1, \dots, p_N is defined as

$$H(X) = - \sum_{n=1}^N p_n \log_2 p_n \quad (3.15)$$

1323 This quantity is also known as the information entropy or the ‘surprise’. It measures the
 1324 amount of uncertainty in a random variable. For example, a variable with a probability of 1
 1325 for one outcome, and 0 for all other outcomes will have 0 bits entropy, because it contains no
 1326 uncertainty. But a variable with a uniform distribution will have maximal entropy as it is the
 1327 least predictable. This quantity is analogous to the entropy of a physical system (Shannon,
 1328 1948). Note that any base may be used for the logarithm in equation 3.15, but using base 2
 1329 means that the quantity will be measured in ‘bits’.

The joint entropy of two jointly distributed random variables X and Y , where Y has outcomes y_1, \dots, y_M , is defined as

$$H(X, Y) = - \sum_{n=1}^N \sum_{m=1}^M P(X = x_n, Y = y_m) \log_2 P(X = x_n, Y = y_m) \quad (3.16)$$

1330 If X and Y are independent then $H(X, Y) = H(X) + H(Y)$. Otherwise $H(X, Y) <$
 1331 $H(X) + H(Y)$. When X and Y are completely dependent $H(X, Y) = H(X) = H(Y)$.

The conditional entropy of Y conditioned on X is defined as

$$H(Y|X) = - \sum_{n=1}^N \sum_{m=1}^M P(X = x_n, Y = y_m) \log_2 \frac{P(X = x_n, Y = y_m)}{P(X = x_n)} \quad (3.17)$$

1332 When X and Y are independent $H(Y|X) = H(Y)$. Intuitively, we learn nothing of Y by
 1333 knowing X , so Y is equally uncertain whether we know X or not. If Y is totally dependent
 1334 on X , then the fraction in the logarithm is 1, which gives $H(Y|X) = 0$.

1335 These entropy measures are the basis of the mutual information measure.

1336 **Maximum entropy limit**

When spiking data is binned into spike counts there is an upper limit on the entropy of these data. The maximum entropy discrete distribution is the discrete uniform distribution. A

random variable with this distribution will take values from some finite set with equal probabilities. Binned spike count data will take values between 0 and some maximum observed spike count n_{\max} . A neuron with responses that maximises entropy will take these values with equal probability, i.e. if $i \in \{0, \dots, n_{\max}\}$ then $P(X = i) = \frac{1}{n_{\max} + 1}$. The entropy of this neuron will be

$$\begin{aligned} H(X) &= - \sum_{i=0}^{n_{\max}} P(X = i) \log_2 P(X = i) \\ &= - \sum_{i=0}^{n_{\max}} \frac{1}{n_{\max} + 1} \log_2 \left(\frac{1}{n_{\max} + 1} \right) \\ &= - \log_2 \left(\frac{1}{n_{\max} + 1} \right) \\ &= \log_2 (n_{\max} + 1) \end{aligned}$$

1337 Therefore, the maximum entropy of the binned spike counts of a neuron is $\log_2 (n_{\max} + 1)$.
 1338 Of course, it would be very unusual for a neuron to fire in accordance with the discrete
 1339 uniform distribution. Most measurements of entropy taken on binned spiking data will be
 1340 much lower than the maximum. See figure 3.2 to see the maximum entropy as a function of
 1341 the maximum observed spike count.

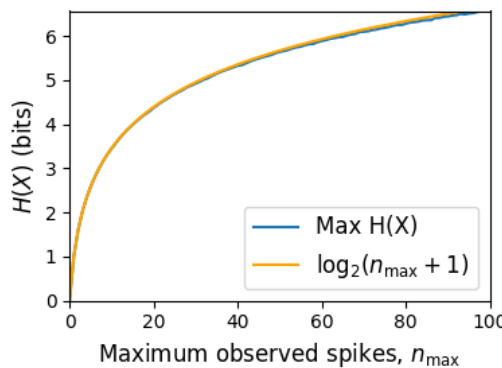


FIGURE 3.2: **Entropy Limit:** The upper limit on entropy of binned spike count data as a function of the maximum observed spike count. The orange line is the analytical maximum. The blue line is the entropy of samples with $N = 1000$ data points taken from the discrete uniform distribution.

1342 **Mutual Information $I(X; Y)$**

1343 The mutual information can be defined mathematically in a number of ways, all of which are
 1344 equivalent. These definitions illustrate the different ways of interpreting the mutual informa-
 1345 tion.

For two jointly distributed random variables X and Y , the mutual information $I(X;Y)$ is defined as

$$I(X;Y) = H(Y) - H(Y|X) \quad (3.18)$$

$$= H(X) - H(X|Y) \quad (3.19)$$

1346 Equation 3.18 fits with the following intuition: The mutual information between X and Y is
1347 the reduction in uncertainty about X gained by knowing Y , or vice versa. We could also say
1348 the mutual information is the amount of information gained about X by knowing Y , or vice
1349 versa.

Another useful entropy based definition for the mutual information is

$$I(X;Y) = H(X) + H(Y) - H(X,Y) \quad (3.20)$$

1350 This definition is useful because it does not require the calculation of conditional probabili-
1351 ties.

The mutual information can also be defined in terms of marginal, joint, and conditional distributions. For example,

$$I(X;Y) = - \sum_{n=1}^N \sum_{m=1}^M P(X = x_n, Y = y_m) \log_2 \frac{P(X = x_n, Y = y_m)}{P(X = x_n)P(Y = y_m)} \quad (3.21)$$

Notice that this can be rewritten as a Kullback–Leibler divergence.

$$I(X;Y) = D_{KL}(P(X,Y) || P(X)P(Y)) \quad (3.22)$$

1352 So, we can also think of the mutual information as a measure of the difference between
1353 the joint distribution of X and Y , and the product of their marginal distributions. Since the
1354 product of the marginal distributions is the joint distribution for independent variables, we
1355 can think of the mutual information as a measure of the variables’ dependence on one another.

1356 The minimum value that $I(X;Y)$ can take is 0. This occurs when the random variables
1357 X and Y are independent. Then we have $H(X|Y) = H(X)$, and $H(Y|X) = H(Y)$, which
1358 according to equation 3.18, gives $I(X;Y) = 0$. We also have that $H(X,Y) = H(X) +$
1359 $H(Y)$ in this case, which according equation 3.20, gives $I(X;Y) = 0$. Finally, we also have
1360 $P(X,Y) = P(X)P(Y)$, which leaves us with 1 in the argument for the logarithm in equation
1361 3.21, which again gives $I(X;Y) = 0$.

1362 The mutual information reaches its maximum value when one of the variables X and
 1363 Y is completely determined by knowing the value of the other. In that case $I(X; Y) =$
 1364 $\min\{H(X), H(Y)\}$.

1365 **Variation of Information** $VI(X, Y)$

The variation of information is another information theoretical quantity based on the mutual information. It is defined as

$$VI(X; Y) = H(X) + H(Y) - 2I(X; Y) \quad (3.23)$$

We can rewrite this as the summation of two positive quantities

$$VI(X; Y) = [H(X) - I(X; Y)] + [H(Y) - I(X; Y)] \quad (3.24)$$

1366 In English, the variation of information is the summation of the uncertainty in the random
 1367 variables X and Y excluding the uncertainty shared by those variables.

1368 This measure will become more relevant when we go on to talk about clusterings because
 1369 $VI(X; Y)$ forms a metric on the space of clusterings.

1370 **Measuring entropies & mutual information**

1371 In practice, we measured the mutual information between spike counts using Python and the
 1372 python package `pyitlib`. We used the PT-bias correction technique to estimate the bias of
 1373 our measurements when measuring the mutual information between the spike counts of two
 1374 cells (Treves and Panzeri, 1995).

1375 When measuring the mutual information between clusterings we used Python, but we
 1376 used the `mutual_info_score`, `adjusted_mutual_info_score`, and
 1377 `normalized_mutual_info_score` functions from the `sklearn.metrics` part of
 1378 the `sklearn` package.

1379 **3.3.5 Network analysis**

1380 **Correlation networks**

1381 In order to analyse functional networks created by the neurons in our ensemble, we mea-
 1382 sured the total correlation between each pair of neurons. These measurements induced an

1383 undirected weighted graph/network between the neurons. The weight of each connection
1384 was equal to the total correlation between each pair of neurons.

1385 We followed the same procedure for total correlations 3.3.2, spike count correlations, and
1386 signal correlations 3.3.3.

1387 **Rectified correlations**

1388 At the time of writing, the community detection method outlined in (Humphries et al., 2019)
1389 could only be applied to networks with positively weighted connections. But many neuron
1390 pairs were negatively correlated. To apply the community detection method, we *rectified* the
1391 network, by setting all the negative weights to zero.

1392 We also looked for structure in the network created by negative correlations by reversing
1393 the signs of the correlations, and rectifying these correlations before applying our network
1394 analysis.

1395 Finally, we used the absolute value of the correlations as the weights for the graph/network.
1396 By doing this, we hoped to identify both correlated and anti-correlated functional communi-
1397 ties of neurons.

1398 **Sparsifying data networks**

1399 When creating our correlation networks, we wanted to exclude any correlations that could
1400 be judged to exist ‘by chance’. To do this, we measured the 5th and 95th percentile of
1401 the shuffled correlations (see section 3.3.2) for the given mouse and time bin width. We
1402 then set all the data correlations between these two values to 0. This excluded any ‘chance’
1403 correlations from our network, and created a sparser network. This allowed us to make use
1404 of the ‘sparse weighted configuration model’ as described in section 3.3.5.

1405 **Communities**

1406 Given some network represented by an adjacency matrix \mathbf{A} , a community within that net-
1407 work is defined as a collection of nodes where the number of connections within these nodes
1408 is higher than the expected number of connections between these nodes. In order to quan-
1409 tify the ‘expected’ number of connections, we need a model of expected networks. This is
1410 analogous to a ‘null model’ in traditional hypothesis testing. We test the hypothesis that our
1411 data network departs from the null network model to a statistically significant degree. For
1412 undirected unweighted networks, the canonical model of a null network is the configuration

model (Fosdick et al., 2016). Since we are working with weighted sparse networks, we used more suitable null models, described below.

1415 **Weighted configuration model**

1416 The *weighted configuration model* is a canonical null network model for weighted networks.
 1417 Given some data network, the weighted configuration model null network will preserve the
 1418 degree sequence and weight sequence of each node in the data network. But the edges will
 1419 be distributed randomly (Fosdick et al., 2016). Any structure in the data network beyond
 1420 its degree sequence and weight sequence will not be captured in the weighted configuration
 1421 model. So, this model can be used in testing the hypothesis that this extra structure exists.

1422 **Sparse weighted configuration model**

1423 The *sparse weighted configuration model* is another null network model. Similar in nature to
 1424 the weighted configuration model (see section 3.3.5), but the sparsity of the data network is
 1425 preserved in the null network. This is achieved by sampling from a probability distribution
 1426 for the creation or non-creation of each possible connection, then distributing the weight of
 1427 the data network randomly in this sparse network (Humphries et al., 2019). This is the null
 1428 network that we used when searching for additional structure in our data networks.

1429 **Spectral rejection**

1430 We made use of the spectral rejection algorithm as outlined in (Humphries et al., 2019). The
 1431 spectral rejection algorithm is a method for finding structure in a network not captured by a
 1432 supposed null model, if such structure exists.

To describe the method, we denote our data network matrix \mathbf{W} , we denote the expected network of our null network model as $\langle \mathbf{P} \rangle$. Then the departure of our data network from the null network can be described by the matrix

$$\mathbf{B} = \mathbf{W} - \langle \mathbf{P} \rangle \quad (3.25)$$

1433 a common choice for $\langle \mathbf{P} \rangle$ in community detection is the ‘configuration model’ (Fosdick et
 1434 al., 2016; Humphries, 2011). The matrix \mathbf{B} is often called the configuration matrix, in this
 1435 context we will use the term ‘deviation matrix’ as it captures the deviation of \mathbf{W} from the
 1436 null model.

1437 To test for structure in the network represented by \mathbf{W} , we examine the eigenspectrum of \mathbf{B}
1438 and compare it to the eigenspectrum of our null model. Firstly, note that since our data model
1439 doesn't allow self loops, and is not directed, the matrix representing the network will be
1440 symmetric and positive semi-definite, and will therefore be invertible with real eigenvalues.
1441 We selected a null model with the same characteristics.

1442 To find the eigenspectrum of the null model, we generated N samples from our null
1443 model P_1, \dots, P_N , and we measured their deviation matrices B_1, \dots, B_N . We then calculated
1444 the eigenspectrum of each of those samples. We calculated the upper bound of the null model
1445 eigenspectrum by taking the mean of the largest eigenvalues of B_1, \dots, B_N . We calculated a
1446 lower bound on the null model eigenspectrum by taking the mean of the smallest eigenvalues
1447 of B_1, \dots, B_N .

1448 We then calculated the eigenspectrum of \mathbf{B} , our data network deviation matrix. If any of
1449 those eigenvalues lay outside of the upper or lower bounds of the null model eigenspectrum,
1450 this is evidence of additional structure not captured by the null model. If we chose the sparse
1451 weighted configuration model (see section 3.3.5) as our null network model, then eigenvalues
1452 lying below the lower bound indicate k -partite structure in the network. For example, if one
1453 eigenvalue lay below the lower bound, this would indicate some bipartite structure in the data
1454 network. If any eigenvalues lay above the upper bound of the null model eigenspectrum, this
1455 is evidence of community structure in the data network. For example, one eigenvalue of \mathbf{B}
1456 lying above the upper bound of the null model eigenspectrum indicates the presence of two
1457 communities in the network (Humphries, 2011).

1458 **Node rejection**

1459 If there are d data eigenvalues lying outside of the null network eigenspectrum, the d eigen-
1460 vectors corresponding to these eigenvalues will form a vector space. If we project the nodes
1461 of our network into this vector space, by projecting either rows or columns of the data ma-
1462 trix, we can see how strongly each node contributes to the vector space. Nodes that contribute
1463 strongly to the additional structure will project far away from the origin, nodes that do not
1464 contribute to the additional structure will project close to the origin. We want to use this
1465 information to discard those nodes that do not contribute.

1466 We can test whether a node projects *far* away from the origin or *close* to the origin
1467 using the eigenvalues and eigenvectors of B_1, \dots, B_N . The j th eigenvector and eigenvalue
1468 of B_i gives a value for a null network's projection into the j th dimension of the additional
1469 structure vector space. The matrices B_1, \dots, B_N give N projections into that dimension.

1470 These projections are a distribution of the null networks' projections. If the data node's
 1471 projection exceeds that of the null network projections this node is judged to project *far* from
 1472 the origin, and therefore contribute to the additional structure. Otherwise, the node is judged
 1473 to project *close* to the origin, and is therefore rejected (Humphries et al., 2019).

1474 **Community detection**

1475 Another application for this d dimensional space is community detection. We first project
 1476 all of the nodes into this d -dimensional space, then perform the clustering in this space. The
 1477 clustering and community detection procedure is described in (Humphries, 2011).

1478 In practice, the procedure is carried out n times (we chose $n = 100$ times), this returns n
 1479 clusterings. We resolve these n clusterings to one final clustering using *consensus clustering*.
 1480 We used the consensus clustering method that uses an explicit null model for the consensus
 1481 matrix, as outlined in (Humphries et al., 2019).

1482 **3.3.6 Clustering Comparison**

A clustering \mathcal{C} is a partition of a set D into sets C_1, C_2, \dots, C_K , called clusters, that satisfy the following for all $k, l \in \{1, \dots, K\}$:

$$C_k \cap C_l = \emptyset \quad (3.26)$$

$$\bigcup_{k=1}^K C_k = D \quad (3.27)$$

1483 If we consider two clusterings, \mathcal{C} with clusters C_1, C_2, \dots, C_K and \mathcal{C}' with clusters
 1484 C'_1, C'_2, \dots, C'_K . There are a number of measurements we can use to compare \mathcal{C} and \mathcal{C}' . In
 1485 the following, the number of elements in D is denoted by n , and the number of elements in
 1486 cluster C_k is n_k .

1487 **Adjusted Rand Index**

1488 The *adjusted Rand Index* is a normalised similarity measure for clusterings based on pair
 1489 counting.

1490 If we consider the clusterings \mathcal{C} and \mathcal{C}' , and denote

1491 • the number of pairs in the same cluster in \mathcal{C} and \mathcal{C}' by N_{11}

1492 • the number of pairs in different clusters in \mathcal{C} and \mathcal{C}' by N_{00}

- 1493 • the number of pairs in the same cluster in \mathcal{C} and different clusters in \mathcal{C}' by N_{10}

- 1494 • the number of pairs in different clusters in \mathcal{C} and the same cluster in \mathcal{C}' by N_{01}

then the *Rand Index* is defined as

$$RI = \frac{N_{11} + N_{00}}{N_{11} + N_{00} + N_{10} + N_{01}} = \frac{N_{11} + N_{00}}{\binom{n}{2}} \quad (3.28)$$

1495 The Rand Index is 1 when the clusterings are identical, and 0 when the clusterings are com-
1496 pletely different.

The *adjusted Rand Index* intends on correcting the Rand Index for chance matching pairs.

This is defined as

$$ARI = \frac{2(N_{00}N_{11} - N_{01}N_{10})}{(N_{00} + N_{01})(N_{01} + N_{11}) + (N_{00} + N_{10})(N_{10} + N_{11})} \quad (3.29)$$

1497 The adjusted Rand Index is 1 when the clusterings are identical, and 0 when the Rand Index
1498 is equal to its expected value.

1499 Clusterings as random variables

If we take any random element of D , the probability that this element is in cluster C_k of clustering \mathcal{C} is

$$P(K = k) = \frac{n_k}{n} \quad (3.30)$$

1500 this defines a probability distribution, which makes the clustering a random variable. Any
1501 clustering can be considered as a random variable this way.

This means that we can measure any of the information theoretic quantities defined in section 3.3.4 with respect to clusterings. For example, the entropy of a clustering is

$$H(\mathcal{C}) = - \sum_{k=1}^K \frac{n_k}{n} \log \frac{n_k}{n} \quad (3.31)$$

If we have two clusterings, the joint probability distribution of these clusterings is defined as

$$P(K = k, K' = k') = \frac{|C_k \cap C'_{k'}|}{n} \quad (3.32)$$

1502 The joint distribution allows us to define the mutual information between two clusterings,
1503 $I(\mathcal{C}; \mathcal{C}')$ (Meilă, 2007).

1504 **Information based similarity measures**

The mutual information between two clusterings is a similarity measure, with $I(\mathcal{C}; \mathcal{C}') = 0$ if \mathcal{C} and \mathcal{C}' are completely different, and $I(\mathcal{C}; \mathcal{C}') = H(\mathcal{C}) = H(\mathcal{C}')$ if \mathcal{C} and \mathcal{C}' are identical. This can be normalised in a number of different ways to make more similarity measures (Vinh, Epps, and Bailey, 2010)

$$NMI_{joint} = \frac{I(\mathcal{C}; \mathcal{C}')}{H(\mathcal{C}, \mathcal{C}')} \quad (3.33)$$

$$NMI_{max} = \frac{I(\mathcal{C}; \mathcal{C}')}{\max\{H(\mathcal{C}), H(\mathcal{C}')\}} \quad (3.34)$$

$$NMI_{sum} = \frac{2I(\mathcal{C}; \mathcal{C}')}{H(\mathcal{C}) + H(\mathcal{C}')} \quad (3.35)$$

$$NMI_{sqrt} = \frac{I(\mathcal{C}; \mathcal{C}')}{\sqrt{H(\mathcal{C})H(\mathcal{C}')}} \quad (3.36)$$

$$NMI_{min} = \frac{I(\mathcal{C}; \mathcal{C}')}{\min\{H(\mathcal{C}), H(\mathcal{C}')\}} \quad (3.37)$$

We can control for chance similarities between the two clusterings by measuring the *adjusted mutual information* between the clusterings. This is defined as

$$AMI_{sum} = \frac{I(\mathcal{C}; \mathcal{C}') - E\{I(\mathcal{C}; \mathcal{C}')\}}{\frac{1}{2}[H(\mathcal{C}) + H(\mathcal{C}')] - E\{I(\mathcal{C}; \mathcal{C}')\}} \quad (3.38)$$

1505 The first term in the denominator, taking the average of the marginal entropies, can be re-
 1506 placed by taking the maximum, minimum, or the geometric mean (Vinh, Epps, and Bailey,
 1507 2010).

1508 **Information based metrics**

The variation of information between two clusterings $VI(\mathcal{C}; \mathcal{C}')$ (see section 3.3.4) is a metric on the space of clusterings (Meilă, 2007). That is,

$$VI(\mathcal{C}; \mathcal{C}') \geq 0 \quad (3.39)$$

$$VI(\mathcal{C}; \mathcal{C}') = 0 \iff \mathcal{C} = \mathcal{C}' \quad (3.40)$$

$$VI(\mathcal{C}; \mathcal{C}') = VI(\mathcal{C}'; \mathcal{C}) \quad (3.41)$$

$$VI(\mathcal{C}; \mathcal{C}'') \leq VI(\mathcal{C}; \mathcal{C}') + VI(\mathcal{C}'; \mathcal{C}'') \quad (3.42)$$

Another metric is the *information distance* (Vinh, Epps, and Bailey, 2010)

$$D_{max} = \max\{H(\mathcal{C}), H(\mathcal{C}')\} - I(\mathcal{C}; \mathcal{C}') \quad (3.43)$$

Both of these can be normalised

$$NVI(\mathcal{C}; \mathcal{C}') = 1 - \frac{I(\mathcal{C}; \mathcal{C}')}{H(\mathcal{C}, \mathcal{C}')} \quad (3.44)$$

$$d_{max} = 1 - \frac{I(\mathcal{C}; \mathcal{C}')}{\max\{H(\mathcal{C}), H(\mathcal{C}')\}} \quad (3.45)$$

1509 Comparing detected communities and anatomical divisions

1510 In order to quantify the difference or similarity between the communities detected in our cor-
 1511 relation network and the anatomical classification of the cells in that network, we considered
 1512 the communities and the anatomical regions as clusters in two different clusterings, \mathcal{C}_{comm}
 1513 and \mathcal{C}_{anat} , respectively. We then measured the similarity between the clusterings using the
 1514 mutual information, the adjusted mutual information, and the normalised mutual informa-
 1515 tion. We measured the difference between, or the distance between, the clusterings using the
 1516 variation of information, the normalised variation of information, and the normalised infor-
 1517 mation distance. We also measured the difference between the clusterings using the adjusted
 1518 Rand Index, just to use a non-information based measure.

1519 We took all of these measures for communities detected using different time bin widths.
 1520 This gave us an idea of the effect of time bin width on correlation networks in neural ensem-
 1521 bles relative to anatomical regions within those ensembles.

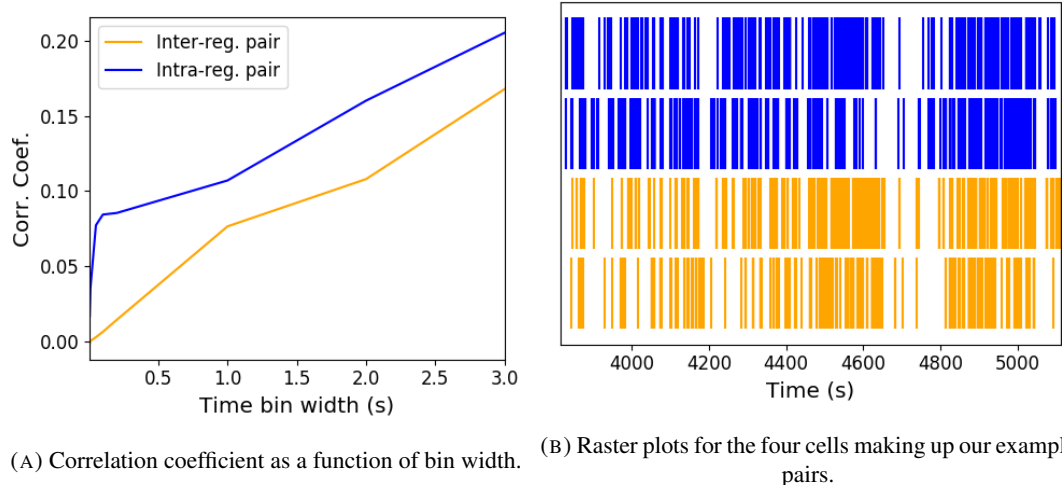
1522 3.4 Results

1523 Note that in the following text, we refer to the correlation coefficient between two sequences
 1524 of spike counts from two different cells as the *total correlation*. We refer to the correlation
 1525 between spike counts in response to a certain stimulus as the *spike count correlation* aka
 1526 *noise correlation*, and we refer to the correlation between mean or expected responses to
 1527 different stimuli as the *signal correlation* (Cohen and Kohn, 2011).

1528 The nine different brain regions from which we had data were the caudate putamen (CP),
 1529 frontal motor cortex (FrMoCtx), hippocampus (HPF), lateral septum (LS), midbrain (MB),
 1530 primary visual cortex (V1), superior colliculus (SC), somatomotor cortex (SomMoCtx), and
 1531 thalamus (TH).

1532 **3.4.1 Average correlation size increases with increasing time bin width**

1533 First we inspected the affect of time bin width on total correlations. We know that using short
 1534 time bins results in artificially small correlation measurements (Cohen and Kohn, 2011), so
 1535 we expected to see an increase in correlation amplitude with increasing time bin width. That
 1536 is exactly what we observed. Taking 50 cells at random, we calculated the total correla-
 1537 tion between every possible pair of these cells, using different time bin widths ranging from
 1538 0.005s to 3s. We found that the longer the time bin width, the greater the correlations (see
 1539 figure 3.4a).



(A) Correlation coefficient as a function of bin width. (B) Raster plots for the four cells making up our example pairs.

FIGURE 3.3: (A) An example of the correlation coefficients between two different pairs of cells, one where both cells are in the same brain region (intra-regional pair), and one where both cells are in different brain regions (inter-regional pair). The correlation coefficients have been measured using different time bin widths, ranging from 5ms to 3s. Note the increasing amplitude of the correlations with increasing bin width. (B) A raster plot showing the spike times of each pair of cells.

1540 We also separated the positively correlated pairs from the negatively correlated pairs
 1541 using the mean correlation of each pair across all bin widths (see section 3.3.2). We found
 1542 that the positively correlated pairs become more positively correlated with increasing time bin
 1543 width, and the negatively correlated pairs become more negatively correlated with increasing
 1544 time bin width (see figures 3.4b and 3.4c).

1545 In figure 3.3a we plot correlations from two example pairs, one pair from within a region,
 1546 and one pair between regions. It can be seen that the correlation coefficient increases with
 1547 bin width. The correlations can be observed by eye in the raster plot for these cells in figure
 1548 3.3b.

1549 When taking the mean across all pairs, the positively correlated pairs dominate in terms
 1550 of both number of pairs, and amplitude of correlations. Therefore the mean across all pairs

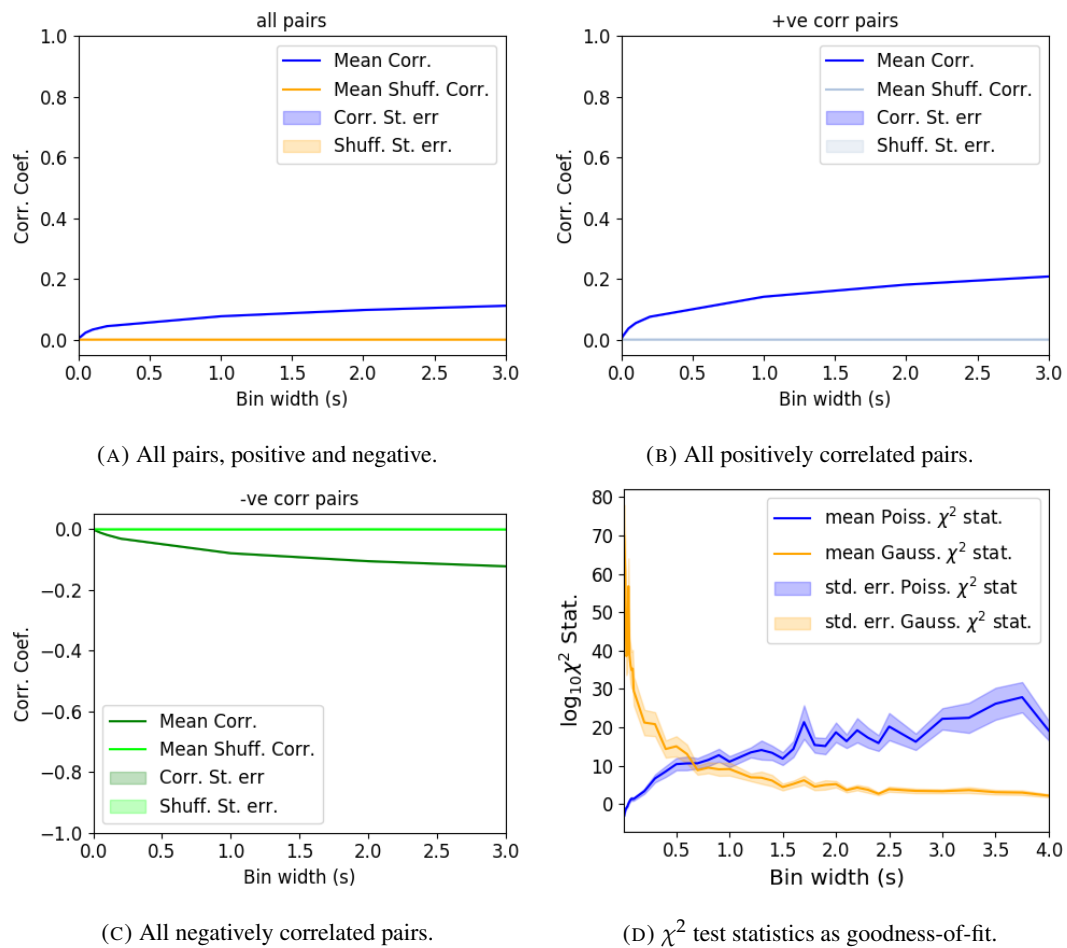


FIGURE 3.4: Mean correlation coefficients measured from pairs of 50 randomly chosen neurons. (A) All possible pairs, (B) positively correlated pairs, and (C) negatively correlated pairs. (D) Mean and standard error of χ^2 test statistics for Poisson and Gaussian distributions fitted to neuron spike counts.

1551 is positive.

1552 These results were observed in each of the three mouse subjects from which we had data.

1553 **3.4.2 Goodness-of-fit for Poisson and Gaussian distributions across increasing
1554 time bin widths**

1555 We wanted to investigate if the width of the time bin used to bin spike times into spike counts
1556 had an effect on the distribution of spike counts. We used the χ^2 statistic as a goodness-of-fit
1557 measure for Poisson and Gaussian (normal) distributions to the spike count of 100 randomly
1558 chosen neurons for a number of bin widths ranging from 0.01s to 4s. For the χ^2 statistic, the
1559 higher the value, the worse the fit.

1560 We expected a Poisson distribution to be a better fit for shorter time bin widths because
1561 spike counts must be non-negative, therefore any distribution of spike counts with mass dis-
1562 tributed at or close to 0 will be skewed. The distribution of spike counts is more likely to be
1563 distributed close to 0 when the time bin widths used to bin spike times into spike counts are
1564 small relative to the amount of time it takes for a neuron to fire an action potential ($\sim 1\text{ms}$ in
1565 the case of non-burst firing neurons).

1566 We expected a Gaussian distribution to be a better fit for longer time bin widths, because
1567 a Poisson distribution with a large rate is well approximated by a Gaussian distribution with
1568 mean and variance equal to the Poisson rate. Therefore, a Gaussian distribution would ap-
1569 proximate the mean of a collection of large spike counts, and have more flexibility than a
1570 Poisson distribution to fit the variance.

1571 We found that that a Poisson distribution is the best fit for shorter time bins less than 0.7s
1572 in length. Then a Gaussian distribution is a better fit for time bins greater than 0.7s in length
1573 (see figure 3.4d).

1574 **3.4.3 Differences between and inter- and intra- regional correlations decrease
1575 with increasing bin width**

1576 We investigated the differences in distribution between inter-regional correlations, i.e. corre-
1577 lations between neurons in different brain regions, and intra-regional correlations, i.e. corre-
1578 lations between neurons in the same brain region.

1579 Firstly, we investigated these quantities for all possible pairs of ~ 500 neurons taken
1580 from across all the 9 brain regions from which we had data. We distributed these neurons as
1581 evenly as possible across all of the regions, so that cells from one region would not dominate
1582 our data. We observed that the mean intra-regional correlations were always higher than the

mean inter-regional correlations for every value of time bin width used. We also observed that as the time bin width increased these mean correlations increased and the difference between the mean inter-regional and intra-regional correlations grew (see figure 3.5 (Left)).

Stringer et al. (2019) had a similar finding using the same data. They used only one value for the time bin width, 1.2s. Using this time bin width to bin spike times and measure total correlations, they found that the mean ‘within-region’ correlations were always greater than the ‘out-of-region’ correlations (Stringer et al., 2019). The figure from their paper showing this result can be seen in figure 3.5 (Right).

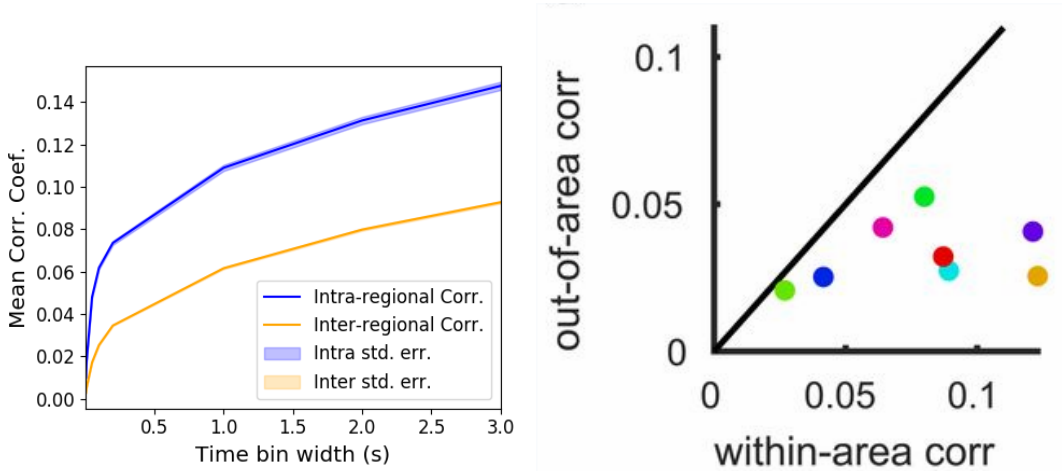
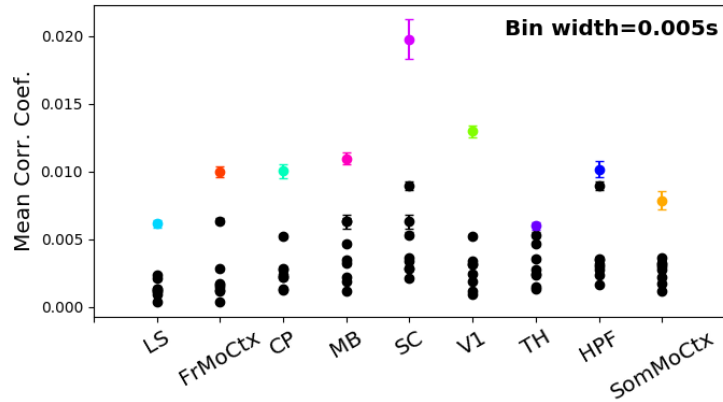


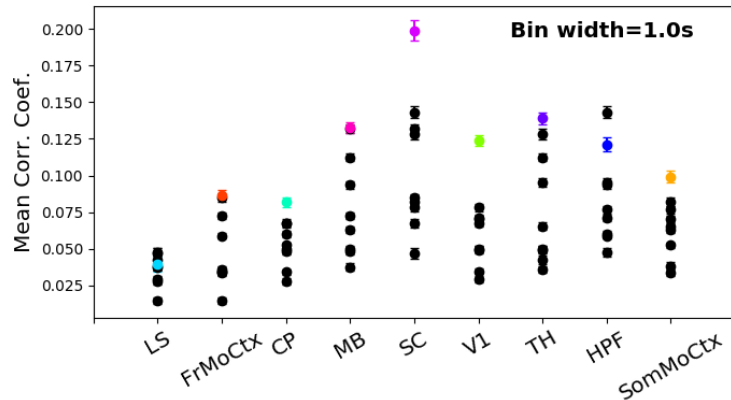
FIGURE 3.5: (Left)The mean intra-region and inter-region correlations using all possible pairs of ~ 500 neurons, spread across 9 different brain regions. (Right) Courtesy of Stringer et al. (2019), mean inter-regional (out-of-area) correlation coefficients vs mean intra-regional (within-area) correlation coefficients for a bin width of 1.2s. Note that the intra-regional coefficients are higher in each case.

Examples of the correlations of one intra-regional pair and one inter-regional pair can be seen in figure 3.3.

Secondly, we separated those pairs into intra-regional and inter-regional groups. We noted that the mean intra-regional correlations (coloured dots in figures 3.6a and 3.6b) for a given region tended to be higher than the mean inter-regional correlations (black dots in figures 3.6a and 3.6b) involving cells from that region. However, in contrast with our previous result, we noted that the difference between the mean intra-regional correlations and most highly correlated inter-regional correlations reduced as we increased the time bin width (see figures 3.6a and 3.6b). This shows that the mean correlations shown in figure 3.5 are not distributed evenly across all region pair combinations.



(A) Mean inter-regional and intra-regional correlations using a time bin width of 5ms.

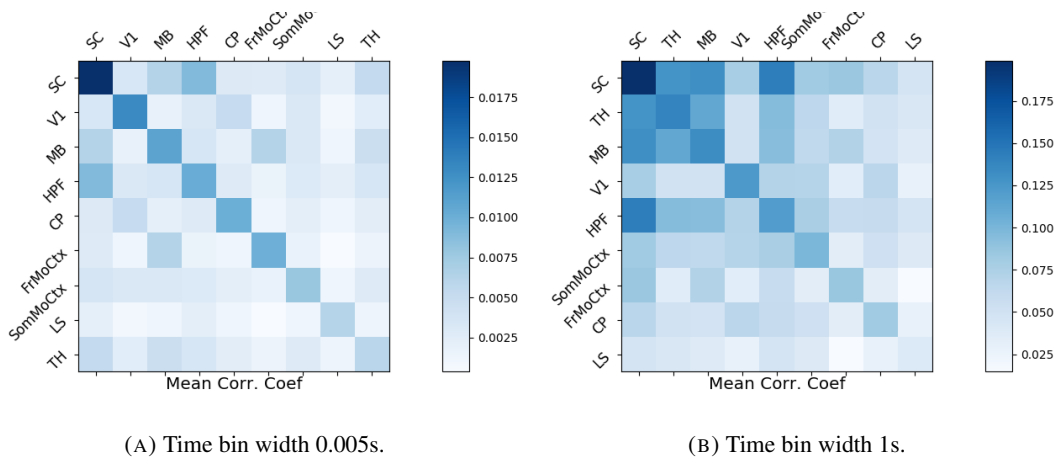


(B) Mean inter-regional and intra-regional correlations using a time bin width of 1s.

FIGURE 3.6: The mean intra-regional correlations (coloured dots) and mean inter-regional correlations (black dots) for a given region, indicated on the x-axis, for different time bin widths. Each black dot represents the mean inter-regional correlations between the region indicated on the x-axis and one other region. (A) shows these measurements when we used a time bin width of 5ms. (B) shows these measurements when we used a time bin width of 1s. Note that the difference between the mean inter-regional correlations and mean intra-regional correlations is smaller for 1s bins.

Finally, to see these regional mean correlations in a bit more detail, to examine the individual pair combinations in particular, we displayed these data in a matrix of mean correlations (see figure 3.7), showing the mean intra-regional correlations on the main diagonal, and the mean inter-regional correlations off diagonal. Comparing a version of this figure created using a short time bin width of 5ms (figure 3.7a) and a version using a longer time bin width of 1s (figure 3.7b) we observed that the mean intra-regional correlations are always relatively high in comparison to the mean inter-regional correlations, but the mean correlations in some inter-regional pairs are relatively much higher when using the longer time bin width.

This could indicate information being processed quickly at a local or within-region level, and the local representations of this information spreading between regions at longer timescales.



(A) Time bin width 0.005s.

(B) Time bin width 1s.

FIGURE 3.7: Mean inter-regional (main diagonal) and intra-regional (off diagonal) correlation coefficients. (A) Shows these measurements when spike times were binned using 5ms time bins. (B) Shows the same, using 1s time bins. Note that the matrices are ordered according to the main diagonal values, therefore the ordering is different in each subfigure.

These results were consistent across the three mouse subjects. But, the relative magnitudes of the mean intra-regional and inter-regional correlations were not consistent. For example, the region with the highest mean intra-regional correlations when using 1s bin widths for subject one is the superior colliculus (SC), but for subject two it is the midbrain (MB).

3.4.4 Connected and divided structure in correlation based networks reduces in dimension with increasing bin width

We used the correlation measurements to create weighted undirected graphs/networks where each node represents a neuron, and the weight of each edge is the pairwise correlation between those neurons represented by the nodes at either end of that edge. We aimed to find

1620 communities of neurons within these networks, and compare the structure of these commu-
1621 nities to the anatomical division of those neurons. The first step of this process involved
1622 applying the ‘spectral rejection’ technique developed by Humphries et al (2019) (Humphries
1623 et al., 2019). This technique compares our data network to a chosen null network model, and
1624 finds any additional structure in the data network beyond that which is captured in the null
1625 network model (if there is any such structure).

1626 By comparing the eigenspectrum of the data network to the eigenspectrum of many sam-
1627 ples from the null network model, this technique allows us to estimate the dimensionality of
1628 the additional structure in the data network, and gives us a basis for that vector space. It also
1629 divides the additional structure into connected structure, and k -partite (or divided) structure.
1630 For example, if our algorithm found two dimensions of additional connected structure, and
1631 one dimension of additional divided structure. We might expect to find three communities,
1632 that is groups more strongly connected within group than without, and we might expect to
1633 find bi-partite structure, that is two sets that are more strongly connected between groups
1634 than within groups.

1635 The technique also finds which nodes contribute to this additional structure, and divides
1636 our data network into signal and noise networks. The details of spectral rejection and node
1637 rejection can be found in sections 3.3.5 and 3.3.5 respectively, and a full overview can be
1638 found in (Humphries et al., 2019).

1639 We chose the sparse weighted configuration model (see section 3.3.5) as our null network
1640 model. This model matches the sparsity and the total weight of the original network but
1641 distributes the weight at random across the sparse network.

1642 We applied the spectral rejection method to our networks based on total correlations using
1643 different values for the time bin width. We observed that for smaller time bin widths, our data
1644 networks had both k -partite structure, and community structure. As the width of the time bin
1645 increased, we found that the k -partite structure disappeared from our data networks, and the
1646 dimension of the community structure reduced in two of the three mice from which we had
1647 data (see figure 3.8).

1648 **3.4.5 Detecting communities in correlation based networks**

1649 We applied the community detection procedure described in section 3.3.5 to our signal net-
1650 works for our various time bin widths. We detected a greater number of smaller communities
1651 at shorter time bin widths, and a smaller number of larger communities for longer time bin
1652 widths (see figure 3.9). This was expected after the results found in section 3.4.4. We found

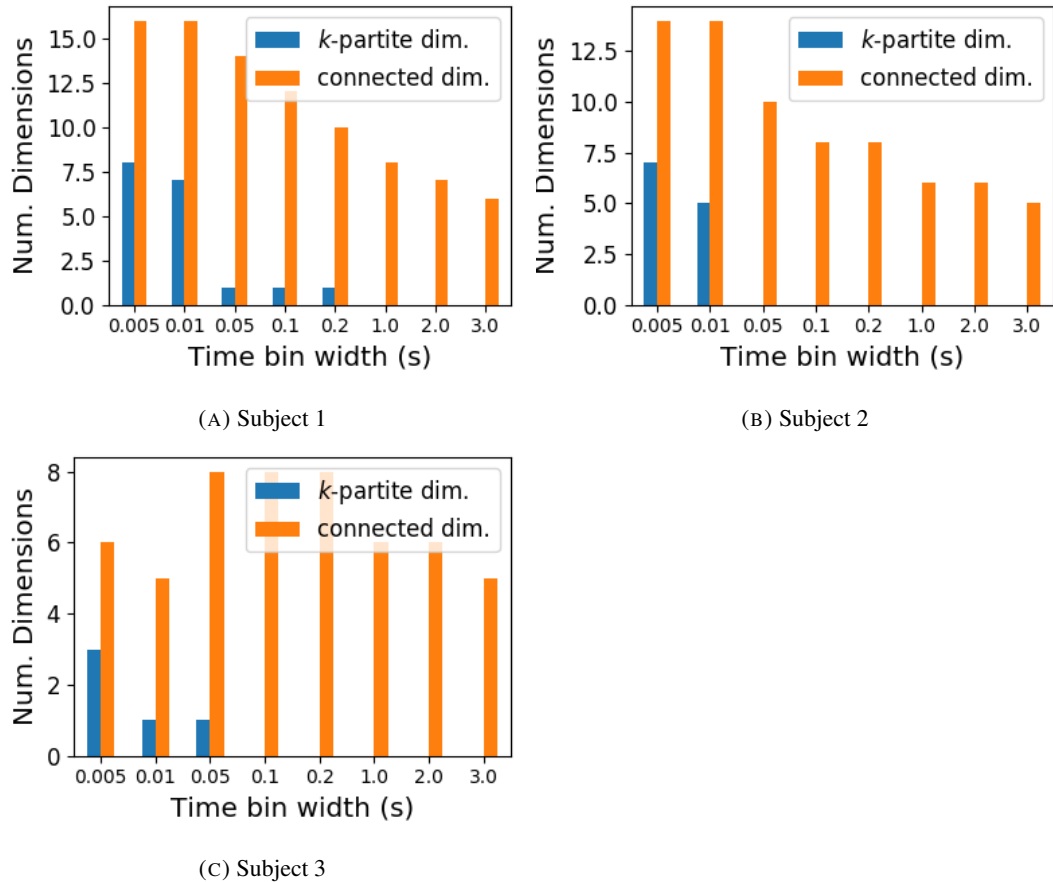


FIGURE 3.8: The number of dimensions in the *k*-partite and connected structure in the correlation based networks beyond the structure captured by a sparse weighted configuration null network model (see section 3.3.5), shown for different time bin widths. Note that the *k*-partite structure disappears for time bin width greater than 200ms for all three subjects. The dimension of the connected structure reduces with increasing bin width for 2 of the 3 subjects (top row).

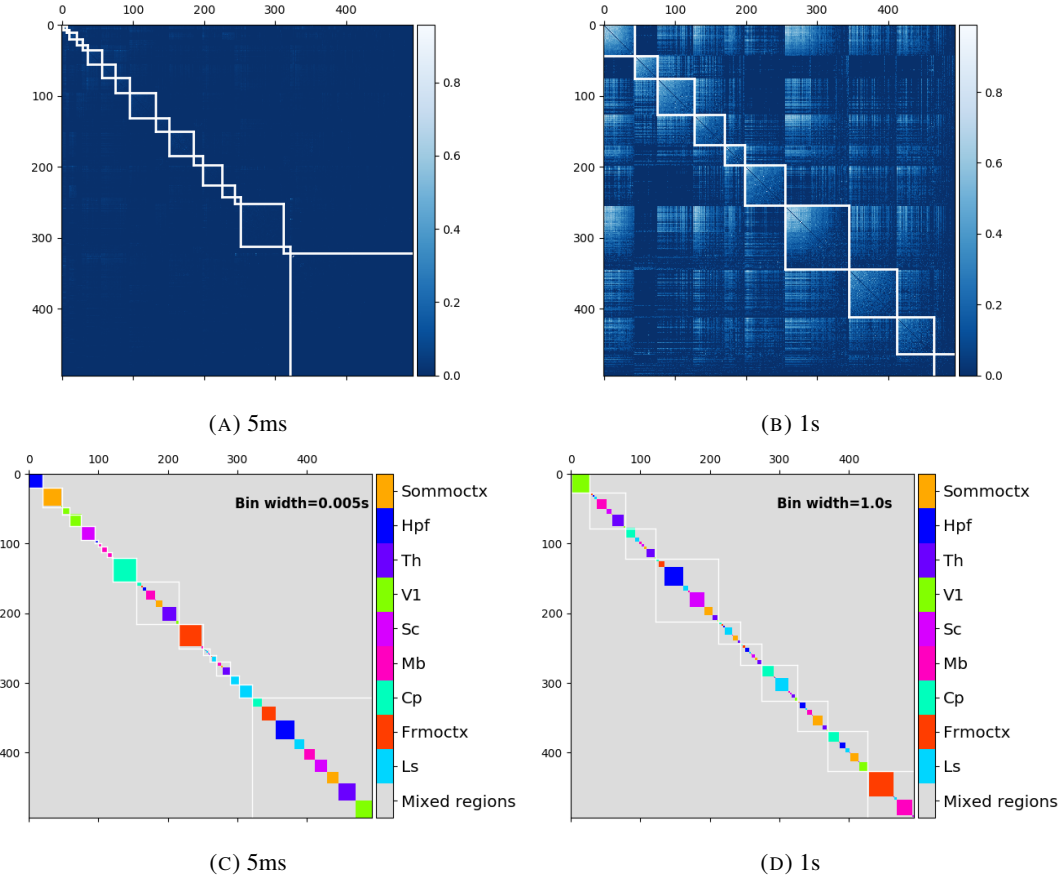


FIGURE 3.9: (A-B) Correlation matrices with detected communities indicated by white lines. Each off main diagonal entry in the matrix represents a pair of neurons. Those entries within a white square indicate that both of those neurons are in the same community as detected by our community detection procedure. Matrices shown are for 5ms and 1s time bin widths respectively. Main diagonal entries were set to 0. (C-D) Matrices showing the anatomical distribution of pairs along with their community membership. Entries where both cells are in the same region are given a colour indicated by the colour bar. Entries where cells are in different regions are given the grey colour also indicated by the colour bar.

1653 more dimensions of additional structure at shorter time bin widths, therefore we found more
1654 communities at shorter time bin widths.

1655 We also noticed that at short time bin widths the communities detected tended to be
1656 dominated by cells from one region. Whereas communities existing in networks created
1657 using wider time bin widths tended to contain cells from many different brain regions. More
1658 on this in the next section.

1659 **3.4.6 Functional communities resemble anatomical division at short timescales**

1660 In order to quantify the similarity of the communities detected to the anatomical division of
1661 the cells. We treated both the anatomical division and the communities as clusterings of these
1662 cells. We then used measures for quantifying the difference or similarity between clusterings
1663 to quantify the difference or similarity between the detected communities and the anatomical
1664 division. Details of these measures can be found in section 3.3.6 or in (Vinh, Epps, and
1665 Bailey, 2010).

1666 We used two different types of measures for clustering comparison; information based
1667 measures (see section 3.3.6) and pair counting based measures (see section 3.3.6). We include
1668 one example of each in figure 3.10.

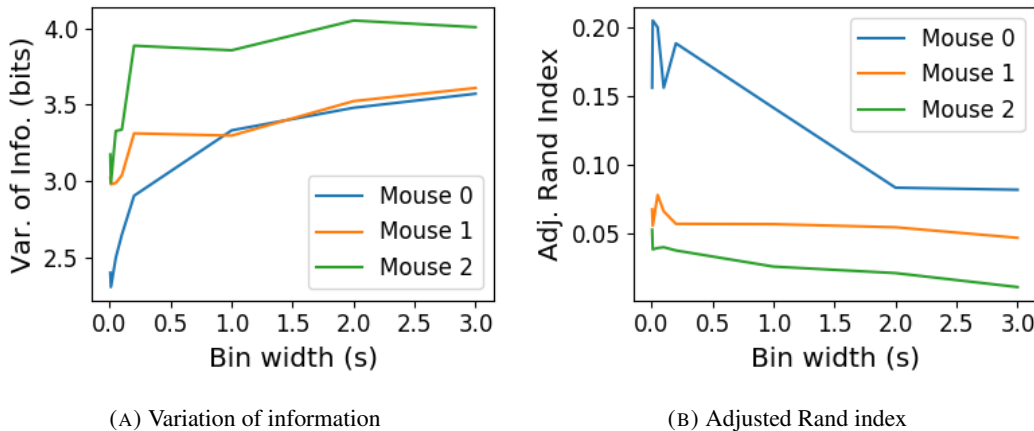
1669 The variation of information is the information based measure included in figure 3.10a.
1670 This measure forms a metric on the space of clusterings. The larger the value for the variation
1671 of information, the more different the clusterings.

1672 The adjusted Rand index is the pair counting based measure included in figure 3.10b. In
1673 contrast with the variation of information, the adjusted Rand index is a normalised similarity
1674 measure. The adjusted Rand index takes value 1 when the clusterings are identical, and takes
1675 value 0 when the clusterings are no more similar than chance.

1676 Both measures indicated that the detected communities and the anatomical division of
1677 the cells were more similar when we used shorter time bins widths (see figure 3.10). This
1678 indicates that correlated behaviour in neuronal ensembles is more restricted to individual
1679 brain regions at short timescales (< 250ms), and the correlated activity spreads out across
1680 brain regions over longer time scales.

1681 **3.4.7 Conditional correlations & signal correlations**

1682 In light of the excellent research of Stringer et al (2019) showing that spontaneous behaviours
1683 can drive activity in neuronal ensembles across the visual cortex and midbrain (Stringer et
1684 al., 2019), we decided to control for the mouse's behaviour when performing our analyses.



(A) Variation of information

(B) Adjusted Rand index

FIGURE 3.10: (A) The variation of information is a measure of distance between clusterings. The distance between the anatomical ‘clustering’ and community detection ‘clustering’ increases with increasing time bin width. (B) The adjusted Rand index is a normalised similarity measure between clusterings. The anatomical and community detection clusterings become less similar as the time bin width increases.

1685 It is possible that our community detection process may be detecting communities across
 1686 multiple brain regions at longer time scales due to aggregating neuronal activity driven by
 1687 several spontaneous behaviours occurring during the time interval covered by a given time
 1688 bin. A time bin of 1s, for example, could contain a spike count where those spikes were driven
 1689 by different spontaneous behaviours. We aimed to investigate this possibility by applying our
 1690 community detection analysis to conditional correlation measures.

1691 We used the top 500 principal components of a video of the mouse’s face as a measure of
 1692 the mouse’s behaviour (see section 3.2.2). We modelled the spike counts as a linear combi-
 1693 nation of the principal components using linear regression with ElasticNet regularisation (see
 1694 section 3.3.3). Using this model, we quantified the expected spike count given the mouse’s
 1695 behaviour $E[X|Z_1, \dots, Z_{500}]$.

1696 We used these expected values to measure $\text{cov}(E[X|Z], E[Y|Z])$, and we used that value,
 1697 the covariance $\text{cov}(X, Y)$, and the *law of total covariance* (see section 3.3.3) to measure
 1698 $E[\text{cov}(X, Y|Z)]$. Here X and Y represent spike counts from individual cells, and Z is short-
 1699 hand for the 500 principal components mentioned above. The two components of the co-
 1700 variance, $\text{cov}(E[X|Z], E[Y|Z])$ and $E[\text{cov}(X, Y|Z)]$, represent a ‘signal covariance’ and ex-
 1701 pected value of a ‘spike count covariance’ respectively, analogous to the signal correlation
 1702 and spike count correlation (Cohen and Kohn, 2011).

1703 We examined the means of these components for different values of the time bin width
 1704 (see figure 3.11). We observed a consistent increase in $E[\text{cov}(X, Y|Z)]$ as the time bin width
 1705 increased. But we saw different trends for $\text{cov}(E[X|Z], E[Y|Z])$ for each mouse.

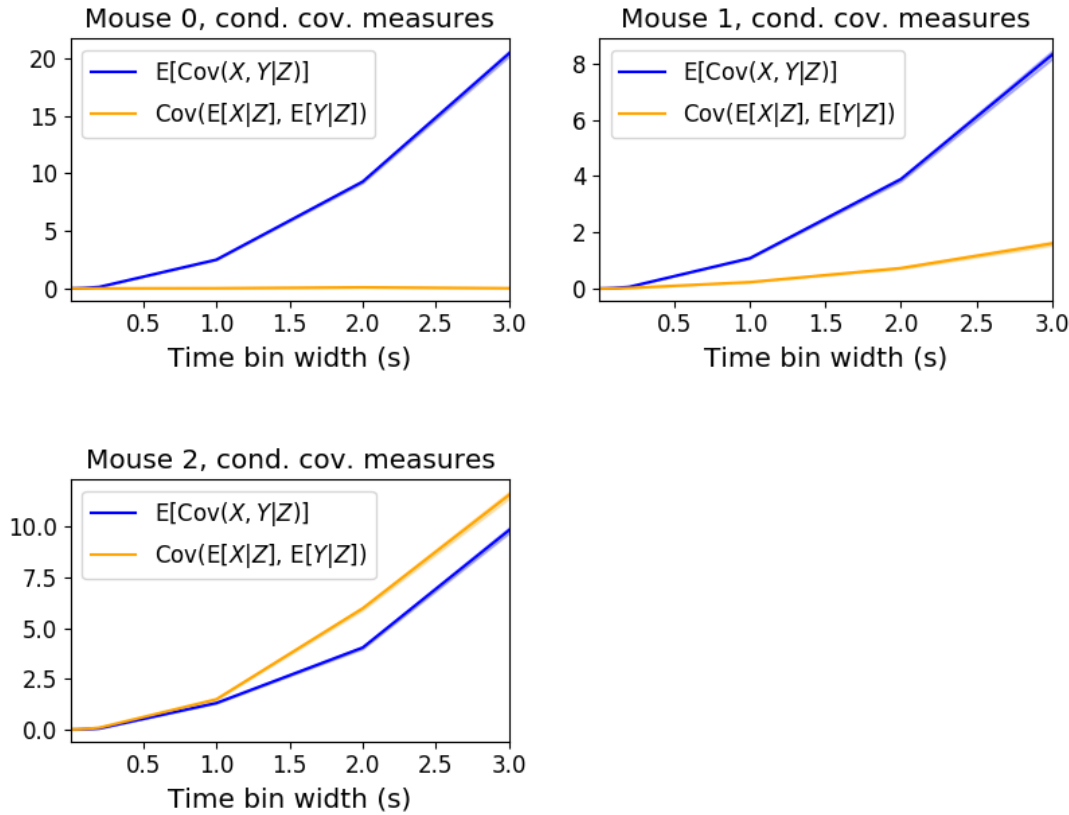


FIGURE 3.11: Comparing the components of the total covariance across different values for the time bin width. We observed a consistent increase in $E[\text{cov}(X, Y|Z)]$ as the time bin width increased. But we saw different trends for $\text{cov}(E[X|Z], E[Y|Z])$ for each mouse.

1706 Using $\text{cov}(E[X|Z], E[Y|Z])$ we measured the signal correlation, ρ_{signal} , and using $E[\text{cov}(X, Y|Z)]$
 1707 we measured the event conditional correlation, $\rho_{X,Y|Z}$ (see section 3.3.3 for more details).
 1708 We saw a consistent increase in $\rho_{X,Y|Z}$ as the time bin width increased, this corresponds to
 1709 the result for $E[\text{cov}(X, Y|Z)]$. We observed different trends for ρ_{signal} for each mouse, this
 1710 corresponds to the result for $\text{cov}(E[X|Z], E[Y|Z])$.

1711 We applied our network noise rejection and community detection process to networks
 1712 based on the spike count correlations $\rho_{X,Y|Z}$ and the signal correlations ρ_{signal} . We noted that
 1713 the community detection on $\rho_{X,Y|Z}$ behaved similarly to the community detection on the total
 1714 correlation. We can see this in figures 3.13a and 3.13b. At very short time bin widths, we
 1715 detect more communities, and those communities often contain cells from one brain region
 1716 only. At longer time bin widths, we detect fewer communities, and those communities tend
 1717 to contain cells from multiple brain regions. When we examine the distance between (or
 1718 similarity between) the anatomical division of the cells, and the detected communities we
 1719 notice that the two clusterings are more similar at shorter time bin widths (see figure 3.14).

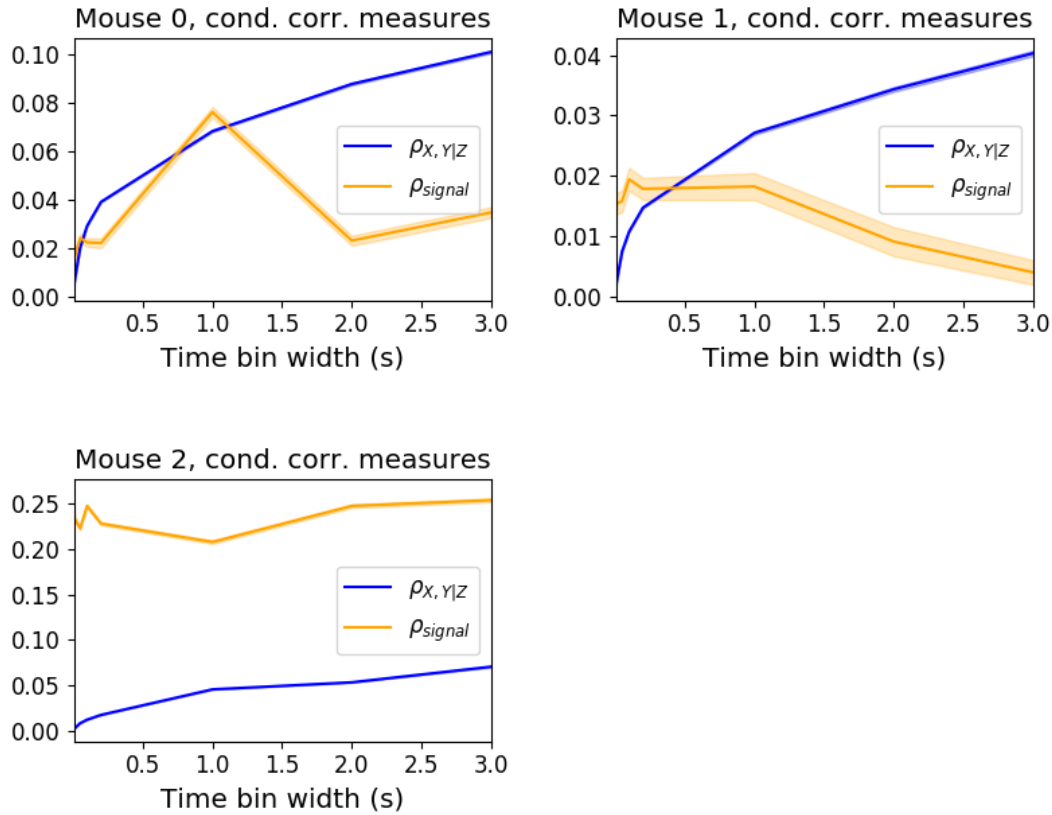


FIGURE 3.12: Comparing the components of the total covariance across different values for the time bin width. We saw a consistent increase in $\rho_{X,Y|Z}$ as the time bin width increased in all three subjects. But we saw different trends in ρ_{signal} for each of the subjects.

When we applied the network noise rejection and community detection process to the networks based on the signal correlations ρ_{signal} we found the number of communities we detected reduced with increasing time bin width. But the number of communities detected was less than that for the total correlations or the spike count correlations. The communities detected always tended to contain cells from multiple regions at both short and long timescales (see figures 3.13c and 3.13d). The communities detected bore very little relation to the anatomical division of the cells. The adjusted Rand index between the community clustering and the anatomical ‘clustering’ is close to zero for every time bin width (see figure 3.15b). This indicates that the similarity between the clusterings is close to chance. We did observe a slight downward trend in the variation of information with increasing bin width (see figure 3.15a), but this is more likely due to a decrease in the number of communities detected rather than any relationship with anatomy.

We also observed that the network noise rejection process rejected some of the cells when applied to the network based on the signal correlations. This means that those cells

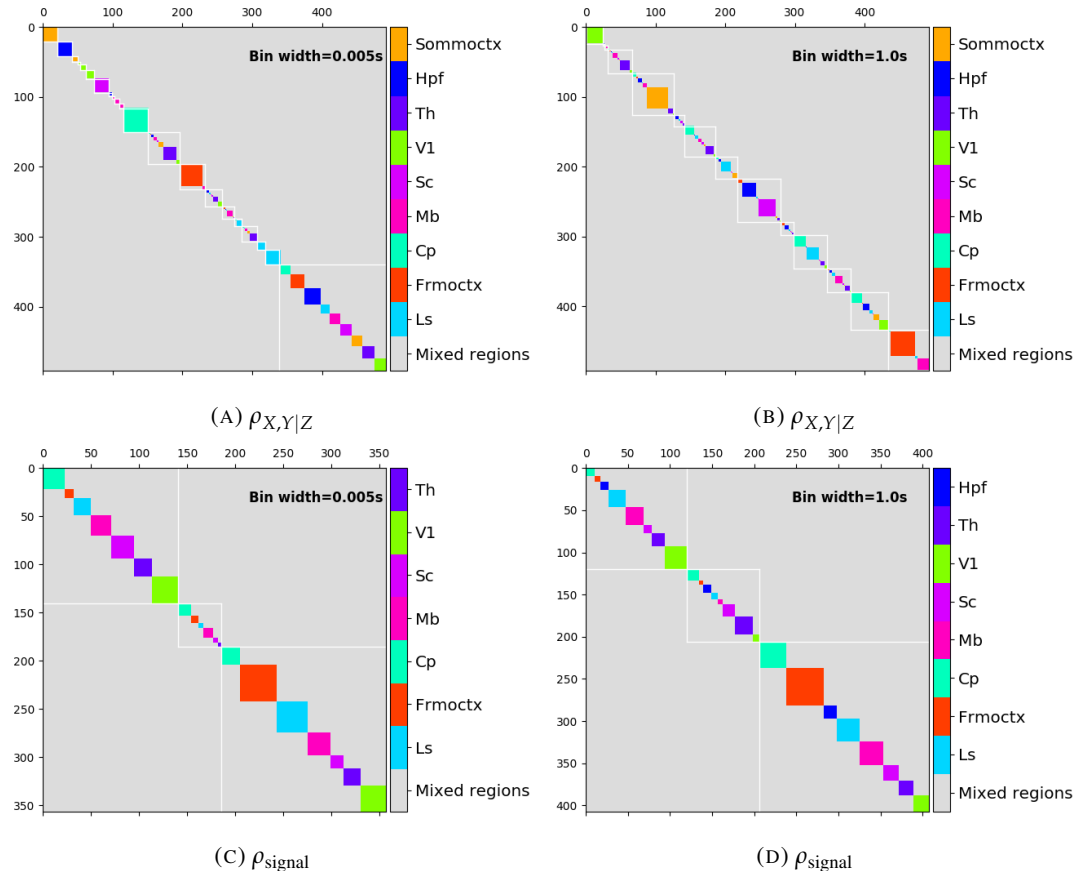


FIGURE 3.13: Matrices showing the regional membership of pairs by colour, and the communities in which those pairs lie. (A-B) Detected communities and regional membership matrix for network based on rectified spike count correlation $\rho_{X,Y|Z}$, using time bin widths of 0.005s and 1s respectively. (C-D) Detected communities and regional membership matrix for network based on rectified signal correlation ρ_{signal} , using time bin widths of 0.005s and 1s respectively.

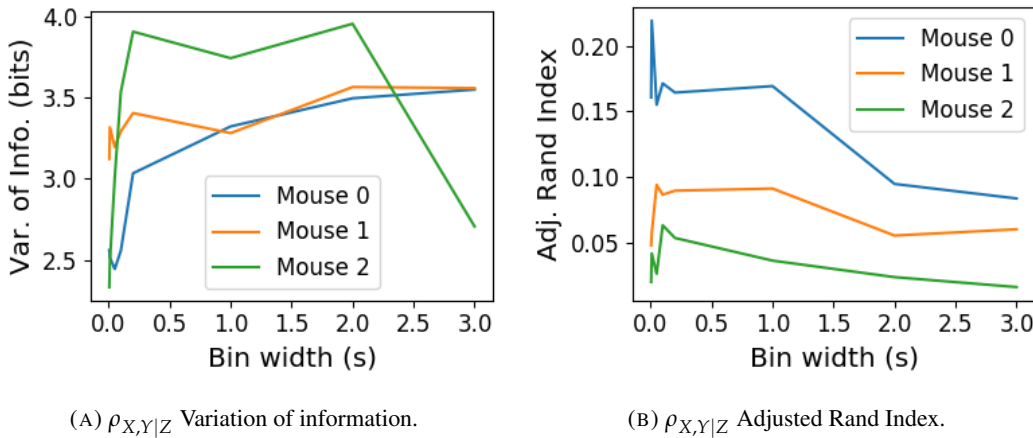
(A) $\rho_{X,Y|Z}$ Variation of information.(B) $\rho_{X,Y|Z}$ Adjusted Rand Index.

FIGURE 3.14: Distance and similarity measures between the anatomical division of the neurons, and the communities detected in the network based on the spike count correlations $\rho_{X,Y|Z}$. (A) The variation of information is a ‘distance’ measure between clusterings. The distance between the anatomical ‘clustering’ and the community clustering increases as the time bin width increases. (B) The adjusted Rand index is a similarity measure between clusterings. The detected communities become less similar to the anatomical division of the cells as the time bin width increases.

1734 did not contribute to the additional structure of the network beyond that captured by the
 1735 sparse weighted configuration model. This is why the matrices in figures 3.13c and 3.13d are
 1736 smaller than their analogues in figures 3.13a and 3.13b.

1737 3.4.8 Absolute correlations and negative rectified correlations

1738 At the moment, the network noise rejection protocol can only be applied to weighted undi-
 1739 rected graphs with non-negative weights. This meant that we had to rectify our correlated
 1740 networks before applying the network noise rejection and community detection process. We
 1741 wanted to investigate what would happen if instead of rectifying the correlations, we used the
 1742 absolute value, or reversed the signs of the correlations and then rectified.

1743 When we used the absolute value of the correlations, we found very similar results to
 1744 those shown above for the rectified total correlations and the rectified spike count corre-
 1745 lations. We detected more communities using shorter bin widths, and these communities
 1746 were more similar to the brain’s anatomy than those communities detected using a longer bin
 1747 width (see figure 3.16). The only exception being that we detected more communities. This
 1748 could indicate that we detected both positively and negatively correlated communities, but
 1749 we haven’t done any further investigation so we cannot say for sure.

1750 When we used the sign reversed rectified correlated networks, we tended to find fewer
 1751 communities. Each community contained cells from many different anatomical regions, at

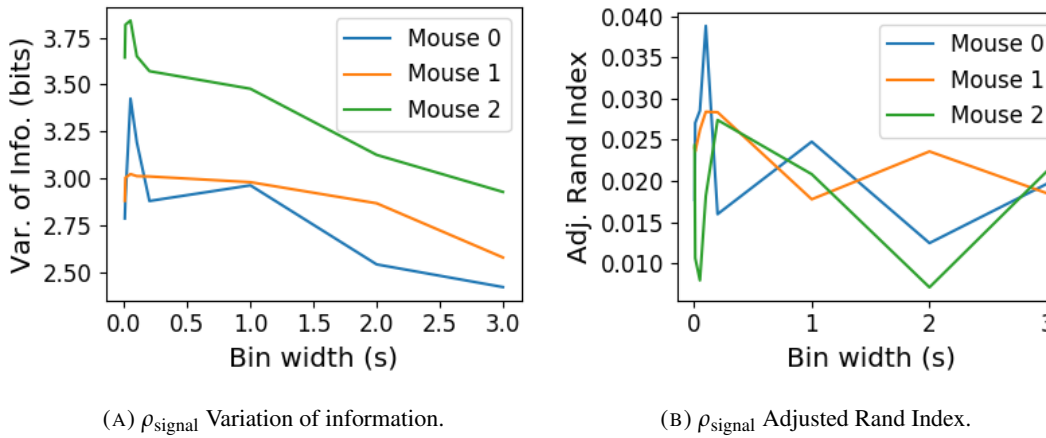
(A) ρ_{signal} Variation of information.(B) ρ_{signal} Adjusted Rand Index.

FIGURE 3.15: Distance and similarity measures between the anatomical division of the neurons, and the communities detected in the network based on the signal correlations ρ_{signal} . (A) The variation of information is a ‘distance’ measure between clusterings. The distance between the anatomical ‘clustering’ and the community clustering increases as the time bin width increases. (B) The adjusted Rand index is a similarity measure between clusterings. The detected communities become less similar to the anatomical division of the cells as the time bin width increases.

1752 both long and short bin widths (see figures 3.17a, 3.17b, 3.17c, 3.17d). The communities
 1753 bore little relation to the anatomical distribution of the cells, this can be seen in figure 3.17f,
 1754 the values close to zero indicate that the similarity between the two clusterings are around
 1755 chance level. This indicates that there was not much structure in the negatively correlated
 1756 networks beyond that captured by the sparse weighted configuration model.

1757 3.5 Discussion

1758 It is well established that the brain uses correlated behaviour in neuronal ensembles to repre-
 1759 sent the information taken in through sensation (Cohen and Maunsell, 2009; Litwin-Kumar,
 1760 Chacron, and Doiron, 2012; deCharms and Merzenich, 1996). However, most studies that
 1761 examine the nature of these correlations in-vivo, study an ensemble of cells from only one
 1762 or two brain regions (Cohen and Kohn, 2011; Wierzynski et al., 2009; Patterson et al., 2014;
 1763 Girard, Hupé, and Bullier, 2001). Furthermore, recent results have shown that behaviour can
 1764 drive correlated activity in multiple brain regions, including those not normally associated
 1765 with motor control (Stringer et al., 2019; Gründemann et al., 2019; Allen et al., 2019). In this
 1766 study, we utilised one of the newly recorded large datasets containing electrophysiological
 1767 recordings from multiple brain regions simultaneously. We investigated correlated behaviour
 1768 in these different brain regions and we investigated correlated behaviour between neurons in
 1769 different regions, during spontaneous behaviour.

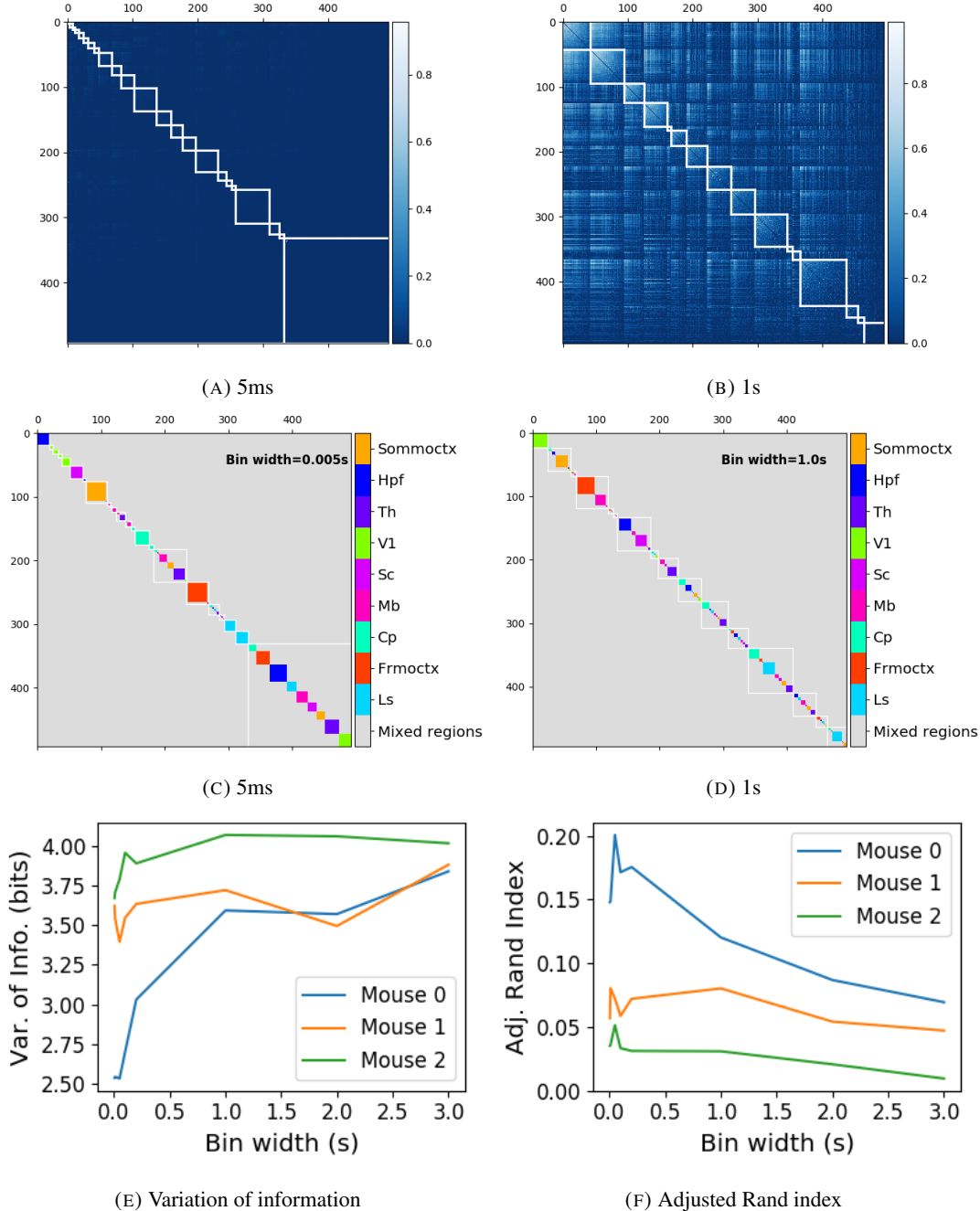


FIGURE 3.16: (A-B) Absolute correlation matrices with detected communities indicated by white lines. These communities are based on the absolute value of the total correlation between each pair of cells. Those entries within a white square indicate that both of those neurons are in the same community. Matrices shown are for 5ms and 1s time bin widths respectively. Main diagonal entries were set to 0. (C-D) Matrices showing the anatomical distribution of pairs along with their community membership. Regional membership is indicated by the colour bar. (E) Variation of information between the anatomical division of the cells, and the detected communities. (F) Adjusted Rand index between the anatomical division, and the detected communities.

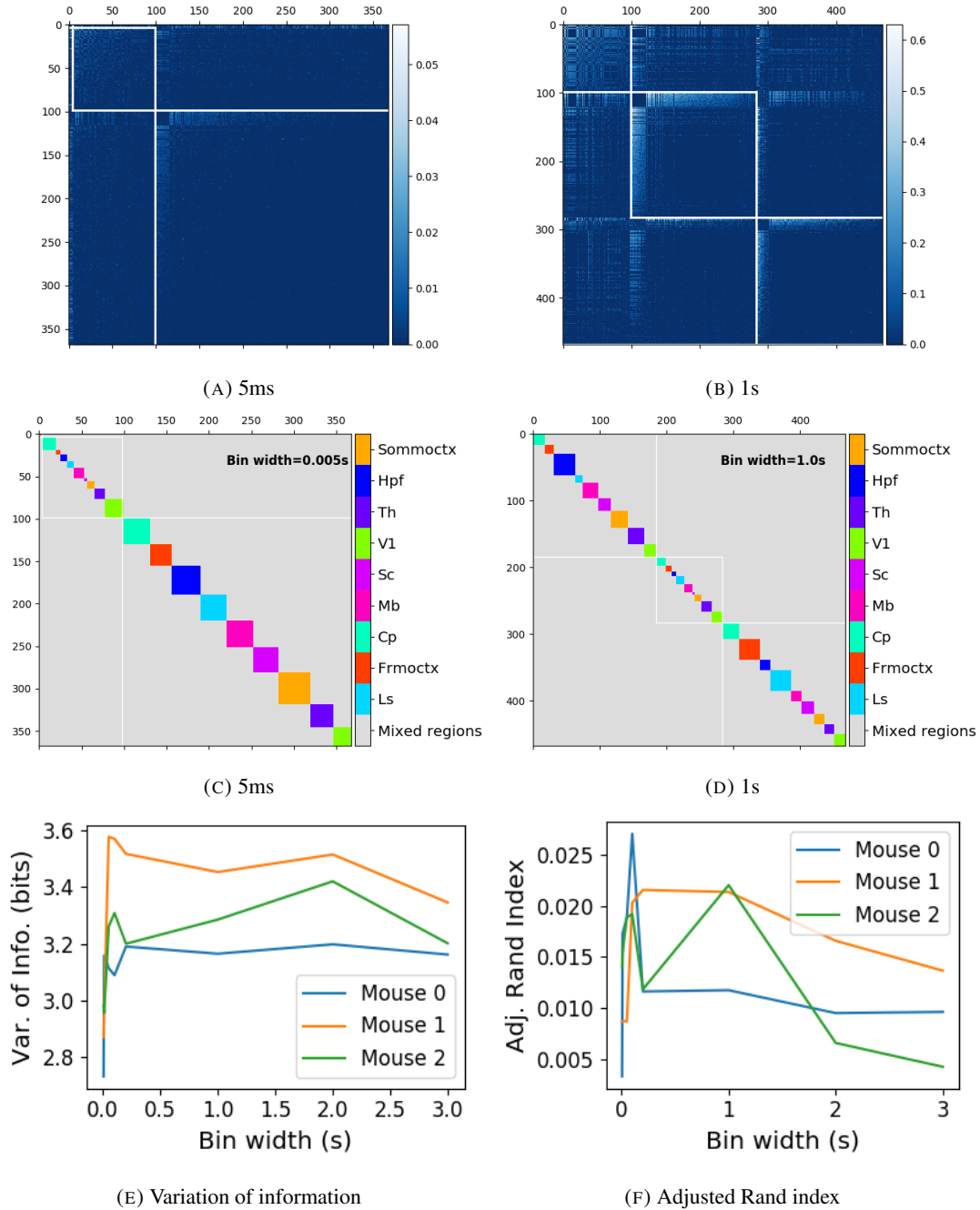


FIGURE 3.17: (A-B) Sign reversed rectified correlation matrices with detected communities indicated by white lines. Those entries within a white square indicate that both of those neurons are in the same community. Matrices shown are for 5ms and 1s time bin widths respectively. Main diagonal entries were set to 0. (C-D) Matrices showing the anatomical distribution of pairs along with their community membership. Regional membership is indicated by the colour bar. (E) Variation of information between the anatomical division of the cells, and the detected communities. (F) Adjusted Rand index between the anatomical division, and the detected communities.

1770 A number of studies have found that the timescale of correlated behaviour induced by a
1771 stimulus can be modulated by the stimulus structure and behavioural context. For example,
1772 the spike train correlations between cells in weakly electric fish are modulated by the spa-
1773 tial extent of the stimulus (Litwin-Kumar, Chacron, and Doiron, 2012), and neurons in the
1774 marmoset primary auditory cortex modulate their spike timing (and therefore correlation) in
1775 response to stimulus features without modulating their firing rate (deCharms and Merzenich,
1776 1996). Furthermore, the width of the time bins over which spike counts are measured has
1777 been shown to have an effect on the magnitude of those correlations (Cohen and Kohn, 2011).
1778 Despite this, very little research has been done comparing correlation measures from the same
1779 dataset at different timescales. We investigated this by varying the time bin width used to bin
1780 spike times into spike counts from as short as 5ms up to 3s.

1781 In order to further investigate the effect of these correlations at different timescales, we
1782 regarded our neuronal ensemble as a weighted undirected graph, where each neuron is rep-
1783 resented by a node, and the weight on each edge is the correlation between the neurons
1784 connected by that edge. We then applied a novel clustering method from network science
1785 (Humphries et al., 2019) to identify communities in these networks. Communities in a net-
1786 work graph refer to sets of nodes that are more strongly connected to each other than the
1787 nodes outside of their set. Another way to put this is to say that the nodes in a community
1788 are more strongly connected than *expected*. What connection strength might be expected is
1789 defined by a null network model. We chose a null network model that matched the sparsity
1790 and total strength of our correlation based data networks. So, if two cells were in the same
1791 community, those cells were more correlated than would be expected given the correlation
1792 strength of their ensemble.

1793 These networks, and the community detection process, were completely agnostic of the
1794 anatomical division of the cells in our ensemble. When we compared the detected commu-
1795 nities with the anatomical division of the cells using distance and similarity measures for
1796 clusterings, we found that the detected communities were more similar to the anatomical
1797 division at shorter timescales. That is, when we used a wider time bin to count spikes, and
1798 computed pairwise correlations with these spike counts, the correlated communities tended to
1799 exist within anatomical regions at shorter timescales, and tended to span anatomical regions
1800 at longer timescales. This could reflect localised functional correlations at short time scales
1801 rippling outwards across brain regions at longer timescales. The brain may be processing
1802 some information quickly locally, and carrying out further, perhaps more detailed, represen-
1803 tation over a longer timescale across many regions using the representations that were just

1804 built locally.

1805 These changes in communities across timescales could also be driven by the anatomy
1806 of the individual cells. For example, it may simply take longer to transmit action potentials
1807 over longer distances, hence correlated activity over longer timescales will exist between
1808 anatomical regions, rather than within. However, the switch to almost exclusively multi-
1809 regional functional networks at 1s bin widths, rather than a mixture of multi-region, and
1810 single-region suggests that the inter-regional correlations either overpower, or inhibit the
1811 local correlations. So there may be more at play than just timescales.

1812 We acknowledged that the region spanning correlated communities that we detected at
1813 longer time scales could exist due to collating activity driven by distinct spontaneous activi-
1814 ties. In order to account for this, we modelled the spike counts as a linear function of the
1815 top 500 principal components of a video of the mouse’s face filmed simultaneously with the
1816 electrophysiological readings. We applied our network noise rejection and community de-
1817 tection process to the weighted undirected networks formed by the spike count correlations
1818 (or noise correlations) and the signal correlations that we calculated using our model. For the
1819 spike count correlation networks, we found much the same results as for the total correlations
1820 as described above. For the signal correlations, the communities detected in these networks
1821 bore little relation to the anatomical division of the cells. Recent findings have shown that
1822 behavioural data accounts for correlations in many brain regions that would otherwise be
1823 dismissed as noise (Stringer et al., 2019), our finding to shows that these correlations are still
1824 governed by the timescale division between local communication and across-region commu-
1825 nication.

1826 There is a lot of room for further investigation based on this research. For a start, the
1827 data that we used here were collected from nine different regions in the mouse brain, but
1828 none of these regions were part of the somatosensory cortex. Given that a mouse experiences
1829 so much of its environment through its sense of smell, some data from this region would be
1830 interesting to investigate. On the same theme, the mice in the experiment from which the
1831 data were collected were headfixed and placed on a rotating ball, but were otherwise behav-
1832 ing spontaneously. Had these mice been exposed to a visual, aural, or olfactory stimulus,
1833 we could have examined the responses of the cells in the brain regions corresponding to vi-
1834 sion, hearing, and olfaction, and compared these responses to the responses from the other
1835 brain regions. Furthermore, we could have investigated the interaction between the sets of
1836 responses.

1837 Another space for further investigation is the community detection. The algorithm that we

1838 used here never detects overlapping communities. But functional communities could indeed
1839 have overlaps. Clustering methods that detect overlapping clusters do exist (Baadel, Thabtah,
1840 and Lu, 2016). Applying one of those algorithms could yield some interesting results. Also,
1841 the community detection algorithm that we used here cannot process graphs with negative
1842 weights, this forced us to separate positive and negative correlations before applying our
1843 network noise rejection and community detections process, or use the absolute value of our
1844 correlations. A community detection algorithm that can work on weighted undirected graphs
1845 with negative weights could yield some interesting results here.

1846 **Chapter 4**

1847 **A simple two parameter distribution
for modelling neuronal activity and
capturing neuronal association**

1850 *Abstract*

1851 Recent developments in electrophysiological technology have lead to an increase in the size
1852 of electrophysiology datasets. Consequently, there is a requirement for new analysis tech-
1853 niques that can make use of these new datasets, while remaining easy to use in practice. In
1854 this work, we fit some one or two parameter probability distributions to spiking data collected
1855 from a mouse exposed to visual stimuli. We show that the Conway-Maxwell-binomial dis-
1856 tribution is a suitable model for the number of active neurons in a neuronal ensemble at any
1857 given moment. This distribution fits these data better than binomial or beta-binomial distribu-
1858 tions. It also captures the correlated activity in the primary visual cortex induced by stimulus
1859 onset more effectively than simply measuring the correlations, at short timescales (< 10ms).
1860 We also replicate the finding of Churchland et al (2010) relating to stimulus onset quenching
1861 neural variability in cortical areas, and we show a correspondence between this quenching
1862 and changes in one of the parameters of the fitted Conway-Maxwell-binomial distributions.

1863 **4.1 Introduction**

1864 Recent advances in electrophysiological technology, such as ‘Neuropixels’ probes (Jun et al.,
1865 2017) have allowed extracellular voltage measurements to be collected from larger numbers
1866 of cells than traditional methods, in multiple brain regions simultaneously, and routinely.
1867 These larger datasets require innovative methods to extract information from the data in a
1868 reasonable amount of time, ‘reasonable’ being subjective in this case.

1869 Theoretically, all the information at any given moment in an electrophysiological dataset
1870 with n neurons could be captured by calculating the probability distribution for every possi-
1871 ble spiking pattern. This would require defining a random variable with 2^n possible values, a
1872 task that quickly becomes impossible as n increases. Attempts at approximating this random
1873 variable often involve measuring pairwise or higher order correlations (Schneidman et al.,
1874 2006; Flach, 2013; Ganmor, Segev, and Schneidman, 2011). But pairwise correlations may
1875 not be enough to characterise instantaneous neural activity (Tkačik et al., 2014). Further-
1876 more, these kinds of models tend to ignore the temporal structure of neuronal data, in favour
1877 of smaller model size, and scalability.

1878 Higher order correlations would be helpful here, but defining these correlations can be
1879 tricky, never-mind quantifying them. If we use the interaction parameters arising from the
1880 exponential family model as measures of higher order correlations, measuring these correla-
1881 tions becomes computationally impractical quite quickly also (the number of ‘three neuron
1882 correlations’ to measure scales with $\binom{n}{3}$). In this paper, we dispense with measuring correla-
1883 tions directly, and attempt to characterise correlated behaviour by measuring ‘association’; a
1884 more general concept that includes correlation.

1885 In this work, we examined the ability of simple distributions to model the number of
1886 active (spiking) neurons in a neuronal ensemble at any given timepoint. We compared a
1887 little-known distribution named the Conway-Maxwell-binomial distribution to the binomial
1888 distribution and the beta-binomial distribution. The binomial distribution is a probability dis-
1889 tribution over the number of successes in a sequence of independent and identical Bernoulli
1890 trials. The beta-binomial distribution is similar, but allows for a bit more flexibility while still
1891 being a model for heterogeneity. Similar to the binomial and beta-binomial, the Conway-
1892 Maxwell-binomial distribution is a probability distribution over the number of successes in a
1893 series of Bernoulli trials, but allows over- and under-dispersion relative to the binomial dis-
1894 tribution. This distribution should therefore be a good candidate for our purposes. We found
1895 that Conway-Maxwell-binomial distribution was usually the best candidate of the three that

1896 we examined.

1897 We also observed some interesting changes in the number of active neurons in the primary
1898 visual cortex and hippocampus at stimulus onset and some changes in this activity in the
1899 thalamus which were sustained for the full duration of the stimulus presentation. This let us
1900 know that there were some responses to model.

1901 We found that fitting a Conway-Maxwell-binomial distribution was a better method of
1902 capturing association between neurons than measuring the spike count correlation for the
1903 short time bins that we used (< 10ms).

1904 Finally, we also wanted to investigate parallels between the parameters of the Conway-
1905 Maxwell-binomial distribution and quantities that have been established as relevant to sen-
1906 sory processing. So, we replicated the findings made by Churchland et al. (2010) relating
1907 to a reduction in neural variability at stimulus onset in the macaque cortical regions, but for
1908 data taken from the mouse primary visual cortex. We compared these findings to the values
1909 of the fitted Conway-Maxwell-binomial distribution parameters.

1910 4.2 Data

1911 We used data collected by Nick Steinmetz and his lab ‘CortexLab at UCL’ (Steinmetz, Caran-
1912 dini, and Harris, 2019). The data can be found online ¹ and are free to use for research
1913 purposes.

1914 Two ‘Phase3’ Neuropixels (Jun et al., 2017) electrode arrays were inserted into the brain
1915 of an awake, head-fixed mouse for about an hour and a half. These electrode arrays recorded
1916 384 channels of neural data each at 30kHz and less than $7\mu\text{V}$ RMS noise levels. The sites
1917 are densely spaced in a ‘continuous tetrode’-like arrangement, and a whole array records
1918 from a 3.8mm span of the brain. One array recorded from visual cortex, hippocampus, and
1919 thalamus, the other array recorded from motor cortex and striatum. The data were spike-
1920 sorted automatically by Kilosort and manually by Nick Steinmetz using Phy. In total 831
1921 well-isolated individual neurons were identified.

1922 4.2.1 Experimental protocol

1923 The mouse was shown a visual stimulus on three monitors placed around the mouse at right
1924 angles to each other, covering about ± 135 degrees azimuth and ± 35 degrees elevation.

¹<http://data.cortexlab.net/dualPhase3/>

1925 The stimulus consisted of sine-wave modulated full-field drifting gratings of 16 drift di-
1926 rections ($0^\circ, 22.5^\circ, \dots, 337.5^\circ$) with 2Hz temporal frequency and 0.08 cycles/degree spatial
1927 frequency displayed for 2 seconds plus a blank condition. Each of these 17 conditions were
1928 presented 10 times in a random order across 170 different trials. There were therefore 160
1929 trials with a drifting-grating visual stimulus present, and 10 trials with a blank stimulus.

1930 **4.3 Methods**

1931 **4.3.1 Binning data**

1932 We converted the spike times for each cell into spike counts by putting the spike times into
1933 time bins of a given ‘width’ (in milliseconds). We used time bins of 1ms, 5ms, and 10ms.
1934 We used different time bin widths to assess the impact of choosing a bin width.

1935 **4.3.2 Number of *active* neurons**

1936 To count the number of active neurons in each neuronal ensemble, we split the time interval
1937 for each trial into bins of a given width. We counted the number of spikes fired by each cell
1938 in each bin. If a cell fired *at least* one spike in a given bin, we regarded that cell as active in
1939 that bin. We recorded the number of active cells in every bin, and for the purposes of further
1940 analysis, we recorded each cell’s individual spike counts.

1941 It should be noted that when we used a bin width of 1ms, the maximum number of
1942 spikes in any bin was 1. For the wider time bins, some bins had spike counts greater than
1943 1. Consequently when using a bin width of 1ms, the number of active neurons and the total
1944 spike count of a given bin were identical. But for wider bin widths, the total spike count was
1945 greater than the number of active neurons.

1946 So for the 1ms bin width, the activity of a neuron and the number of spikes fired by that
1947 neuron in any bin can be modelled as a Bernoulli variable. But for wider time bins, only the
1948 activity can be modelled in this way.

1949 **4.3.3 Moving windows for measurements**

1950 When taking measurements (e.g. moving average over the number of active neurons) or
1951 fitting distributions (eg. the beta binomial distribution) we slid a window containing a certain
1952 number of bins across the data, and made our measurements at each window position. For
1953 example, when analysing 1ms bin data, we used a window containing 100 bins, and we slid

Bin width (ms)	Window size (bins)	Window size (ms)	Windows per trial
1ms	100	100ms	296
5ms	40	200ms	286
10ms	40	400ms	266

TABLE 4.1: Details of the different bin width and analysis window sizes used when binning spike times, and analysing those data.

1954 the window across the time interval for each trial moving 10 bins at a time. So that for
 1955 3060ms of data, we made 296 measurements.

1956 For the 5ms bin width data, we used windows containing 40 bins, and slid the window 2
 1957 bins at a time when taking measurements.

1958 For the 10ms bin width data, we used windows containing 40 bins, and slid the window
 1959 1 bin at a time when taking measurements (see table 4.1 for concise details).

1960 By continuing to use windows containing 40 bins, we retained statistical power but sac-
 1961 rificed the number of measurements taken.

1962 There was an interval between each trial with a grey image in place of the moving of
 1963 the moving bar stimulus. This interval varied in time. But we included some of this interval
 1964 when recording the data for each trial. We started recording the number of active neurons,
 1965 and the number of spikes from each neuron from 530ms before each trial until 1030ms after
 1966 each trial. This way, we could see the change in our measurements at the onset of a stimulus
 1967 and the end of stimulus presentation.

1968 As mentioned in section 4.3.2, we recorded the number of active neurons in each bin, and
 1969 the spike count for each neuron in each bin. The actual measurements we took using these
 1970 data in each window were as follows:

1971 **Moving average** The average number of active cells in each window.

1972 **Moving variance** The variance of the number of active cells in each window.

1973 **Average correlation** We measured the correlation between the spike counts of each pair of
 1974 cells in the ensemble, and took the average of these measurements.

1975 **Binomial p** We fitted a binomial distribution to the data in each window and recorded the
 1976 fitted probability of success, p in each case.

1977 **Beta-binomial α, β** We fitted a beta-binomial distribution to the data in each window, and
 1978 recorded the values of the fitted shape parameters, α and β , of each distribution.

1979 **Conway-Maxwell-binomial distribution p, ν** We fitted a Conway-Maxwell-binomial dis-
 1980 tribution to the data in each window, and recorded the fitted values of p and ν for each
 1981 distribution.

1982 **Log-likelihoods** We also recorded the log-likelihood of each of the fitted distributions for
 1983 each window.

1984 **4.3.4 Fano factor**

The *Fano factor* of a random variable is defined as the ratio of the variable's variance to its mean.

$$F = \frac{\sigma^2}{\mu} \quad (4.1)$$

1985 We measured the Fano factor of the spike count of a given cell by measuring the mean and
 1986 variance of the spike count across trials, and taking the ratio of those two quantities. When
 1987 calculated in this way the Fano factor can be used as a measure of neural variability that
 1988 controls for changes in the firing rate. This is similar to the calculation used in (Churchland
 1989 et al., 2010).

1990 **4.3.5 Probability Distributions suitable for modelling ensemble activity**

1991 We present here three different probability distributions that could be suitable to model the
 1992 number of active neurons in an ensemble. Each distribution has the set $\{0, \dots, n\}$ as its sup-
 1993 port, where n is the number of neurons in the ensemble. These are simple distributions with
 1994 either two or three parameters each. However, we regard n as known when using these dis-
 1995 tributions for modelling, so in effect each distribution has either one or two free parameters.

1996 **Association**

1997 *Association* between random variables is similar to the correlation between random variables
 1998 but is more general in concept. The correlation is a measure of association; and association
 1999 doesn't have a mathematical definition like correlation does. Essentially, the association
 2000 between two random variables is their tendency to take the same or similar values. Positively
 2001 associated variables tend to take the same value, and negatively associated variables tend to
 2002 take different values. In this research, we work with probability distributions of the number of
 2003 successes in a set of Bernoulli trials. These Bernoulli variables may or may not be associated.

2004 A probability distribution over the number of successes in n Bernoulli trials, where the
 2005 Bernoulli variables may be associated, could constitute a good model for the number of active
 2006 neurons in an ensemble of n neurons.

2007 **Binomial distribution**

The binomial distribution is a two parameter discrete probability distribution that can be thought of as a probability distribution the number of successes from n independent Bernoulli trials, each with the same probability of success. The parameters of the binomial distribution are n the number of trials, and $0 \leq p \leq 1$, the probability of success for each of these trials. A random variable with the binomial distribution can take values from $\{0, \dots, n\}$. The probability mass function of the distribution is

$$P(k; n, p) = \binom{n}{k} p^k (1-p)^{n-k} \quad (4.2)$$

2008 As a model for the activity of a neuronal ensemble, the main problem with the binomial
 2009 distribution is that it treats each neuron, represented as a Bernoulli trial, as independent. It is
 2010 well known that neurons are not independent, and that correlated behaviour between neurons
 2011 is vital for representing sensory information (Cohen and Maunsell, 2009). The binomial dis-
 2012 tribution falls short in this regard, but it is useful as performance benchmark when assessing
 2013 the performance of other models.

2014 **Beta-binomial distribution**

2015 The beta distribution is the conjugate distribution of the binomial distribution. The beta-
 2016 binomial distribution is the combination of the beta distribution and the binomial distribution,
 2017 in that the probability of success for the binomial distribution is sampled from the beta dis-
 2018 tribution. This allows the beta-binomial distribution to capture some over dispersion relative
 2019 to the binomial distribution.

The beta-binomial distribution is a three parameter distribution, n the number of Bernoulli trials, and $\alpha \in \mathbb{R}_{>0}$ and $\beta \in \mathbb{R}_{>0}$ the shape parameters of the beta distribution. The probability mass function for the beta-binomial distribution is

$$P(k; n, \alpha, \beta) = \binom{n}{k} \frac{B(k + \alpha, n - k + \beta)}{B(\alpha, \beta)} \quad (4.3)$$

2020 where $B(\alpha, \beta)$ is the beta function.

This probability distribution can be reparametrised in a number of ways. One of which defines new parameters π and ρ by

$$\pi = \frac{\alpha}{\alpha + \beta} \quad (4.4)$$

$$\rho = \frac{1}{\alpha + \beta + 1} \quad (4.5)$$

2021 This reparametrisation is useful because π acts as a location parameter analogous to the p
 2022 parameter of a binomial distribution. A value of $\rho > 0$ indicates over-dispersion relative to a
 2023 binomial distribution.

2024 As a model for the activity of a neuronal ensemble, the beta-binomial distribution is
 2025 more suitable than a binomial distribution because the over-dispersion of the beta-binomial
 2026 distribution can be used to model positive association between the neurons. An extreme
 2027 example of this over-dispersion/positive association can be seen in figure 4.1b. In this figure,
 2028 the neurons are positively associated and so tend to take the same value, consequently the
 2029 probability mass of the beta-binomial distribution builds up close to $k = 0$ and $k = n$. It is
 2030 worth noting that the location parameter for each distribution has the same value, $p = \pi =$
 2031 0.5.

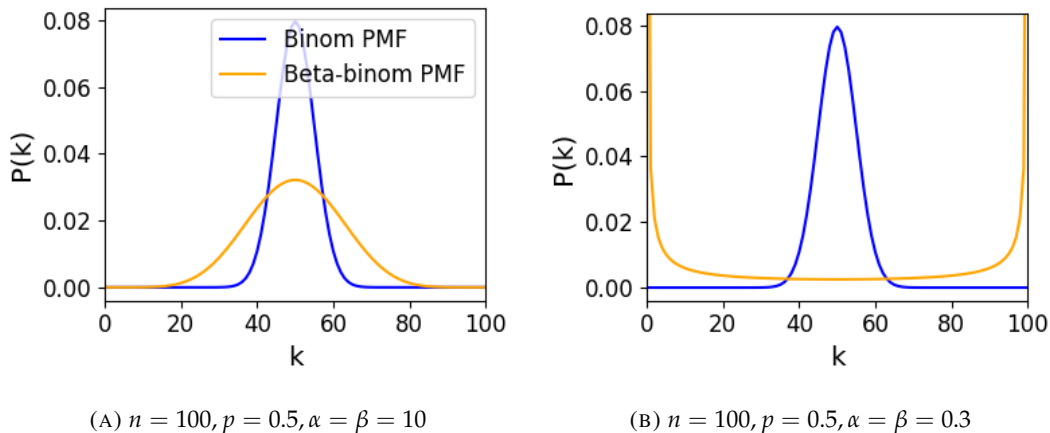
(A) $n = 100, p = 0.5, \alpha = \beta = 10$ (B) $n = 100, p = 0.5, \alpha = \beta = 0.3$

FIGURE 4.1: Figures showing the over-dispersion possible for a beta-binomial distribution relative to a binomial distribution. Parameters are shown in the captions.

2032 Conway-Maxwell-binomial distribution

2033 The Conway-Maxwell-binomial distribution (COMb distribution) is a three parameter generalisation of the binomial distribution that allows for over dispersion and under dispersion

relative to the binomial distribution. The parameters of the distribution are n the number of Bernoulli trials, and two shape parameters $0 \leq p \leq 1$, and $\nu \in \mathbb{R}$.

The probability mass function of the COMb distribution is

$$P(k; n, p, \nu) = \frac{1}{S(n, p, \nu)} \binom{n}{k}^{\nu} p^k (1-p)^{n-k} \quad (4.6)$$

where

$$S(n, p, \nu) = \sum_{j=0}^n \binom{n}{j}^{\nu} p^j (1-p)^{n-j} \quad (4.7)$$

The only difference between this PMF and the PMF for the standard binomial is the introduction of ν and the consequent introduction of the normalising function $S(n, p, \nu)$.

Indeed, if $\nu = 1$ the COMb distribution is identical to the binomial distribution with the same values for n and p . We can see in figure 4.2d that the KL-divergence $D_{KL}(P_{COMb}(n, p, \nu) || P_{Bin}(n, p)) = 0$ along the line where $\nu = 1$. The analytical expression for the divergence is

$$D_{KL}(P_{COMb}(k; n, p, \nu) || P_{Bin}(k; n, p)) = (\nu - 1) E_{P_{COMb}(k; n, p, \nu)} \left[\log \binom{n}{k} \right] \quad (4.8)$$

$$- \log S(n, p, \nu) \quad (4.9)$$

At $\nu = 1$, we have $S(n, p, 1)$ which is just the sum over the binomial PMF, so $S(n, p, 1) = 1$ and therefore $D_{KL}(P_{COMb}(n, p, \nu) || P_{Bin}(n, p)) = 0$.

If $\nu < 1$ the COMb distribution will exhibit over-dispersion relative to the binomial distribution. If $p = 0.5$ and $\nu = 0$ the COMb distribution is the discrete uniform distribution, and if $\nu < 0$ the mass of the COMb distribution will tend to build up near $k = 0$ and $k = n$. This over-dispersion represents positive association in the Bernoulli variables. An example of this over-dispersion can be seen in figure 4.2b.

If $\nu > 1$ the COMb distribution will exhibit under-dispersion relative to the binomial distribution. The larger the value of ν the more probability mass will build up at $n/2$ for even n , or at $\lfloor n/2 \rfloor$ and $\lceil n/2 \rceil$ for odd n . This under-dispersion represents negative association in the Bernoulli variables. An example of this under-dispersion can be seen in figure 4.2a.

It should be noted that the p parameter of the COMb distribution does not correspond to the mean of the distribution, as is the case for the binomial p parameter, and beta-binomial π parameter. That is, the COMb p parameter is not a location parameter. An illustration of this can be seen in figure 4.2c. This is because an interaction between the p and ν parameters skews the mean. There is no analytical expression for the mean of the COMb distribution.

ν	Relative dispersion	Association between neurons/variables
< 1	over	positive
1	none	none
> 1	under	negative

TABLE 4.2: Relative dispersion of the COMb distribution, and association between Bernoulli variables as represented by the value of the ν parameter.

2055 Since the COMb distribution has the potential to capture positive and negative associa-
 2056 tions between the neurons/Bernoulli variables, it should be an excellent candidate for mod-
 2057 elling the number of active neurons in a neuronal ensemble.

2058 We wrote a dedicated Python package to enable easy creation and fitting of COMb dis-
 2059 tribution objects. The format of the package imitates the format of other distribution objects
 2060 from the `scipy.stats` Python package. The COMb package can be found here:
 2061 https://github.com/thomasjdelaney/Conway_Maxwell_Binomial_Distribution

2062 4.3.6 Fitting

2063 We fitted binomial, beta-binomial, and Conway-Maxwell-binomial (COMb) distributions to
 2064 the neural activity in each of the overlapping windows covering each trial. To fit the distribu-
 2065 tions we minimised the appropriate negative log likelihood function using the data from the
 2066 window.

There is an analytical solution for maximum likelihood estimate of the binomial distribution's p parameter.

$$\hat{p} = \frac{1}{n} \sum_{i=1}^N k_i \quad (4.10)$$

2067 We minimised the negative log likelihood function of the beta-binomial distribution nu-
 2068 merically. We calculated the negative log likelihood for a sample directly, by taking the sum
 2069 of the log of the probability mass function for each value in the sample. We minimised the
 2070 negation of that function using the `minimise` function of the `scipy.optimize` Python
 2071 package.

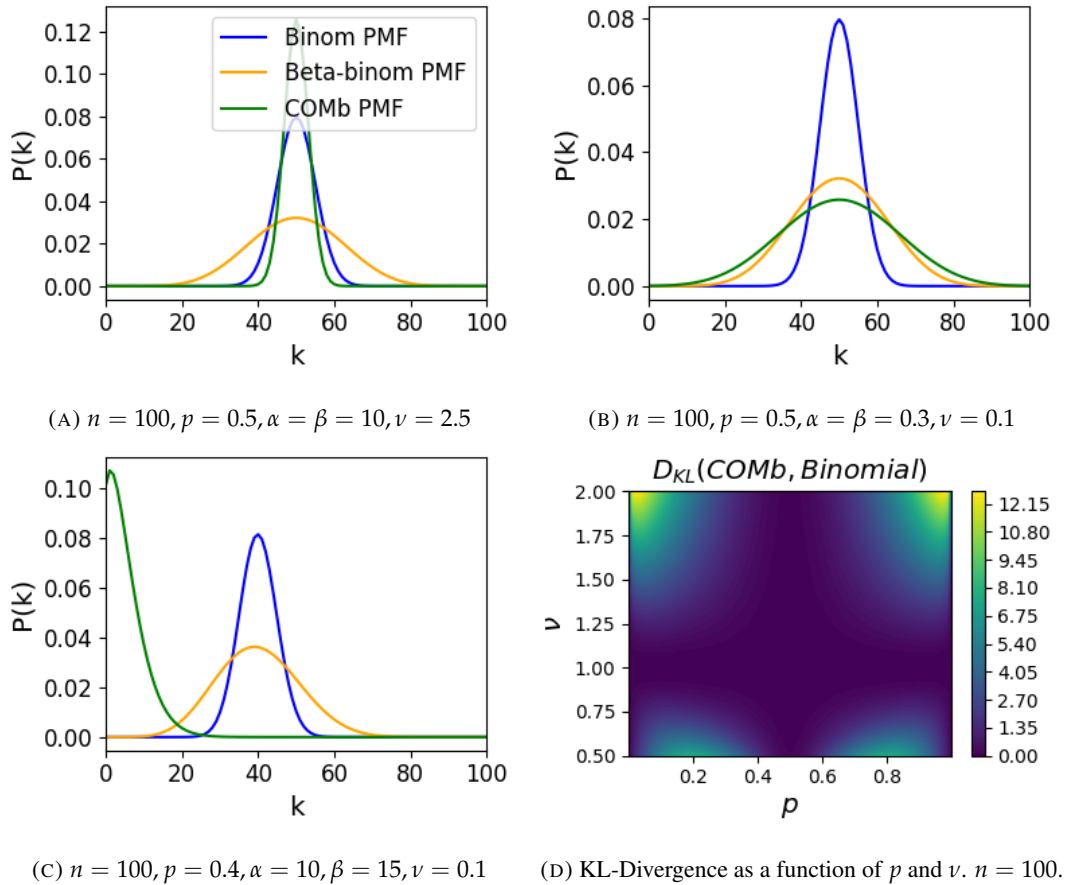


FIGURE 4.2: Figures showing (A) the under-dispersion and (B) over-dispersion permitted by the COMb distribution relative to a binomial distribution. (C) illustrates that the p parameter of the COMb distribution does not correspond to the mean of the distribution, as it does for the binomial and beta-binomial distributions. (D) shows a heatmap for the value of the Kullback-Liebler divergence between the COMb distribution and the standard binomial distribution with same value for n , as a function of p and ν . $n = 100$.

Parameters are shown in the captions.

The log likelihood function of the COMb distribution given some sample $\{k_1, \dots, k_N\}$ is

$$\ell(p, \nu | k_1, \dots, k_N) = N [n \log(1 - p) - \log S(n, p, \nu)] \quad (4.11)$$

$$+ \log \frac{p}{1 - p} \sum_{i=1}^N k_i \quad (4.12)$$

$$+ \nu \sum_{i=1}^N \log \binom{n}{k_i} \quad (4.13)$$

2072 We minimised the negation of this function using numerical methods. More specifically, we
2073 used the `minimise` function of the `scipy.optimize` Python package.

2074 **4.3.7 Goodness-of-fit**

2075 After fitting, we measured the goodness-of-fit of each model/distribution with their log like-
2076 lihood. We calculated this directly using the `logpmf` functions of the distribution objects in
2077 Python.

2078 **4.4 Results**

2079 We defined a neuron as *active* in a time bin if it fires at least one spike during the time interval
2080 covered by that bin. We measured the number of active neurons in the primary visual cortex
2081 of a mouse in 1ms bins across 160 trials of a moving bar visual stimulus. We then slid a
2082 100ms window across these 1ms bins taking measurements, and fitting distributions along
2083 the way. We did the same for neurons in the thalamus, hippocampus, striatum, and motor
2084 cortex. We repeated the analysis for 5ms time bins with 40 bin windows, and 10ms time bins
2085 with 40 bin windows.

2086 **4.4.1 Increases in mean number of active neurons and variance in number of
2087 active neurons at stimulus onset in some regions**

2088 We measured the average number of active neurons, and the variance of the number of active
2089 neurons in a 100ms sliding window starting 500ms before stimulus onset until 1000ms after
2090 stimulus onset. We found differences in the response across regions. There were no observed
2091 changes in response to the stimulus in the motor cortex or the striatum. The changes in the
2092 other regions are detailed below.

2093 **Primary visual cortex**

2094 We found a transient increase in both the average and variance of the number of active neu-
2095 rons at stimulus onset, followed by a fall to pre-stimulus levels, followed by another transient
2096 increase (see figure 4.3). The oscillation in both of these measurements appear to reflect the
2097 frequency of the stimulus (see Data section 4.2.1), and it is known that stimulus structure can
2098 influence response structure(Litwin-Kumar, Chacron, and Doiron, 2012). We see a similar
2099 but lower amplitude oscillation at the end of the stimulus presentation.

2100 **Hippocampus**

2101 In the hippocampus we observed a transient increase in the average number of active neurons
2102 and in the variance of the number of active neurons at stimulus onset (see figure 4.4). The
2103 increase lasted about 125ms, and the subsequent fall to baseline took the a similar amount of
2104 time.

2105 **Thalamus**

2106 In the thalamus we observed a transient increase in the both the average and variance of
2107 the number of active neurons on stimulus onset, followed by a fall to pre-stimulus levels,
2108 followed by a sustained increase until the stimulus presentation ends.

2109 As one you might expect for a visual stimulus, the change in the average number of active
2110 neurons was greatest in the primary visual cortex. In this region, this quantity doubled on
2111 stimulus onset. In contrast, in the hippocampus and the thalamus, the average number of
2112 active neurons only increased by a fraction of the unstimulated baseline value. The duration
2113 of the response in V1 and the hippocampus at stimulus onset was 300 – 400ms, but the
2114 response in the thalamus appeared to last for the duration of stimulus presentation. The V1
2115 also showed a change in the average number of active neurons at stimulus end. The change
2116 was similar to that observed at stimulus onset, but smaller in magnitude (see figures 4.3, 4.4,
2117 and 4.5)

2118 **4.4.2 Conway-Maxwell-binomial distribution is usually a better fit than bino-
2119 mial or beta-binomial**

2120 Since the Conway-Maxwell-binomial distribution has not been fitted to neuronal data before,
2121 it is not clear that it would be a better fit than the binomial or beta-binomial distributions.
2122 In order to find out which parametric distribution was the best fit for the largest proportion

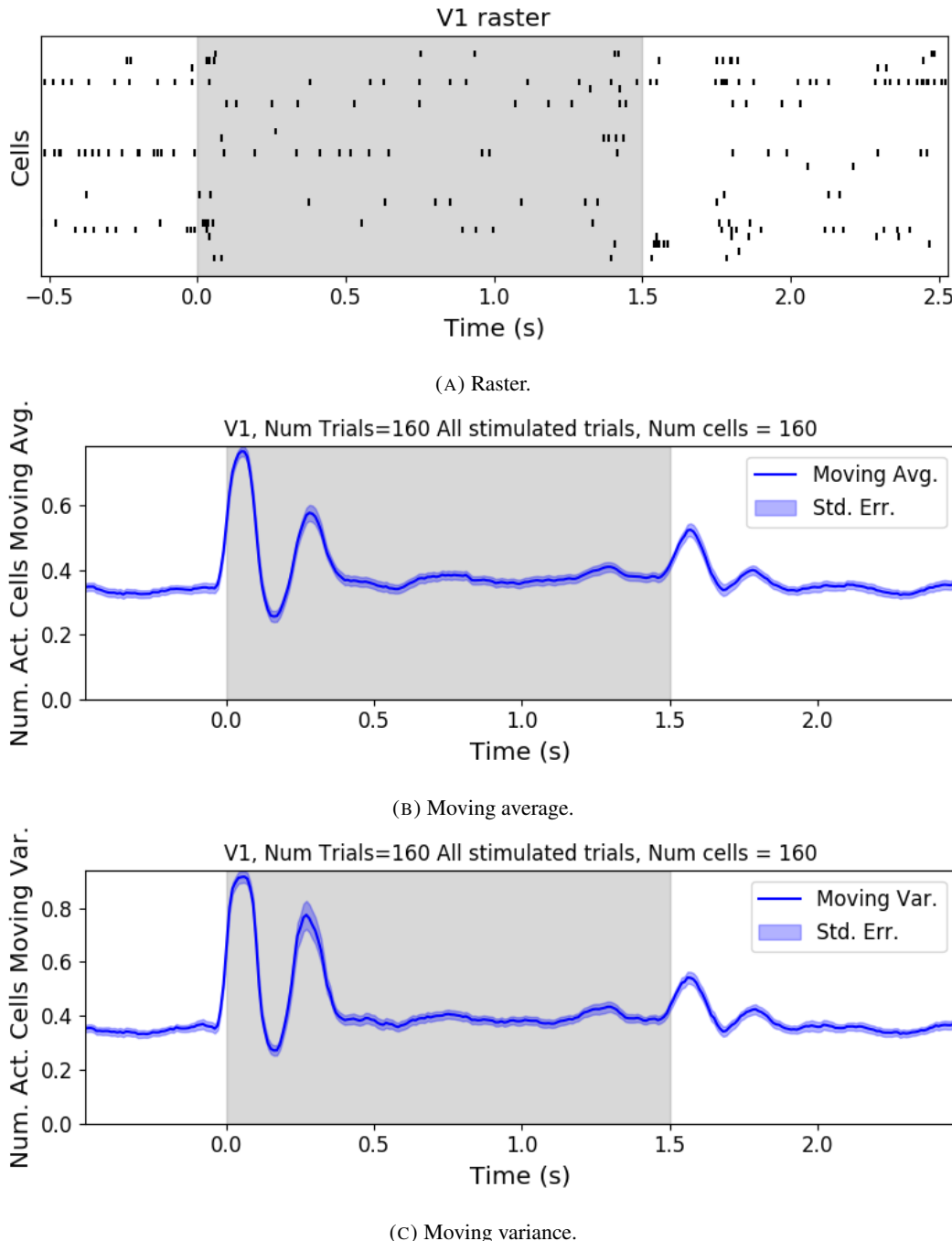


FIGURE 4.3: (A) Raster plot showing the spikes fired by 33 randomly chosen neurons in the primary visual cortex. (B-C) (B) average and (C) variance of the number of active neurons, measured using a sliding window 100ms wide, split into 100 bins. The midpoint of the time interval for each window is used as the timepoint (x-axis point) for the measurements using that window. The grey shaded area indicates the presence of a visual stimulus. The opaque line is an average across the 160 trials that included a visual stimulus of any kind. We can see a transient increase in the average number of active neurons and the variance of this number, followed by a fluctuation and another increase.

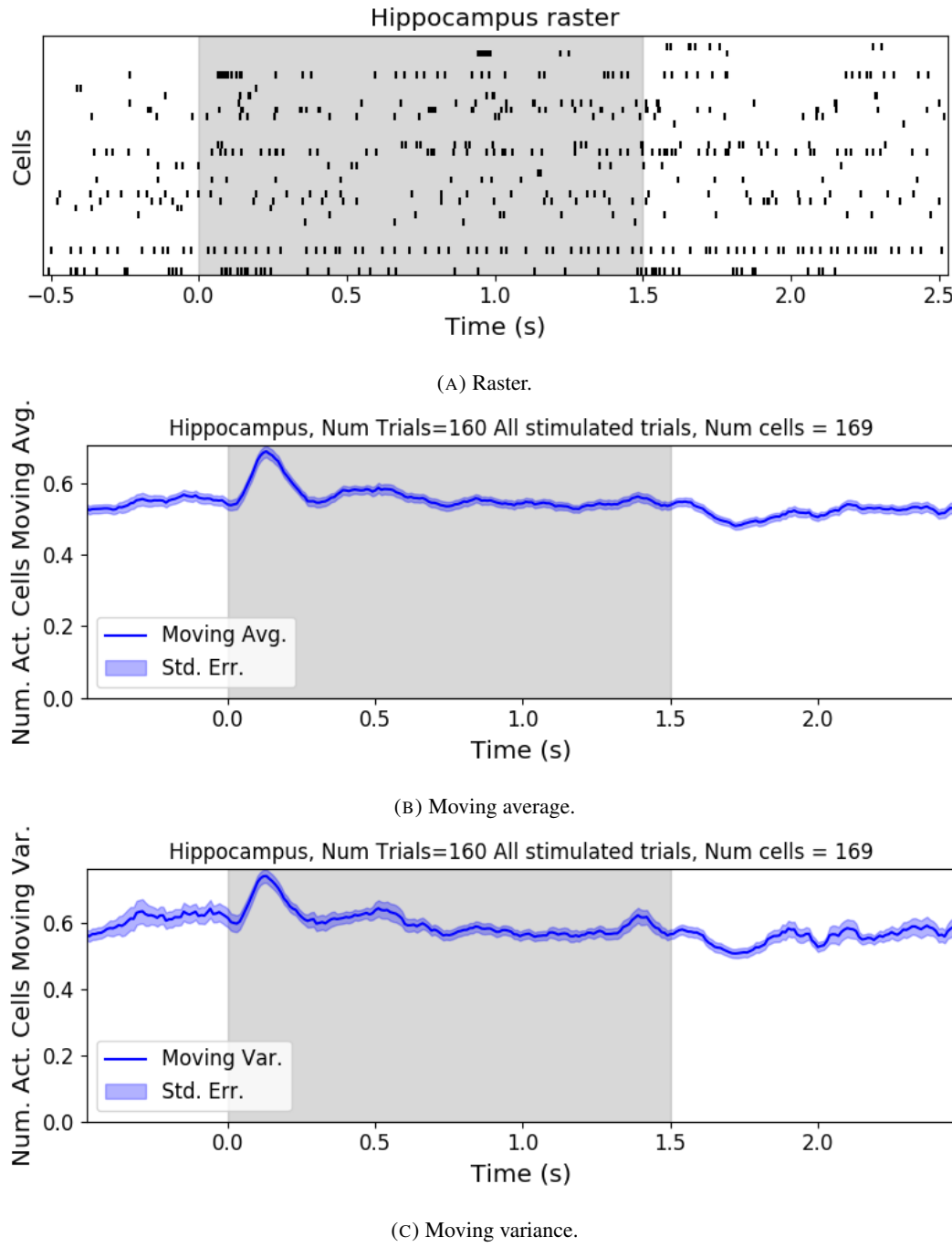


FIGURE 4.4: (A) Raster plot showing the spikes fired by 33 randomly chosen neurons in the hippocampus. (B-C) (B) average and (C) variance of the number of active neurons, measured using a sliding window 100ms wide, split into 100 bins. The midpoint of the time interval for each window is used as the timepoint (x-axis point) for the measurements using that window. The grey shaded area indicates the presence of a visual stimulus. The opaque line is an average across the 160 trials that included a visual stimulus of any kind. We can see a transient increase in the average number of active neurons and the variance of this number at stimulus onset.

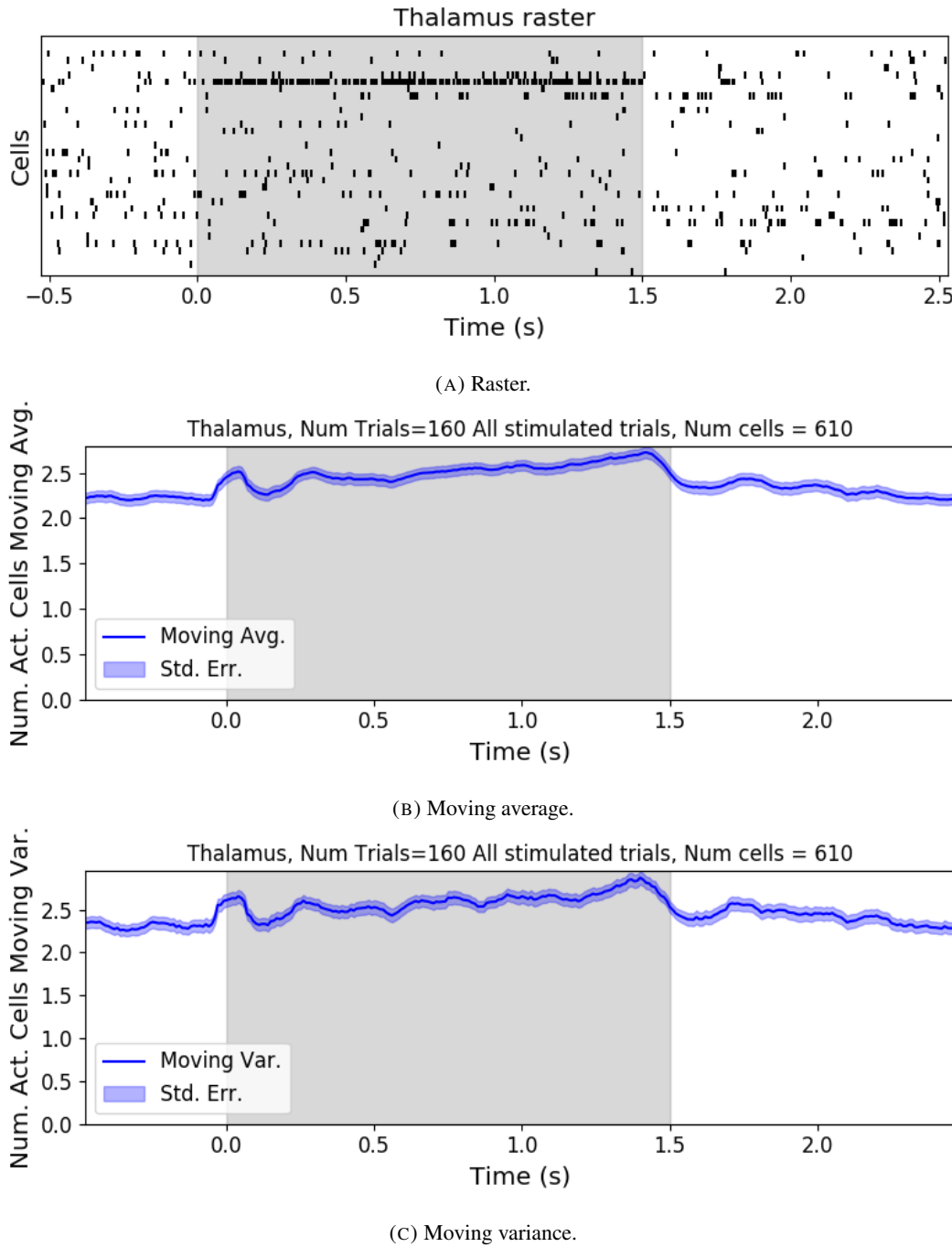
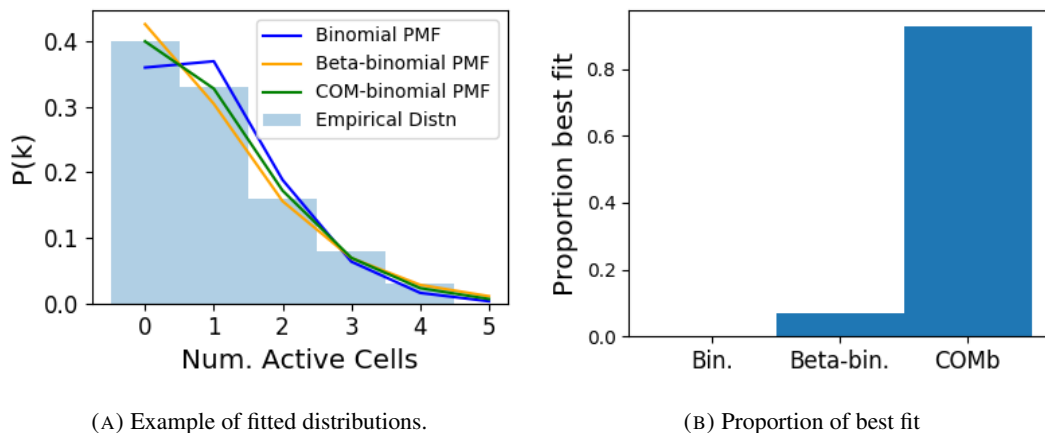


FIGURE 4.5: (A) Raster plot showing the spikes fired by 33 randomly chosen neurons in the thalamus. (B-C) (B) average and (C) variance of the number of active neurons, measured using a sliding window 100ms wide, split into 100 bins. The midpoint of the time interval for each window is used as the timepoint (x-axis point) for the measurements using that window. The grey shaded area indicates the presence of a visual stimulus. The opaque line is an average across the 160 trials that included a visual stimulus of any kind. We can see an immediate increase at stimulus onset, a subsequent fall, and another sustained increase until the stimulus presentation ends.

of our data, we fit a binomial, a beta-binomial, and a Conway-Maxwell-binomial (COMb) distribution to each window for each bin width, and each region. Then we assessed the goodness-of-fit of each distribution by calculating the log-likelihood of each fitted distribution using the associated sample. We measured the proportion of samples for which each distribution was the best fit, for each bin width value and each region.

We found that the COMb distribution was the best fit for most of the samples regardless of bin width or region. The bin width had an effect on the number of samples for which the COMb distribution was the best fit. The results are summarised in table 4.3. For a bin width of 1ms, the COMb distribution was the best fit for over 90% of samples, the beta-binomial distribution was the best fit for less than 10% of samples, and the binomial distribution was the best fit for less than 1% of samples, across regions. For 5ms bins, the COMb distribution was the best fit for 70 – 80% of samples, the beta-binomial distribution was the best fit for 20 – 30% of the samples, and again the binomial distribution was the best fit for less than 1% of samples, across regions. Finally, for 10ms bins, the COMb distribution was the best fit for 53 – 80% of samples, the beta-binomial distribution was the best fit for 20 – 47% of the samples, and the binomial distribution was the best fit for less than 0.1% of samples, across regions.



(A) Example of fitted distributions.

(B) Proportion of best fit

FIGURE 4.6: (A) An example of the binomial, beta-binomial, and Conway-Maxwell-binomial distributions fitted to a sample of neural activity. The Conway-Maxwell-binomial distribution is the best fit in this case. The histogram shows the empirical distribution of the sample. The probability mass function of each distribution is indicated by a different coloured line. (B) Across all samples in all trials, the proportion of samples for which each fitted distribution was the best fit. The Conway-Maxwell-binomial distribution was the best fit for 93% of the samples taken from V1 using a bin width of 1ms.

Bin Width (ms)	Binomial	Beta-binomial	COMb
1ms	< 1%	< 10%	> 90%
5ms	< 0.1%	20 – 30%	70 – 80%
10ms	< 0.1%	20 – 47%	53 – 80%

TABLE 4.3: Proportion of samples for which each distribution was the best fit, grouped by bin width. The COMb distribution is the best fit most of the time.

2140 **4.4.3 Conway-Maxwell-binomial distribution captures changes in association
2141 at stimulus onset**

2142 We fit a Conway-Maxwell-binomial (COMb) distribution to the number of active neurons in
2143 the 1ms time bins in a 100ms sliding window. We also measured the correlation coefficient
2144 between the spike counts of all possible pairs of neurons, and took the average of these
2145 coefficients. We did this for all the trials with a visual stimulus. We observed a reduction in
2146 the COMb distribution's ν parameter at stimulus onset from around 1 to between 0 and 1 (see
2147 figure 4.7a). A value of ν less than 1 indicates positive association between the neurons (see
2148 section 4.3.5). We might expect to see this positive association reflected in the correlation
2149 coefficients, but this is not the case. We see no change in the time series of average correlation
2150 measures at stimulus onset.

2151 This may be due to the very short time bin we used in this case. We know that using small
2152 time bins can artificially reduce correlation measurements (Cohen and Kohn, 2011). In this
2153 case, fitting the COMb distribution may be a useful way to measure association in a neuronal
2154 ensemble over very short timescales (< 10ms).

2155 **4.4.4 Replicating stimulus related quenching of neural variability**

2156 Churchland et al. (2010) inspected the effect of a stimulus on neural variability. One of the
2157 measures of neural variability that they employed was the Fano factor of the spike counts of
2158 individual cells (see section 4.3.4). They found a reduction in neural variability as measured
2159 by the Fano factor in various cortical areas in a macaque at the onset of various visual stimuli,
2160 or a juice reward (Churchland et al., 2010).

2161 We measured the Fano factor of the spike count of each cell in each brain region, during
2162 each trial. We measured the mean and standard error of these Fano factors from 500ms
2163 before stimulus onset until 1000ms after stimulus end. For the primary visual cortex, we
2164 found a transient reduction in the Fano factor immediately after stimulus onset. We used
2165 a Mann-Whitney U test to check that the Fano factors measured in a window starting at

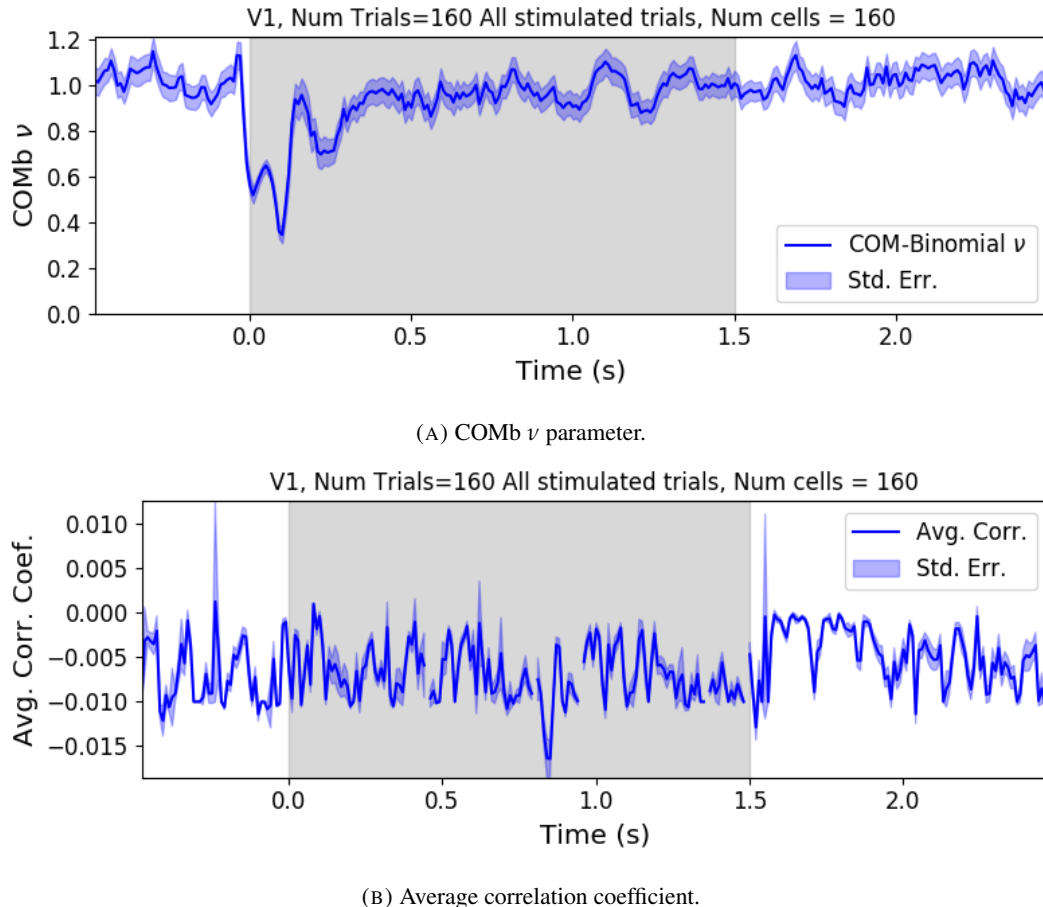


FIGURE 4.7: (A) We fit a Conway-Maxwell-binomial distribution to the number of active neurons in 1ms time bins of a 100ms sliding window. We did this for all trials with a visual stimulus and took the average across those trials. We see a transient drop in value for the distribution's ν parameter at stimulus onset. This shows an increase in association between the neurons. (B) We measured the correlation coefficient between the spike counts of all possible pairs of neurons in the same sliding window. We took the average of those coefficients. We also did this for every visually stimulated trial, and took the average across trials. The increase in association is not reflected with an increase in average correlation.

stimulus onset and ending 100ms later were significantly lower than the factors measured in a window ending at stimulus onset ($p < 0.001$, see figure 4.8a). We did not get this statistically significant result in any other region.

Our findings agree with those of Churchland et al. for the primary visual cortex. However Churchland also found a reduction in the Fano factor in the dorsal premotor cortex (PMd) at stimulus onset. Our measurements from the mouse motor cortex show no change at stimulus onset (see figure 4.8b). This could indicate some difference in the functionality of the motor cortex in a macaque and the motor cortex of a mouse.

Similar to these findings in the Fano factor, we found a reduction in the ν parameter of the COMB distribution on stimulus onset in V1 (figure 4.7a) and in no other region from

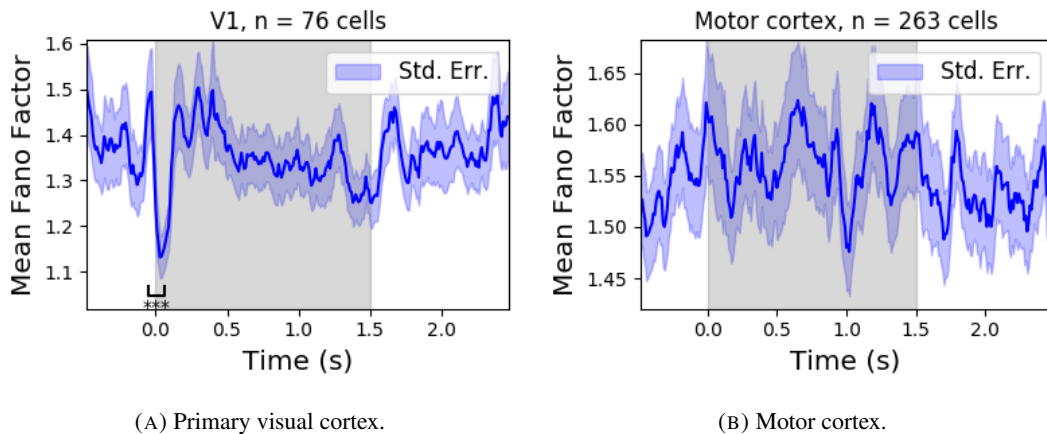


FIGURE 4.8: (A) The mean Fano factor of the spike counts of the cells in the primary visual cortex. Means were taken across cells first, then across trials. There was a significant decrease in the Fano factors immediately after stimulus onset. (B) The mean Fano factor of the spike counts of the cells in the motor cortex. No significant change in measurements at any point.

which we had data. Specifically, the ν parameter reduced from around 1, to between 1 and 0. This represents a change from no association between the neurons, to a positive association. It is possible that this positive association may be responsible for the reduction in the Fano factor.

4.5 Discussion

Our aim in this research was to develop a new statistical method for analysing the activity of a neuronal ensemble at very short timescales. We wanted our method to use information taken from the whole ensemble, but we also wanted the method to be quick and easy to implement. It is likely that analysis methods with these characteristics will become valuable as electrophysiological datasets include readings from more cells over longer time periods. In this case, we used the number of active, or spiking, neurons in a very short time bin ($< 10\text{ms}$) as a measure of ensemble activity.

First of all, we showed that there were changes in response that we could model at these very short time scales in some of the brain regions from which we had recordings. We observed changes in the average number of active neurons, and the variance of the number of active neurons in three different brain regions in response to visual stimuli. Since we know that correlated behaviour is associated with sensory perception (deCharms and Merzenich, 1996), we might hope to measure the pairwise correlations within the neuronal population in order to further investigate these responses. But, using such short time bins can produce

artificially small spike count correlation measurements (Cohen and Maunsell, 2009). Overcoming this limitation was one of our objectives for our new method. In order to do this, we abandoned the idea of measuring the correlations directly and embraced the concept of *association*. In order to quantify the association between neurons, we used the Conway-Maxwell-binomial distribution to model the number of active (spiking) neurons in an ensemble as a sum of possibly associated Bernoulli random variables.

We showed that the Conway-Maxwell-binomial distribution performed better than the more common options of the binomial and beta-binomial distributions. Furthermore, we showed that the positively associated behaviour between neurons in the primary visual cortex could be captured by fitting a Conway-Maxwell-binomial distribution, but was not captured by the more standard approach of measuring the spike count correlation. The associated behaviour could not be measured using spike count correlations, because of the very short bins required to capture short timescale behaviour.

We replicated a famous result from Churchland et al (2010) relating to the quenching of neural variability in cortical areas at stimulus onset, and in doing so, we established a correspondence between the association quantifying parameter of the Conway-Maxwell-binomial (COMb) distribution and the neural variability as measured by the Fano factor. We found a reduction in the ν parameter of the COMB distribution at stimulus onset, indicating a change from no association to positive association between neurons in V1. We found a corresponding reduction in the Fano factor of the individual cells in V1. The positive association between neurons induced by the stimulus would constrain the neurons to fire at the same time. The stimulus also induced a larger number of neurons to spike. These two actions combined could cause an increase in the firing rate of individual cells that is greater in magnitude than the increase in firing rate variability. If this is indeed the case, then the association as captured by the COMB distribution could be regarded as one of the ‘natural parameters’ of the ensemble response for short timescales. That is, a quantity that directly measures some aspect of the behaviour of the ensemble. In this case, it the correlated behaviour of the individual neurons is captured.

This work could be just a first step in creating analysis methods based on the Conway-Maxwell-binomial distribution, or similar statistical models. One way to extend the method would be to pair it up with the ‘Population Tracking model’ (O’Donnell et al., 2017). This model attempts to characterise the interaction between an ensemble and each member of the ensemble by quantifying the probability of spiking for a given a cell, given the number of active cells in the whole population. Combining this model with the COMB distribution

would give us a model that could accurately fit the number of active neurons at any moment, and that gives a probability of firing for each cell, and therefore probabilities for full spiking patterns, without adding a huge number of parameters to fit.

A more complex way to extend the model would be to fit a Conway-Maxwell-binomial distribution to data recorded from multiple brain regions simultaneously, with a different fit for each region, then to analyse the temporal relationship between the fitted parameters of each region. If we analysed the time series of the COMB distribution parameters from the different regions, looking at cross-correlations between regions, this may give some results relating to the timescales in which information is processed in different brain regions.

2238 **Chapter 5**

2239 **Studies with practical limitations &**
2240 **negative results**

2241 *Abstract*

2242 Here I will present some details on research topics that I started, but that unfortunately did not
2243 lead anywhere useful. There are two pieces of research, based on two papers. Each paper is
2244 related to the overall theme of my PhD of analysing and modelling behaviours of populations
2245 of neurons. The first part is based on a model of parallel spike trains including higher order
2246 interactions by Shimazaki et al (2012). The second part is based on a multiscale model for
2247 making inferences on hierarchical data.

2248 **5.1 Dynamic state space model of pairwise and higher order neu-**
2249 **ronal correlations**

2250 In their paper Shimazaki et al (2012) aimed to model spike trains from populations of neurons
2251 in parallel, with pairwise and higher order dynamic interactions between the trains. They
2252 modelled the spike trains as multi-variate binary processes using a log-linear model, and they
2253 extracted spike interaction parameters using a Bayesian filter/EM-algorithm. They developed
2254 a goodness-of-fit measure for the model to test if including these higher order correlations
2255 is necessary for an accurate model. Their measure was based on the Bayes factor but they
2256 also assessed the suitability of higher order models using the AIC and BIC. So the increase
2257 in the number of parameters associated with fitting higher order interactions was taken into
2258 account. They tested the performance of the model on synthetic data with known higher
2259 order correlations. They used the model to look for higher order correlations in data from
2260 awake behaving animals. They use the model to demonstrate dynamic appearance of higher
2261 order correlations in the monkey motor cortex (Shimazaki et al., 2012).

2262 We used the available Python repository to implement the model, and we successfully
2263 worked through the tutorial provided. But we found that the model did not scale well to
2264 larger populations. We attempted to fit the model to a population of 10 neurons and found we
2265 didn't manage to finish the process. Since, our goal was to find a model to scale to hundreds
2266 or thousands of neurons, we decided that this model was no longer worth pursuing.

2267 **5.2 A multiscale model for hierarchical data applied to**
2268 **neuronal data**

2269 In their paper Kolaczyk et al (2001) developed a framework for a modelling hierarchically
2270 aggregated data, and making inferences based on a model arising from this framework. They
2271 assumed that a hierarchical aggregation existed on the data in question, where each element at
2272 each level of the hierarchy had some associated measurements, an associated mean process,
2273 which was the expected value of these measurements. They also assumed that the measure-
2274 ments of each parent were equal to the sum of the measurements from all of its children.
2275 They showed that these assumptions gave rise to a relationship between parent and child
2276 measurements across all levels of the hierarchy, where the product of the likelihood of the
2277 parameters of the lowest level of the hierarchy can be expressed as products of conditional
2278 likelihoods of the elements of higher levels of the hierarchy (Kolaczyk and Huang, 2010).

2279 They gave examples of these expressions for measurements sampled from Gaussian dis-
2280 tributions, and Poisson distributions, and showed the definitions of the hierarchical param-
2281 eters which reparametrise the distribution of these data taking the hierarchy into account.
2282 They go on to suggest prior distributions for this multiscale model, and integrate these priors
2283 to give posterior distributions for the measurements from each element at each level in the hi-
2284 erarchy, and expressions for the MAP estimated parameters of each the associated processes
2285 (Kolaczyk and Huang, 2010).

2286 We implemented their model in Python by creating some synthetic data from Poisson
2287 distributions, and defining a hierarchy by agglomerating these data. We calculated the MAP
2288 estimates using our knowledge of the hierarchy, and using the expressions given in the paper.
2289 We found that the MAP estimates were far less accurate than would be achieved by simply
2290 ignoring the hierarchy during estimation, and using a maximum likelihood approach. After
2291 that, we decided to move on.

2292 **Chapter 6**

2293 **Discussion**

2294 In this project, we attempted to address some of the challenges in data collection from
2295 large neuronal ensembles (specifically with calcium imaging) and some of the problems in
2296 analysing the data collected from large neuronal ensembles.

2297 Firstly, we investigated the relationship between cell biochemistry, action potentials and
2298 the fluorescence traces produced by fluorescent calcium indicators. We did this by building
2299 a biophysical model that takes in a spike train and returns the fluorescence trace that that
2300 spike would induce. The model included mechanics for the binding of calcium to fluorescent
2301 and endogenous mobile and immobile buffers, and the consequent changes in concentration
2302 of free and bounded calcium. The model consisted of 17 parameters, 13 of which were
2303 set according to data from the literature, and 4 of which were free parameters. We trained
2304 the model using simultaneously collected spiking and calcium imaging data (Berens et al.,
2305 2018). We fitted the model by matching the $\Delta F/F_0$ in response to an action potential, and
2306 by matching the power spectrum of the actual fluorescence trace. This meant that our model
2307 would include the correct amount of noise as well as return the correct change in amplitude
2308 in response to an action potential.

2309 Since our model produced fluorescence traces, we could apply spike inference algorithms
2310 to the modelled fluorescence traces that our model produced after training, and compare the
2311 performance of the algorithms on the modelled traces to their performance on the real traces.
2312 We used three spike inference algorithms, two of which were based on modelling the cal-
2313 cium trace as an autoregression (Friedrich and Paninski, 2016; Pnevmatikakis et al., 2016),
2314 and another inference algorithm that was a little more biologically inspired, but amounted to
2315 a very similar algorithm (Deneux et al., 2016). We compared the performance of the algo-
2316 rithms by using them to infer spikes from 20 real and modelled fluorescence traces induced
2317 by 20 corresponding real spike trains. We then used several binary classification measures
2318 (true positive rate, accuracy etc.) to asses the quality of the spike inference for the real and

2319 modelled fluorescence traces. We found that the spike inference algorithms performed sim-
2320 ilarly on real and modelled traces, showing that our model is capturing at least some of the
2321 characteristics of the real fluorescence traces.

2322 In order to investigate the effect of indicator characteristics on the modelled fluorescence
2323 trace and spike inference quality, we perturbed the indicator's affinity and dissociation rate
2324 in parallel, keeping the ratio of the two the same for all perturbations. We measured the SNR
2325 of the trace, and the true positive rate of the spike inference algorithms at each perturbed
2326 value pair. We found that perturbing the values lower caused in decrease in SNR and spike
2327 inference quality. This shows that our model could be used to test theoretical fluorescent cal-
2328 cium indicators without having to actually manufacture them. Experimental neuroscientists
2329 could also use our model to judge which indicator characteristics are most influential in their
2330 experimental context.

2331 We then investigated the effect of perturbing buffer concentration, and indicator concen-
2332 tration, on the signal-to-noise ratio of the modelled fluorescence trace and spike inference
2333 quality. This was a worthwhile experiment because endogenous buffer concentrations vary
2334 from cell to cell (Bartol et al., 2015; Maravall et al., 2000; Neher and Augustine, 1992), as
2335 does indicator expression (Chen et al., 2013). We found that extreme perturbations away
2336 from the indicator concentration taken from the literature lowered the SNR of the trace, and
2337 the spike inference quality. We also found that increases in the concentration of endogenous
2338 buffer above the value taken from the literature caused a decrease in the SNR and spike infer-
2339 ence quality. This reiterates that the indicator and endogenous buffers compete to bind with
2340 free calcium molecules, and this has an effect on fluorescence and consequently on spike
2341 inference.

2342 We then created some synthetic spike trains with controlled mean firing rates sampled
2343 the rates from an Ornstein-Uhlenbeck process. We found that the higher the firing rate, the
2344 lower the accuracy of the spike inference algorithms. But the mean firing could perhaps be
2345 inferred from the amplitude of the fluorescence traces. The higher firing rate, the higher the
2346 amplitude. Calibrating the model to facilitate and accurate measurement would require some
2347 kind of ground truth, but relative comparisons could be made without any other knowledge
2348 of the underlying spiking process.

2349 One obvious limitation to our model is the lack of binding mechanics for both the indi-
2350 cator and endogenous buffers. Greenberg et al included these mechanics in their successful
2351 spike inference model. We felt that the timescale of these binding mechanics was so small in
2352 comparison to the fluorescence dynamics that omitting them would make no difference. But

2353 it is possible that their inclusion would improve our model.

2354 After investigating the difficulties with inferring spiking data from calcium imaging data,
2355 we moved from data collection to analysis and we decided to implement a new network anal-
2356 ysis method on data from a neuronal ensemble. Using an electrophysiological dataset with
2357 spike sorted data from 9 different brain regions in 3 mice (Steinmetz, Carandini, and Harris,
2358 2019), we binned the spike times for each cell into spike counts for each cell and measured
2359 the correlation coefficients between these spike counts for a selection of cells evenly dis-
2360 tributed across the 9 regions. We repeated these measurements for time bin widths ranging
2361 from 5ms to 3s. We rectified these measurements and, for a given time bin width, used them
2362 as weights for a weighted undirected graph where each node represents a neuron, and the
2363 weight of each edge is the correlation between the neurons represented by the nodes on that
2364 edge. We applied a novel spectral analysis and community detection method (Humphries
2365 et al., 2019) to this network. This clustered the nodes in our ensemble into communities
2366 whose behaviour was more correlated than expected. Our measure of 'expected correlation
2367 strength' were based on a random network that matched our data network's sparsity and total
2368 weight. We compared the detected communities to the anatomical division of our cells using
2369 clustering comparison measures. We then conditioned the binned spike counts on the be-
2370 haviour of the mouse using the principal components of a video of the mouses face recorded
2371 simultaneously with the electrophysiology. We broke the total covariance down into 'spike
2372 count covariance' and 'signal covariance' components conditioning on the behavioural data
2373 and using the law of total covariance. We then repeated our analysis for spike count corre-
2374 lations, and signal correlation. Finally, since our community detection method was only valid
2375 on graphs with non-negative weights, we used different methods for creating a non-negative
2376 graph from our total correlations, and we repeated our analysis on those graphs.

2377 Our first finding was that the time bin width used to bin spike times into spike counts had
2378 a effect on the mean magnitude of the correlations measured. The wider the bin, the higher
2379 the correlations. Not only that, we separated the pairs into positively and negative correlated
2380 pairs, and we found that positively correlated pairs have greater correlation coefficients when
2381 using a wider bin, and negatively correlated pairs have more negative correlation coefficients
2382 when using a wider bin. We also found that the width of the bin used had an effect on the
2383 distribution of the spike counts. For smaller bin widths, the distribution of spike counts was
2384 better represented by a skewed distribution like the Poisson distribution. For wider bins, the
2385 spike counts were better represented by a Gaussian distribution.

2386 Next we investigated the differences between correlations within regions and between

2387 regions. When we divided the pairs according to those two groups, we found that the mean
2388 within-region correlations were higher at every bin width, and the difference between the two
2389 means grew with increasing bin width. When we split the pairs of cells according to their
2390 regions, we found that the mean within-region correlations in any given region were usually
2391 greater than the mean between-region correlations for any region pair involving that region.
2392 The difference between the mean within-region correlation and the highest between-region
2393 correlations involving that region grew smaller with increasing bin width. To investigate this
2394 further, we plotted these mean correlations in matrices. Although the mean within-region
2395 correlations were usually the highest value in their row or column, as the bin width increased,
2396 the mean between-region correlations grew in magnitude relative to the within-region figure.

2397 Next we chose a null network model, and we used the ‘Network Noise Rejection’ pro-
2398 cess (Humphries et al., 2019) to check for additional structure in our correlation based data
2399 network that was not captured by the null model. We found additional structure for any bin
2400 width that we used. We also found that the dimensionality of the additional structure reduced
2401 as we increased the bin width. This could mean that the processes or representations that take
2402 place over longer timescales within the brain also take place in a lower dimensional space.

2403 We applied a community detection method (Humphries, 2011) to the signal correlation
2404 networks arising from the network noise rejection. We found that the number of communi-
2405 ties detected decreased with increasing bin width. We also noticed that at shorter bin widths,
2406 the detected communities were more likely to consist of cells from one brain region only.
2407 We investigated this further by using clustering comparison methods to compare the detected
2408 communities with the anatomical division of the cells. We found that for short timescales
2409 < 50ms correlated communities tended to exist within anatomical regions, and for longer
2410 timescales > 100ms, the correlated communities tended to exist across anatomical regions.
2411 This is broadly in agreement with a similar finding for EEG data from humans performing se-
2412 mantic or memory tasks (Stein and Sarnthein, 2000). Von Stein et al. (2000) found that visual
2413 processing taking place locally in the visual system was captured in the gamma frequency
2414 range (25 – 70Hz), while semantic processing was captured in the beta range (12 – 18Hz),
2415 and tasks involving mental imagery and working memory retention were captured in the theta
2416 and alpha ranges (4 – 8Hz, and 8 – 12Hz respectively).

2417 We then conditioned our correlation measures on the the mouse’s behaviour. This al-
2418 lowed us to create spike count correlation (or noise correlation) networks, and signal corre-
2419 lation networks (Cohen and Kohn, 2011). We applied our analysis to these networks. For the

spike count correlation networks we found very similar results to the total correlation networks. More communities at smaller bin widths, and communities resembled the anatomical division at smaller bin widths. Given that recent findings show that behaviour can account for correlated spiking in many areas of the brain (Stringer et al., 2019), these results for the spike count correlation show that this correlated behaviour is still processed locally at short timescales, while processes and representations that take more time make use of correlated activity across multiple regions.

For the signal correlations, we still found additional structure in these networks. But we always detected a smaller number of communities. These communities also had no relation to the anatomical division of the cells. This result shows that there are groups of cells across multiple brain regions that are activated similarly by certain behaviours.

All of the networks so far were based on rectified correlation measures, because the network noise rejection and community detection processing is (currently) only valid for networks with non-negative weights. For the final part of our analysis, we tried different ways of transforming our total correlations into non-negative quantities before applying our analysis. First of all we took the absolute value of our correlation measures. Our results were very similar to those for the rectified correlations with the exception that we detected more communities consistently. It is possible that using this method detects both positively and negatively correlated communities.

We also tried reversing the sign of all the correlations, then rectifying the network. We hope that this would allow us to detect the negatively correlated communities. We did detect communities in these networks, but never more than three, and these communities bore no relationship with the anatomical distribution of the cells.

There is a lot of potential for network science applications in computational neuroscience. For example, some pairwise measure other than correlation coefficients could be used as the weights of the graph. A directed measure like synaptic connectivity could be used as the basis for directed graphs. The analysis methods applicable to directed graphs could give insights about the formation of synaptic connections, or the dynamic changes in these connections over time. Other methods of community detection could be used on directed or undirected graphs. We used a ‘hard’ clustering method in our research, that is, each neuron could be a member of one cluster/community only. ‘Fuzzy-clustering’ methods do exist, where each element of the set to be clustered could be a member of more than one cluster (Baadel, Thabtah, and Lu, 2016).

Having spent much time investigating correlated behaviour using coefficients of spike

counts, we decided to try another method for capturing correlated behaviour in neuronal ensembles. We used electrophysiological data taken from 5 brain regions of an awake mouse exposed to visual stimuli (Steinmetz et al., 2019). We modelled the number of active neurons in a given brain region as the number of successes in a collection of dependent Bernoulli random variables using the Conway-Maxwell-binomial distribution. To avoid violating the Bernoulli assumption, we binned the spike times using 1ms bins. The Conway-Maxwell-binomial distribution is a two parameter extension of the standard binomial distribution. The extra parameter allows the distribution to capture possible positive or negative association between the Bernoulli trials (Kadane, 2016). This means that we are assuming that all the neurons are dependent in the same way. This is not an accurate assumption, but it allows us model the data in a simple way.

First of all we established that there were changes in the number of active neurons in response to the visual stimuli. This was the case in the hippocampus, thalamus, and primary visual cortex. Each region had its own signature response. We measured the mean and variance of the number of active neurons in a sliding window starting before stimulus onset, and finishing after the end of stimulus presentation.

As well as the Conway-Maxwell-binomial distribution, we also fitted binomial, and beta-binomial distributions to the number of active neurons in a sliding window. We found that the Conway-Maxwell-binomial distribution was the best fit for over 90% of the samples. This means that the COMb distribution is capturing some dependency between the neurons, because the binomial distribution assumes independence. Also the COMb distribution captures this dependence more accurately than the beta-binomial distribution, which does have some capacity for over dispersion.

Next we showed that the Conway-Maxwell-binomial distribution captured the change in association at stimulus onset better than the correlation coefficient. The extremely small bin width artificially shrunk the correlation coefficient to the point where this measurement didn't detect any correlated activity. But the association parameter of the COMb distribution detected some positive association between the neurons at stimulus onset. So, for particularly short time bins, where neurons can be treated as Bernoulli random variables, the Conway-Maxwell-binomial distribution is a good way to capture correlated behaviour. There are other measurements for capturing association to which this distribution should be compared. Cross-correlograms could be used for some measure of synchrony, for example.

Finally, we replicated a famous finding of Churchland et al. (2010) relating to the quenching of neural variability at stimulus onset, thereby finding a parallel between this reduction

2488 in the Fano factor and a reduction in the association parameter of the COMb distribution.

2489 We showed that computational neuroscientists can make progress by being inventive with
2490 their statistical models. A similar distribution to investigate would be the Conway-Maxwell-
2491 Poisson distribution. This is similar to the standard Poisson distribution, but with an addi-
2492 tional parameter that allows for over- or under- dispersion relative to a Poisson distribution.
2493 This might be ideal for modelling firing rates of individual neurons. Some interaction be-
2494 tween the fitted parameters could capture the association between neurons.

2495 There is one technology that has the potential to take over from both electrophysiology
2496 and calcium imaging. The technique of voltage imaging has become more useful in recent
2497 years. The aim for neuroscience would be to develop a voltage imaging dye or protein that
2498 images the membrane potential of a neuron with enough spatial and temporal resolution to
2499 detect action potentials. Genetically encoded voltage indicators have been developed, and
2500 enable targeting of specific neuronal ensembles. But their spatial resolution is not yet high
2501 enough to single out individual cells (Bando et al., 2019). These indicators have the potential
2502 to take over from calcium imaging, and if imaging deep within the brain becomes possible,
2503 electrophysiology could also be replaced. This is speculation, but the potential is there.

2504

Bibliography

- 2505 Allen, William E. et al. (2019). “Thirst regulates motivated behavior through modulation of
 2506 brainwide neural population dynamics”. In: *Science* 364.6437.
- 2507 Baadel, S., F. Thabtah, and J. Lu (2016). “Overlapping clustering: A review”. In: *2016 SAI
 2508 Computing Conference (SAI)*, pp. 233–237.
- 2509 Baldassano, Christopher et al. (2017). “Discovering Event Structure in Continuous Narrative
 2510 Perception and Memory”. In: *Neuron* 95.3, 709 –721.e5.
- 2511 Bando, Yuki et al. (2019). “Genetic voltage indicators”. In: *BMC Biology* 17.1, p. 71.
- 2512 Bartol, Thomas M. et al. (2015). “Computational reconstitution of spine calcium transients
 2513 from individual proteins”. In: *Frontiers in Synaptic Neuroscience* 7, p. 17.
- 2514 Berens, Philipp et al. (May 2018). “Community-based benchmarking improves spike rate in-
 2515 ference from two-photon calcium imaging data”. In: *PLOS Computational Biology* 14.5,
 2516 pp. 1–13.
- 2517 Bezanson, Jeff et al. (Sept. 2012). “Julia: A Fast Dynamic Language for Technical Comput-
 2518 ing”. In: *MIT*.
- 2519 Buccino, Alessio P. et al. (2019). “SpikeInterface, a unified framework for spike sorting”. In:
 2520 *bioRxiv*.
- 2521 Chen, Tsai-Wen et al. (July 2013). “Ultrasensitive fluorescent proteins for imaging neuronal
 2522 activity”. In: *Nature* 499, 295–300.
- 2523 Churchland, Mark M. et al. (2010). “Stimulus onset quenches neural variability: a widespread
 2524 cortical phenomenon”. eng. In: *Nature neuroscience* 13.3. 20173745[pmid], pp. 369–378.
- 2525 Cohen, Marlene R. and Adam Kohn (2011). “Measuring and interpreting neuronal corre-
 2526 lations”. In: *Nature Neuroscience* 14.7, pp. 811–819.
- 2527 Cohen, Marlene R. and John H. R. Maunsell (2009). “Attention improves performance pri-
 2528 marily by reducing interneuronal correlations”. eng. In: *Nature neuroscience* 12.12. 19915566[pmid],
 2529 pp. 1594–1600.
- 2530 Dana, Hod et al. (Sept. 2014). “Thy1-GCaMP6 Transgenic Mice for Neuronal Population
 2531 Imaging In Vivo”. In: *PloS one* 9, e108697.

- 2532 deCharms, R. Christopher and Michael M. Merzenich (1996). “Primary cortical represen-
2533 tation of sounds by the coordination of action-potential timing”. In: *Nature* 381.6583,
2534 pp. 610–613.
- 2535 Deneux, Thomas et al. (July 2016). “Accurate spike estimation from noisy calcium signals
2536 for ultrafast three-dimensional imaging of large neuronal populations in vivo”. In: *Nature
2537 Communications* 7.1.
- 2538 Dombeck, Daniel A. et al. (2010). “Functional imaging of hippocampal place cells at cellular
2539 resolution during virtual navigation”. In: *Nature Neuroscience* 13.11, pp. 1433–1440.
- 2540 Éltes, Tímea et al. (2019). “Improved spike inference accuracy by estimating the peak am-
2541 plitude of unitary [Ca₂₊] transients in weakly GCaMP6f-expressing hippocampal pyra-
2542 midal cells”. In: *The Journal of Physiology* 597.11, pp. 2925–2947.
- 2543 Faas, Guido C. et al. (2011). “Calmodulin as a direct detector of Ca₂₊ signals”. In: *Nature
2544 Neuroscience* 14.3, pp. 301–304.
- 2545 Fiala, John C. and Kristen M. Harris (1999). *Dendrite Structure*.
- 2546 Flach, Boris (Sept. 2013). “A Class of Random Fields on Complete Graphs with Tractable
2547 Partition Function”. In: *IEEE transactions on pattern analysis and machine intelligence*
2548 35, pp. 2304–6.
- 2549 Forney, G. D. (1973). “The viterbi algorithm”. In: *Proceedings of the IEEE* 61.3, pp. 268–
2550 278.
- 2551 Fosdick, Bailey et al. (Aug. 2016). “Configuring Random Graph Models with Fixed Degree
2552 Sequences”. In: *SIAM Review* 60.
- 2553 Friedrich, Johannes and Liam Paninski (2016). “Fast Active Set Methods for Online Spike In-
2554 ference from Calcium Imaging”. In: *Advances in Neural Information Processing Systems*
2555 29. Ed. by D. D. Lee et al. Curran Associates, Inc., pp. 1984–1992.
- 2556 Ganmor, Elad, Ronen Segev, and Elad Schneidman (2011). “Sparse low-order interaction
2557 network underlies a highly correlated and learnable neural population code”. In: *Pro-
2558 ceedings of the National Academy of Sciences* 108.23, pp. 9679–9684.
- 2559 Girard, P., J. M. Hupé, and J. Bullier (2001). “Feedforward and Feedback Connections Be-
2560 tween Areas V1 and V2 of the Monkey Have Similar Rapid Conduction Velocities”. In:
2561 *Journal of Neurophysiology* 85.3. PMID: 11248002, pp. 1328–1331.
- 2562 Greenberg, David et al. (Nov. 2018). “Accurate action potential inference from a calcium
2563 sensor protein through biophysical modeling:” in:
- 2564 Gründemann, Jan et al. (2019). “Amygdala ensembles encode behavioral states”. In: *Science*
2565 364.6437.

- 2566 Hodgkin, A. L. and A. F. Huxley (1939). “Action Potentials Recorded from Inside a Nerve
2567 Fibre”. In: *Nature* 144.3651, pp. 710–711.
- 2568 Humphries, Mark et al. (Jan. 2019). “Spectral rejection for testing hypotheses of structure in
2569 networks”. In:
- 2570 Humphries, Mark D. (2011). “Spike-Train Communities: Finding Groups of Similar Spike
2571 Trains”. In: *Journal of Neuroscience* 31.6, pp. 2321–2336.
- 2572 Jun, James J. et al. (2017). “Fully integrated silicon probes for high-density recording of
2573 neural activity”. In: *Nature* 551.7679, pp. 232–236.
- 2574 Kadane, Joseph B. (June 2016). “Sums of Possibly Associated Bernoulli Variables: The
2575 Conway–Maxwell-Binomial Distribution”. In: *Bayesian Anal.* 11.2, pp. 403–420.
- 2576 Kilhoffer, Marie-Claude et al. (Sept. 1992). “Use of Engineered Proteins With Internal Tryp-
2577 topahan Reporter Groups and Perturbation Techniques to Probe the Mechanism of Ligand-
2578 Protein Interactions: Investigation of the Mechanism of Calcium Binding to Calmodulin”.
2579 In: *Biochemistry* 31.34, pp. 8098–8106.
- 2580 Koch, Christoff (1999). *Biophysics of Computation: Information Processing in Single Neu-*
2581 *rons*. Oxford University Press.
- 2582 Kolaczyk, Eric and Haiying Huang (Sept. 2010). “Multiscale Statistical Models for Hierar-
2583 chical Spatial Aggregation”. In: *Geographical Analysis* 33, pp. 95 –118.
- 2584 Lee, Suk-HO et al. (July 2000). “Differences in Ca²⁺ buffering properties between excitatory
2585 and inhibitory hippocampal neurons from the rat”. In: *The Journal of Physiology* 525.
- 2586 Litwin-Kumar, Ashok, Maurice Chacron, and Brent Doiron (Sept. 2012). “The Spatial Struc-
2587 ture of Stimuli Shapes the Timescale of Correlations in Population Spiking Activity”. In:
2588 *PLoS computational biology* 8, e1002667.
- 2589 Maravall, M et al. (May 2000). “Estimating intracellular calcium concentrations and buffer-
2590 ing without wavelength ratioing”. In: *Biophysical Journal* 78.5, pp. 2655–2667.
- 2591 Maugis, Pa (Jan. 2014). “Event Conditional Correlation: Or How Non-Linear Linear Depen-
2592 dence Can Be”. In:
- 2593 Meilă, Marina (2007). “Comparing clusterings—an information based distance”. In: *Journal*
2594 *of Multivariate Analysis* 98.5, pp. 873 –895.
- 2595 Murray, John D. et al. (2014). “A hierarchy of intrinsic timescales across primate cortex”. In:
2596 *Nature Neuroscience* 17.12, pp. 1661–1663.
- 2597 Neher, E. and G. J. Augustine (1992). “Calcium gradients and buffers in bovine chromaffin
2598 cells”. eng. In: *The Journal of physiology* 450. 1331424[pmid], pp. 273–301.

- 2599 O'Donnell, Cian et al. (Jan. 2017). "The population tracking model: a simple, scalable statistical model for neural population data". English. In: *Neural Computation* 29.1, pp. 50–
2600 93.
- 2602 Okun, Michael et al. (2015). "Diverse coupling of neurons to populations in sensory cortex".
2603 In: *Nature* 521.7553, pp. 511–515.
- 2604 Ouzounov, Dimitre G. et al. (2017). "In vivo three-photon imaging of activity of GCaMP6-
2605 labeled neurons deep in intact mouse brain". eng. In: *Nature methods* 14.4. 28218900[pmid],
2606 pp. 388–390.
- 2607 Patterson, Carolyn A. et al. (2014). "Similar adaptation effects in primary visual cortex and
2608 area MT of the macaque monkey under matched stimulus conditions". In: *Journal of
2609 Neurophysiology* 111.6. PMID: 24371295, pp. 1203–1213.
- 2610 Peron, Simon P. et al. (2015). "A Cellular Resolution Map of Barrel Cortex Activity during
2611 Tactile Behavior". In: *Neuron* 86.3, pp. 783–799.
- 2612 Pnevmatikakis, E.A. et al. (Jan. 2016). "Simultaneous Denoising, Deconvolution, and Demix-
2613 ing of Calcium Imaging Data". In: *Neuron* 89.2, pp. 285–299.
- 2614 Pnevmatikakis, Eftychios et al. (Nov. 2013). "Bayesian spike inference from calcium imaging
2615 data". In: *Conference Record - Asilomar Conference on Signals, Systems and Computers*.
- 2616 Pnevmatikakis, Eftychios et al. (Sept. 2014). "A structured matrix factorization framework
2617 for large scale calcium imaging data analysis". In:
- 2618 Schneidman, Elad et al. (2006). "Weak pairwise correlations imply strongly correlated net-
2619 work states in a neural population". eng. In: *Nature* 440.7087. 16625187[pmid], pp. 1007–
2620 1012.
- 2621 Shannon, C. E. (1948). "A Mathematical Theory of Communication". In: *Bell System Tech-
2622 nical Journal* 27.3, pp. 379–423.
- 2623 Shimazaki, Hideaki et al. (2012). "State-space analysis of time-varying higher-order spike
2624 correlation for multiple neural spike train data". eng. In: *PLoS computational biology*
2625 8.3. 22412358[pmid], e1002385–e1002385.
- 2626 Staude, Benjamin, Sonja Grün, and Stefan Rotter (2010). "Higher-Order Correlations and
2627 Cumulants". In: *Analysis of Parallel Spike Trains*. Ed. by Sonja Grün and Stefan Rotter.
2628 Boston, MA: Springer US, pp. 253–280.
- 2629 Stein, Astrid von and Johannes Sarnthein (2000). "Different frequencies for different scales
2630 of cortical integration: from local gamma to long range alpha/theta synchronization". In:
2631 *International Journal of Psychophysiology* 38.3, pp. 301 –313.

- 2632 Steinmetz, Nick, Matteo Carandini, and Kenneth D. Harris (2019). "Single Phase3" and
2633 "Dual Phase3" *Neuropixels Datasets*.
- 2634 Steinmetz, Nick et al. (Mar. 2019). "Eight-probe Neuropixels recordings during spontaneous
2635 behaviors". In:
- 2636 Stevenson, Ian H. and Konrad P. Kording (2011). "How advances in neural recording affect
2637 data analysis". In: *Nature Neuroscience* 14.2, pp. 139–142.
- 2638 Stringer, Carsen et al. (2019). "Spontaneous behaviors drive multidimensional, brainwide
2639 activity". In: *Science* 364.6437.
- 2640 Tada, Mayumi et al. (2014). "A highly sensitive fluorescent indicator dye for calcium imaging
2641 of neural activity in vitro and in vivo". In: *European Journal of Neuroscience* 39.11,
2642 pp. 1720–1728.
- 2643 Tian, Lin et al. (2009). "Imaging neural activity in worms, flies and mice with improved
2644 GCaMP calcium indicators". eng. In: *Nature methods* 6.12. 19898485[pmid], pp. 875–
2645 881.
- 2646 Tkačik, Gašper et al. (2014). "Searching for collective behavior in a large network of sen-
2647 sory neurons". eng. In: *PLoS computational biology* 10.1. 24391485[pmid], e1003408–
2648 e1003408.
- 2649 Treves, Alessandro and Stefano Panzeri (1995). "The Upward Bias in Measures of Informa-
2650 tion Derived from Limited Data Samples". In: *Neural Computation* 7.2, pp. 399–407.
- 2651 Vinh, Nguyen Xuan, Julien Epps, and James Bailey (Dec. 2010). "Information Theoretic
2652 Measures for Clusterings Comparison: Variants, Properties, Normalization and Correc-
2653 tion for Chance". In: *J. Mach. Learn. Res.* 11, 2837–2854.
- 2654 Vogelstein, Joshua T. et al. (Oct. 2010). "Fast nonnegative deconvolution for spike train infer-
2655 ence from population calcium imaging". In: *Journal of neurophysiology* 104.6, 295–300.
- 2656 Wierzynski, Casimir M. et al. (2009). ""State-Dependent Spike-Timing Relationships be-
2657 tween Hippocampal and Prefrontal Circuits during Sleep"". In: "Neuron" "61" ."4", "587
2658 –596".
- 2659 Zariwala, Hatim A. et al. (2012). "A Cre-dependent GCaMP3 reporter mouse for neuronal
2660 imaging in vivo". eng. In: *The Journal of neuroscience : the official journal of the Society
2661 for Neuroscience* 32.9. 22378886[pmid], pp. 3131–3141.
- 2662 Zou, Hui and Trevor Hastie (2005). "Regularization and variable selection via the Elastic
2663 Net". In: *Journal of the Royal Statistical Society, Series B* 67, pp. 301–320.